

NASA/CR-2005-213929



Investigation of the Thermomechanical Response of Shape Memory Alloy Hybrid Composite Beams

Brian A. Davis
North Carolina State University, Raleigh, North Carolina

October 2005

The NASA STI Program Office . . . in Profile

Since its founding, NASA has been dedicated to the advancement of aeronautics and space science. The NASA Scientific and Technical Information (STI) Program Office plays a key part in helping NASA maintain this important role.

The NASA STI Program Office is operated by Langley Research Center, the lead center for NASA's scientific and technical information. The NASA STI Program Office provides access to the NASA STI Database, the largest collection of aeronautical and space science STI in the world. The Program Office is also NASA's institutional mechanism for disseminating the results of its research and development activities. These results are published by NASA in the NASA STI Report Series, which includes the following report types:

- **TECHNICAL PUBLICATION.** Reports of completed research or a major significant phase of research that present the results of NASA programs and include extensive data or theoretical analysis. Includes compilations of significant scientific and technical data and information deemed to be of continuing reference value. NASA counterpart of peer-reviewed formal professional papers, but having less stringent limitations on manuscript length and extent of graphic presentations.
- **TECHNICAL MEMORANDUM.** Scientific and technical findings that are preliminary or of specialized interest, e.g., quick release reports, working papers, and bibliographies that contain minimal annotation. Does not contain extensive analysis.
- **CONTRACTOR REPORT.** Scientific and technical findings by NASA-sponsored contractors and grantees.

- **CONFERENCE PUBLICATION.** Collected papers from scientific and technical conferences, symposia, seminars, or other meetings sponsored or co-sponsored by NASA.
- **SPECIAL PUBLICATION.** Scientific, technical, or historical information from NASA programs, projects, and missions, often concerned with subjects having substantial public interest.
- **TECHNICAL TRANSLATION.** English-language translations of foreign scientific and technical material pertinent to NASA's mission.

Specialized services that complement the STI Program Office's diverse offerings include creating custom thesauri, building customized databases, organizing and publishing research results ... even providing videos.

For more information about the NASA STI Program Office, see the following:

- Access the NASA STI Program Home Page at <http://www.sti.nasa.gov>
- E-mail your question via the Internet to help@sti.nasa.gov
- Fax your question to the NASA STI Help Desk at (301) 621-0134
- Phone the NASA STI Help Desk at (301) 621-0390
- Write to:
NASA STI Help Desk
NASA Center for AeroSpace Information
7121 Standard Drive
Hanover, MD 21076-1320

NASA/CR-2005-213929



Investigation of the Thermomechanical Response of Shape Memory Alloy Hybrid Composite Beams

Brian A. Davis
North Carolina State University, Raleigh, North Carolina

National Aeronautics and
Space Administration

Langley Research Center
Hampton, Virginia 23681-2199

Prepared for Langley Research Center
under Cooperative Agreement NCC-1-02043

October 2005

Acknowledgments

I would like to especially thank North Carolina State University (NCSU) Mechanical and Aerospace Engineering Department, National Institute of Aerospace, and the Structural Acoustics Branch at NASA LaRC for funding my education. I am extremely grateful for the opportunity to be a part of the NIA educational program and to learn and conduct research in an environment like NASA LaRC. The amount that I have learned from all coursework at NCSU, and from being involved in research at NASA LaRC has been priceless. I would like to give special thanks to my committee members; Dr. Travis Turner, Dr. Stefan Seelecke, Dr. Richard Keltie, and Dr. Robert Nagel for their support and contributions to this work. I have benefited greatly from all courses and discussions I have had with you all, and feel privileged to be able to learn from you. I would especially like to thank my research mentor and advisor at NASA LaRC, Dr. Travis Turner, for the opportunity to work on a great research project, for all the valuable time spent teaching me, and for making this learning experience so enjoyable. The opportunity to work with and learn from you has allowed me to gain so much valuable experience, and I greatly appreciate all your guidance. I would also like to especially thank my advisor at NCSU for helpful insights and suggestions to this work and for all the support and encouragement through my NIA education and research. I would like to also thank my previous advisor, Dr. Richard F. Keltie, for all the guidance and help throughout my first year of my master's program.

I gratefully acknowledge the assistance of Gary Fleming (NASA LaRC) for calibration, and processing of the PMI data. Thanks are also due to Howard Jones and George Hilton (NASA LaRC) for their contribution to the static and dynamic test configurations. The assistance of Larry Becker and Brian Howerton (Lockheed-Martin) for the development of the LabVIEW-based thermal controller/data acquisition system is also greatly appreciated.

Available from:

NASA Center for AeroSpace Information (CASI)
7121 Standard Drive
Hanover, MD 21076-1320
(301) 621-0390

National Technical Information Service (NTIS)
5285 Port Royal Road
Springfield, VA 22161-2171
(703) 605-6000

Preface

This research results presented herein constitute a master's thesis prepared by Brian Davis under the direction of Dr. Travis L. Turner of NASA Langley Research Center, Structural Acoustics Branch and Dr. Stefan Seelecke of North Carolina State University, Department of Mechanical and Aerospace Engineering.

TABLE OF CONTENTS

LIST OF TABLES	VI
LIST OF FIGURES	VII
LIST OF SYMBOLS	XI
INTRODUCTION	1
1.1 SHAPE MEMORY ALLOYS	1
1.2 MOTIVATION/APPLICATIONS	3
1.3 OBJECTIVES	4
EXPERIMENTAL MEASUREMENT OF THE STATIC THERMOELASTIC RESPONSE OF THE SMAHC BEAM	7
2.1 BACKGROUND	7
2.2 EXPERIMENTAL SET-UP	8
2.3 PROJECTION MOIRE' INTERFEROMETRY	9
2.4 STATIC THERMOELASTIC RESPONSE EXPERIMENTAL RESULTS	10
Laser Displacement Transducer Results	10
Projection Moire' Interferometry Results	13
EXPERIMENTAL MEASUREMENTS OF THE DYNAMIC RESPONSE OF THE SMAHC BEAM	16
3.1 BACKGROUND	16
3.2 EXPERIMENTAL SET-UP	16
3.3 DYNAMIC RESPONSE DATA POST-PROCESSING OVERVIEW	17
3.4 SMAHC BEAM DYNAMIC RESPONSE EXPERIMENTAL RESULTS	19
THERMOELASTIC CONSTITUTIVE MODELING FORMULATION	21
4.1 BACKGROUND	21
4.2 THERMOELASTIC CONSTITUTIVE MODEL/STIFFNESS PROPERTY FORMULATION	21
4.3 STRESS-STRAIN RELATION FOR ORTHOTROPIC MATERIAL	25
NUMERICAL MODELING OF SMAHC BEAM SPECIMENS IN THE COMMERCIAL FINITE ELEMENT CODE ABAQUS	28
5.1 BACKGROUND	28
5.2 STATIC RESPONSE MODELING RESULTS IN ABAQUS	29
5.3 DYNAMIC RESPONSE MODELING RESULTS IN ABAQUS	31
CONCLUSIONS	34
REFERENCES	36
TABLES	38
FIGURES	45
APPENDICES	82

APPENDIX A	83
APPENDIX B	93
APPENDIX C	96
APPENDIX D	98

LIST OF TABLES

Table 3.1- Beam 2 Run 1 dynamic response RMS displacement values as a function of temperature for positions 1, 2, and 3 along the length of the beam.....	38
Table 3.2- Beam 3 Run 2 dynamic response RMS displacement values as a function of temperature for positions 1, 2, and 3 along the length of the beam.....	39
Table 3.3- Beam 2 dynamic response modal parameter estimates for runs 1, 2, and 3.....	40
Table 3.4- Beam 3 dynamic response modal parameter estimates for runs 1, 2, and 3.....	41
Table 4.1- Thermomechanical material property measurement of the Fiberite E-glass/934 epoxy material system in principal material direction.....	42
Table 4.2- Thermomechanical material property measurements of the Nitinol Ribbon actuator material.....	43
Table 4.3- Nitinol Ribbon Transformation Temperatures measured by DSC.....	44

LIST OF FIGURES

Figure 1.1- SMA Lattice Structure at different phases.....	45
Figure 1.2– SMA body under tensile loading/unloading at low temperature, exhibiting the shape memory effect upon heating⁴.....	45
Figure 1.3– Schematic of martensitic and reverse transformations⁵.....	46
Figure 1.4– Stress-Strain Curves for Shape Memory Alloys at various intermediate temperatures⁶.....	46
Figure 1.5- Load-Deformation diagrams for shape memory alloy at various temperatures (fully martensitic-quasiplastic) and (fully austenitic-pseudoelastic)⁴.....	47
Figure 1.6– Nitinol recovery stress vs. temperature and initial strain⁷.....	47
Figure 1.7– Recovery stress vs. temperature, thermal cycle for nitinol ribbon samples at 4% pre-strain ⁸.....	48
Figure 1.8– Variation of austenite start temperature with weight content (%) of Nickel in Nitinol Alloy¹⁰.....	48
Figure 2.1- 22”x1”x0.080” Glass Epoxy/SMA Hybrid Beam (45/0-45/90)_{2s} Lamination with SMA embedded in the 0° lamina only⁸.....	49
Figure 2.2- Consolidated SMAHC structure after curing cycle, and machined SMAHC beam specimens used for experiments⁸.....	49
Figure 2.3– Static Experimental Set-up: SMAHC Beam3 installed in the beam fixture (front view).....	49
Figure 2.4a– Mechanical and electrical grip of beam fixture (front view).....	50
Figure 2.4b- Mechanical and electrical grip of beam fixture (back view).....	50
Figure 2.5- Static Thermoelastic Response Experimental Component Schematic.....	51
Figure 2.6– Static Thermoelastic Response Experimental Configuration Overview.....	51
Figure 2.7- Simple PMI System Schematic³⁵.....	52
Figure 2.8– SMAHC Beam2 Laser Displacement Experimental Results of Midspan for Runs 1-9.	52
Figure 2.9– SMAHC Beam3 Laser Displacement Experimental Results for Midspan Runs 1-10.	53
Figure 2.10– Experimental Configuration of initial imperfection measurements.....	53
Figure 2.11- Laser Translation versus PMI initial imperfection measurements of SMAHC beams installed in beam fixture.	54
Figure 2.12- Laser Translation Measurements of SMAHC Beam3 for three different boundary condition configurations of the Garolite G-10 insulation blocks.	54

Figure 2.13- Garolite G-10 Insulation Blocks Configurations for Laser Displacement Transducer Experiments (Top view of beam fixture boundaries)	55
Figure 2.14- Projection Moire' Interferometry calibration plate³⁴	55
Figure 2.15- PMI differential image data and line fit for the centerline out of plane deflection for Beam3 Run3 at T=160°F	56
Figure 2.16- PMI full field imaging of the SMAHC Beam2 Run1	56
Figure 2.17- PMI full field imaging of the SMAHC Beam 2 Run 4	57
Figure 2.18- PMI full field imaging of the SMAHC Beam 2 Run 8	57
Figure 2.19- PMI full field imaging of the SMAHC Beam 3 Run 1	58
Figure 2.20- PMI full field imaging of the SMAHC Beam 3 Run 4	58
Figure 2.21- PMI full field imaging of the SMAHC Beam 3 Run 8	59
Figure 2.22- Beam2 PMI vs. Laser Static Deflection Measurements	59
Figure 2.23- Beam3 PMI vs. Laser Static Deflection Measurements	60
Figure 3.1- SMAHC beam dynamic response experimental configuration	60
Figure 3.2- SMAHC beam specimen installed, with mounted beam response transducers and fixture transducers (back view)	61
Figure 3.3- Acceleration PSD for the base excitation of the beam with a RMS value of .25g (96.5 in/s²)	61
Figure 3.4- SMAHC beam dynamic response experimental component schematic	62
Figure 3.5- Acceleration vs. Displacement PSD generated by attached m-file, which post-processes the acceleration time history data	63
Figure 3.6- SMAHC Beam 2 PSD's for selected temperatures at position 1	63
Figure 3.7- SMAHC Beam 2 PSD's for selected temperatures at position 2 (midspan)	64
Figure 3.8- SMAHC Beam 2 PSD's for selected temperatures at position 3	64
Figure 3.9- SMAHC Beam 3 PSD's for selected temperatures at position 1	65
Figure 3.10- SMAHC Beam 3 PSD's at selected temperatures for position 2 (midspan)	65
Figure 3.11- SMAHC Beam 3 PSD's at selected temperatures for position 3	66
Figure 3.12- Modal frequency variation of modes 1, and 3 as a function of temperature	66
Figure 4.1- Representative volume element of SMAHC lamina¹⁸	67
Figure 4.2- Applied stress vs. strain for .09x.006x10 inch sample with 0% pre-strain at ambient temperature and 120°C (248 °F)¹⁸	67
Figure 4.3- Applied stress vs. strain for .09x.006x10 inch sample with 4% pre-strain at ambient temperature and 120°C (248 °F)¹⁸	68
Figure 4.4- Recovery Stress vs. Temperature of the Nitinol ribbon (pre-strained 4% and released) for thermal cycles 2, 4, and 50¹⁸	68

Figure 4.5– Modulus for Nitinol ribbon prestrained 4% and released as a function of temperature ¹⁸	69
Figure 4.6- Differential Scanning Calorimetry (DSC) Results for the Nitinol ribbon sample showing transformation temperatures.	69
Figure 5.1- ABAQUS Finite Element Mesh of the SMAHC beam with clamped boundary conditions.	70
Figure 5.2- Static Response SMAHC Beam 2 Run 6 ABAQUS vs experimental results for original recovery force measurements, and 15 °F shift in recovery force input data.	70
Figure 5.3– Static Response SMAHC Beam 2 Run 7 ABAQUS vs. experimental results for original recovery force measurements, and 10 °F shift in recovery force input data.	71
Figure 5.4- Static Response SMAHC Beam 2 Run 8 ABAQUS vs. experimental results for original recovery force measurements, and 15 °F shift in recovery force input data.	71
Figure 5.5- Static Response SMAHC Beam 3 Run 3 ABAQUS vs. experimental results for original recovery force measurements, and 15 °F shift in recovery force input data.	72
Figure 5.6- Static Response SMAHC Beam 3 Run 6 ABAQUS vs. experimental results for original recovery force measurements, and 15 °F shift in recovery force input data.	72
Figure 5.7- Static Response SMAHC Beam 3 Run 8 ABAQUS vs. experimental results for original recovery force measurements, and 20 °F shift in recovery force input data.	73
Figure 5.8- Beam 2 Run 8, position 2 (midspan) PSD comparison at ambient ($\Delta f = .25$ Hz).	73
Figure 5.9- Beam 2 run 8, position 2 (Midspan) PSD comparison at 71.1 °C (160 °F) ($\Delta f = .25$ Hz).	74
Figure 5.10- Beam 2 Run 8, position 2 (midspan) PSD comparison at 93.3 °C (200 °F) ($\Delta f = .25$ Hz).	74
Figure 5.11- Beam 2 Run 8, position 2 (midspan) PSD comparison at 121.1 °C (250 °F).	75
Figure 5.12- Beam 3 Run 8, position 2 (midspan) PSD comparison at 21.7 °C (71 °F) ($\Delta f = .25$ Hz).	75
Figure 5.13- Beam 3 Run 8, position 2 (midspan) PSD comparison at 71.1 °C (160 °F) ($\Delta f = .25$ Hz).	76
Figure 5.14- Beam 3 Run 8, position 2 (midspan) PSD comparison at 93.3 °C (200 °F) ($\Delta f = .25$ Hz).	76
Figure 5.15- Beam 3 Run 8, position 2 (midspan) PSD comparison at 121.1 °C (250 °F) ($\Delta f = .25$ Hz).	77
Figure 5.16- Beam 2 Run 8, position 1 PSD comparison for selected temperatures ($\Delta f = .25$ Hz).	77
Figure 5.17- Beam 3 Run 3, position 3 PSD's comparison for selected temperatures ($\Delta f = .25$ Hz).	78

Figure 5.18- Beam 3 Run 1, position 3 PSD's comparison through the buckling range (T=71 °F).....	78
Figure 5.19- Beam 3 Run 1, position 3 PSD's comparison through the buckling range (T=100 °F).....	79
Figure 5.20- Beam 3 Run 1, position 3 PSD's comparison through the buckling range (T=130 °F).....	79
Figure 5.21- Beam 3 Run 1, position 3 PSD's comparison through the buckling range (T=140 °F).....	80
Figure 5.22- Beam 3 Run 1, position 3 PSD's comparison through the buckling range (T=150 °F).....	80
Figure 5.23- Beam 3 Run 1, position 3 PSD's comparison through the buckling range (T=160 °F).....	81
Figure 10.1- PMI full field imaging of the SMAHC Beam 2 Run 1.....	84
Figure 10.2- PMI full field imaging of the SMAHC Beam 2 Run 2.....	84
Figure 10.3- PMI full field imaging of the SMAHC Beam 2 Run 3.....	85
Figure 10.4- PMI full field imaging of the SMAHC Beam 2 Run 4.....	85
Figure 10.5- PMI full field imaging of the SMAHC Beam 2 Run 5.....	86
Figure 10.6- PMI full field imaging of the SMAHC Beam 2 Run 6.....	86
Figure 10.7- PMI full field imaging of the SMAHC Beam 2 Run 7.....	87
Figure 10.8- PMI full field imaging of the SMAHC Beam 2 Run 8.....	87
Figure 10.9- PMI full field imaging of the SMAHC Beam 2 Run 9.....	88
Figure 10.10- PMI full field imaging of the SMAHC Beam 3 Run 1.....	88
Figure 10.11- PMI full field imaging of the SMAHC Beam 3 Run 2.....	89
Figure 10.12- PMI full field imaging of the SMAHC Beam 3 Run 3.....	89
Figure 10.13- PMI full field imaging of the SMAHC Beam 3 Run 4.....	90
Figure 10.14- PMI full field imaging of the SMAHC Beam 3 Run 5.....	90
Figure 10.15- PMI full field imaging of the SMAHC Beam 3 Run 6.....	91
Figure 10.16- PMI full field imaging of the SMAHC Beam 3 Run 7.....	91
Figure 10.17- PMI full field imaging of the SMAHC Beam 3 Run 8.....	92

LIST OF SYMBOLS

Roman Symbols

A	Cross-Sectional area
A_f	Austenite Finish Temperature
A_s	Austenite Start Temperature
Au	Gold
Cd	Cadmium
d	Distance between grid lines
D	Compliance matrix values
E	Elastic Modulus
G	Shear Modulus
f_n	Natural frequency (cycles/sec)
f_k	Frequency values
i	Row index for a pixel
j	Column index for a pixel
k	Index number
M^+	Martensitic plus variant
M^-	Martensitic minus variant
M_f	Martensite Finish Temperature
M_s	Martensite Start Temperature
N	Total number of samples
Ni	Nickel
n	Index number of samples
P_{cr}	Critical Load
Q	Reduced stiffness matrix values
t	Time
T	Temperature
T_o	Initial temperature
[T]	Transformation matrix
Ti	Titanium

W	Width of SMAHC Lamina
X_k	Fourier components
x_n	Time history sample value
$z(x,y)$	Out of plane deformation at a point specified by coordinates

Greek Symbols

α	Coefficient of thermal expansion
Δ	Shearing deformation
Δ_w	Deformation in principle material direction 2.
ε	Strain
γ	Engineering shear strain
ν_{12}	Poisson's ratio
π	3.14159265
θ	Orientation angle
σ	Stress
σ_r	Recovery Stress
τ	Shear stress
υ	Volume fraction
ω_n	Natural angular frequency
ζ	Damping Ratio ($\frac{c}{2m\omega_n}$)

Subscripts

a	Actuator material
f	Finish transformation temperature
m	Composite matrix material

r	Recovery
s	Start transformation temperature

Superscripts

+	Positive orientation
-	Negative orientation
-1	Inverse
T	Transpose

Abbreviations

CCD	Charge Coupled Device
DSC	Differential Scanning Calorimetry
ECTEM	Effective Coefficient of Thermal Expansion Model
FFT	Fast Fourier Transform
FRF	Frequency Response Function
GPIB	General Purpose Interface Bus
LaRC	Langley Research Center
LMA	Lockheed Martin Astronautics
NASA	National Aeronautics and Space Administration
PID	Proportional, Integral, and Differential feedback
PMI	Projection Moire' Interferometry
PSD	Power Spectral Density
RMS	Root Mean Square
SDOF	Single Degree of Freedom
SIM	Stress Induced Martensite

SMAHC Shape Memory Alloy Hybrid Composites

SME Shape Memory Effect

VI Virtual Instrument

Units of Measurement

ft Foot

in Inch

m Meter

K Degrees Kelvin

V Volts

W Watts

s Second

MPa MegaPascal (10^6 N/m²)

slug English unit of mass (=32.2 *lbm pounds mass*)

μm Micrometer

/ft Per foot

° Degrees

°C Degree Celsius

°F Degree Farenheight

Hz Hertz

lbf Force pounds

kg Kilograms

N Newton

Miscellaneous Symbols

$\langle \rangle$ Normalized quantity (ratio of rms and mean value)

∂ Partial derivative

$d[]$ Derivative

d/dt Time derivative of a quantity

$\int[]$ Integral

Σ Summation of a quantity

SUMMARY

Previous work at NASA Langley Research Center (LaRC) involved fabrication and testing of composite beams with embedded, pre-strained shape memory alloy (SMA) ribbons within the beam structures. That study also provided comparison of experimental results with numerical predictions from a research code making use of a new thermoelastic model for shape memory alloy hybrid composite (SMAHC) structures. The previous work showed qualitative validation of the numerical model. However, deficiencies in the experimental-numerical correlation were noted and hypotheses for the discrepancies were given for further investigation. The goal of this work is to refine the experimental measurement and numerical modeling approaches in order to better understand the discrepancies, improve the correlation between prediction and measurement, and provide rigorous quantitative validation of the numerical analysis/design tool. The experimental investigation is refined by a more thorough test procedure and incorporation of higher fidelity measurements such as infrared thermography and projection moiré interferometry. The numerical results are produced by a recently commercialized version of the constitutive model as implemented in ABAQUS and are refined by incorporation of additional measured parameters such as geometric imperfection. Thermal buckling, post-buckling, and random responses to thermal and inertial (base acceleration) loads are studied. The results demonstrate the effectiveness of SMAHC structures in controlling static and dynamic responses by adaptive stiffening. Excellent agreement is achieved between the predicted and measured results of the static and dynamic thermomechanical response, thereby providing quantitative validation of the numerical tool.

Chapter 1

INTRODUCTION

1.1 Shape Memory Alloys

Shape Memory Alloys (SMA) have become increasingly researched over the past 30 years, due to their fascinating functional properties. In the 1950's the Shape Memory Effect (SME), the recovery of deformation to an original shape by heating to a critical temperature, was discovered in Gold (Au 47.5%) and Cadmium (Cd 52.5%) Alloy by Chang and Read¹. Then in 1963 the SME was discovered at the Naval Ordnance Laboratory in equiatomic composition Titanium-Nickel Alloy (Ni 52%-57%) by Beuhler and Wiley (Nitinol)². Since then other alloys have been discovered to possess the same attractive functionality. Although, the particular alloy, named Nitinol (Nickel, Titanium, Naval, Ordnance, Laboratory), is considered to be the SMA with the most potential for engineering applications because of its ductility at low temperature, high degree of shape-recovery capability (8% strain), large pseudoelastic hysteresis, corrosion and fatigue resistance, biomedical compatibility, and relatively high electrical resistance³.

SMA's are defined as a class of materials that have the ability to recover a given deformation when heated above a certain temperature. There are two stable phases of the lattice structure for these metal alloys that may exist, termed martensite and austenite. Austenite phase represents the high temperature stable state, and possesses the symmetric, cubic crystal lattice structure (See Figure 1.1) with a high elastic modulus. Martensite represents the low temperature stable state, and possesses the less symmetric lattice structure of a monoclinic crystal with a lower elastic modulus. Additionally, the martensite phase may exist as twinned or de-twinned (M^+ , M^-) states (See Figure 1.1). The interactions of thermal and applied mechanical loads to this material system are the basis for driving the phase transitions. The phase transitions between these two states are what provide the unique and attractive functionalities of SMA. When cooled under no applied mechanical load the material transforms from the austenite phase to the self-accommodating martensitic twinned phase. There is no observable shape change associated with this transformation. The boundaries between the layers of twinned martensite are easily deformed under applied load; therefore deformation can easily be achieved in the martensitic state. Figure 1.2 shows the transformation behavior under heating/cooling and loading/unloading of an SMA element. Once a tensile load is applied in the martensitic state, the self-accommodated martensite-twinned configuration will transform, at a critical load, to M^+ or M^- variants depending on the direction of the applied load. When the uniaxial load is removed the M^+ or M^- phase will remain, leaving the given deformation to the SMA element. Upon heating of the martensitic phase the "reverse transformation" occurs in which the lattice structure returns to austenite and recovers any deformation. As previously stated this is termed the shape memory effect. The SME always refers to the free recovery of the deformation. It is important to mention that during the attempt to transform to austenite while constrained, high recovery forces may be generated. This makes SMA's very attractive as actuators in mechanical systems.

Associated with the martensitic and reverse transformations are four characteristic temperatures. Martensite start (M_s) is the temperature at which the SMA begins transforming

from austenite to martensite; martensite finish (M_f) is the temperature at which the SMA becomes fully martensitic and the transformation is complete; austenite start (A_s) represents the temperature at which the “reverse transformation” begins; and austenite finish (A_f) represents the temperature at which the SMA is fully in austenitic phase. The difference in the phase transformation temperatures results in an associated hysteresis curve, which can be seen in Figure 1.3.

SMA's can also exhibit transformation pseudoelastic behavior, which is associated with the recovery of the strain upon unloading. If the material is above A_f temperature and is loaded to a critical stress then the martensitic transformation can be induced, which is termed stress induced martensite (SIM). SIM produces a large deformation in the material, which is fully recovered upon unloading when the material is above A_f temperature (Superelasticity). Pseudoelastic behavior of SMA is attractive for use as an energy dissipation mechanism, and can provide hysteretic damping to structures. The pseudoelastic behavior of SMA is commonly exploited in medical and dental applications.

SIM can also occur when the material is at lower temperatures than A_f temperature, but only partial strain recovery occurs upon unloading at temperatures between $A_s < T < A_f$. In Figure 1.4 the stress-strain diagrams for various temperatures demonstrate the different effects of SMA phase transitions. When the material is at a temperature below M_f and is in the twinned martensitic phase its yield stress to induce fully M^+ de-twinned state, and thus a large deformation, is quite low. Once the material is fully de-twinned and deformed to M^+ , continued loading would produce elastic deformation until slip occurs. Once the material is at a higher temperature in the austenitic phase, the yield stress value is much higher than the martensitic phase's. Figure 1.5 shows the corresponding load-deformation curves for the material at various temperatures representing the quasi-plastic behavior (low temperature) and the pseudoelastic behavior (high temperature).

As previously mentioned SMA's are capable of producing large forces when recovering strain. The SME or reverse transformations described above refer to a free recovery (under zero load). If the strain recovery occurred under load the SMA performs work and is termed a restrained recovery. If the SMA is prevented from recovering strain once heated above the transformation temperature that is termed constrained recovery. Recovery stresses up to 700 MPa may be generated during constrained recovery. In this work the constrained recovery of SMA is used to induce large tensile forces in pre-strained SMA actuator ribbons. It is known that the recovery force generated during constrained recovery is a function of pre-strain, temperature, and thermal cycle. Cross reported the recovery stress vs. temperature for various pre-strain amounts, as seen in Figure 1.6 for Nitinol .1 in diameter rod⁷. At the A_s temperature the recovery stress increases with temperature and then levels off near A_f temperature. As pre-strain increases the recovery stress increases, but will never exceed the austenitic yield stress. Material characterization of Nitinol has been performed experimentally at NASA LaRC and Lockheed Martin Astronautics (LMA) to quantify the recovery stress vs. temperature, among the other temperature dependent properties, of the Nitinol alloy in ribbon form used for this study⁸. Figure 1.7 shows the recovery stress vs. temperature and thermal cycles at 4% pre-strain. It can be seen that the recovery stress/actuation degrades with thermal cycle to near 50 cycles and then levels off.

Factors such as Ni content, aging, thermo-mechanical treatment and addition of alloying elements, which affect the structure, are important for controlling the memory behavior⁹. The transformation temperatures for SMA (M_s , M_f , A_s , A_f) can be altered by

changing the composition of the alloy. It was reported by Beuhler and Wang that the A_s temperature for Nitinol can be varied from $-50\text{ }^\circ\text{C}$ ($-122\text{ }^\circ\text{F}$) to $166\text{ }^\circ\text{C}$ ($330\text{ }^\circ\text{F}$) by changing the Ni content from 54.4% to 56.5% by weight as shown in Figure 1.8¹⁰. When a nearly equiatomic Nitinol (Ni-Ti) alloy is fully annealed the SME consists of transformation directly from the austenite phase to the martensite phase. However, when the equiatomic Nitinol is partially annealed, the austenitic phase transforms to a R-phase, which consist of a rhombohedral lattice structure, before transforming to the martensitic monoclinic structure. This R-phase structure is an intermediate martensitic transformation, which is reported to strengthen the austenitic lattice structure and improve the recoverability of the SME^{11,12}. This additional transformation, being a thermoelastic, martensitic transformation itself, also possesses a SME and pseudoelasticity but produces a much smaller strain recovery, and hysteresis. This is an attractive property for sensor applications. Due to the improved shape memory effect and strengthening of the material, partial annealing is desirable for most applications. The presence of the R-phase does not affect the performance of the alloy for most applications, but will show up in material characterization measurements.

Because there are so many aspects that may affect the transformation behavior of SMA's it is important to have accurate material characterization measurements for experiment and modeling agreement. The transformation temperatures are typically measured by differential scanning calorimetry (DSC). This measurement technique results in plots of heat flow vs. temperature, and shows endothermic peaks corresponding to the austenitic phase transformations, and exothermic peaks corresponding to the martensitic twinned transformation and R-phase transformation. Thus, from the DSC measurements one can observe the values of the transformation temperatures, and the state of the SMA. Then mechanical properties of the SMA are measured by thermomechanical testing to quantify properties such as recovery stress, elastic modulus, and coefficients of thermal expansion vs. temperature to accurately model experimental behavior of SMA.

1.2 Motivation/Applications

The unique functionality of SMA's described above make them a very attractive material for a variety of applications. Since their discovery, early applications involved coupling devices, fasteners, and electrical connectors¹³. The most well documented large-scale application of SMA's in 1971 was as a coupling to connect titanium tubing in the Grumman F-14 aircraft⁹. More recent applications for SMA's have been focused in the medical field, and smart material research. "Smart Structures" have been defined by C.A. Rogers as material systems with intelligence and life features integrated in the microstructure of the material system to reduce mass and energy and produce adaptive functionality¹⁴. Materials commonly classified as "smart materials" include piezoelectric materials, magnetostrictive materials, electrorheological fluids, magnetorheological fluids, and shape memory alloys. All of these materials possess the ability to change their inherent properties as a result of a sensing mechanism. SMA's have the ability to change stiffness, shape, natural frequency, damping and other mechanical characteristics in response to a change in temperature. The recent interest in smart structures has shown that SMA's have great potential for vibration, structural acoustic, and structural shape control¹⁵. Smart materials such as SMA's can be used, as actuator/sensing devices in structures to accomplish desired adaptive properties. One such type of structure was discovered when Rogers and Robertshaw¹⁶

introduced the idea of embedding SMA actuators in a composite laminate. These structures became known as Shape Memory Alloy Hybrid Composites (SMAHC).

The effects of noise and vibration are present in almost every aspect of every day life. It has become common practice to find ways to reduce noise radiation and vibration of structures. Common noise and vibration reduction techniques involve increasing the mass, stiffness, or damping of a structure. This is typically done by passive treatments such as constrained layer damping, acoustic absorption foam, tuned vibration absorbers, visco-elastic vibration isolators, etc.¹⁷. The concept of employing smart structures that can adapt to the surrounding environment, to provide such previously mentioned functionality would be extremely attractive in any field of applications where weight-penalty is of concern. Once such application is in the field of high-performance aerospace vehicles where the excitation levels of their structures are high due to engine noise and turbulent boundary layer fluctuating pressures. Typical treatments for these effects are often limited to relatively low temperatures and high frequencies, and cannot adapt to a changing environment. The elevated thermal environment that aerospace vehicles are exposed to could activate SMAHC structures adaptive properties, rather than employ auxiliary hydraulic/electronic systems to facilitate actuation. Therefore smart structures such as SMAHC's are of great interest.

There has been much research done in recent years on SMAHC's. At NASA LaRC a great deal of experimental work has been performed on SMAHC structures with embedded Nitinol ribbon in which a new thermo-elastic model to predict the thermal buckling and post-buckling response of the structures was formulated¹⁸. Similar theoretical and experimental work has been done by Baz, who used Nitinol SMA wires for controlling the natural frequencies of composite beams¹⁹. The same has also been done for SMAHC plates²⁰. A multitude of studies have been performed on the thermal buckling and post-buckling behavior of composite beams and plates reinforced by SMA components^{21,22,23,24}. Other work done in the area has included active vibration control of cantilevered beams with the actuators external to the structure²⁵. There have also been analytical formulations developed to demonstrate the vibration/structural acoustic control of SMAHC panels^{26,27}.

There has been much work done to develop theoretical models that capture the thermo-mechanical behavior of SMA, as well as characterization of SMA material properties^{28,29,30,31}. There have also been many good comprehensive overviews of SMA characteristics and their applications published^{6,9}. Although, as explained in the subsequent section, constitutive models that lend themselves easily to actual engineering property measurements are scarce.

1.3 Objectives

There has been previous investigation of SMAHC beam structures at NASA LaRC, which provided comparison of experimental results with a research code making use of a new thermomechanical model for SMAHC structures. The previous work showed qualitative validation of the model via the research code, but more definitive investigations are necessary. The goal of this work is to conduct experimental investigations on SMAHC beams to more accurately quantify the static buckling/post-buckling and dynamic response characteristics of the specimens. Numerical results will be generated in the commercial finite element code ABAQUS for comparison to experimental results, in contrast to the research code previously used. Fabrication of SMAHC beam specimens was previously performed at NASA LaRC, in which pre-strained (4%) SMA (Nitinol) ribbons were embedded within layers of glass-epoxy matrix material. The glass-epoxy matrix material was chosen in order to allow electrical

isolation of the SMA actuators, and flaw detection due to the material's translucency. Once the SMA actuator ribbons are placed in the desired layers, the laminate is cured, and the SMA and glass-epoxy are integrated into one hybrid composite structure. Activation of the SMA actuators by resistive heating will serve as an adaptive stiffening mechanism to the structure by generating large recovery forces in the embedded pre-strained SMA ribbons. Accurate measurement techniques will be used to capture the adaptive stiffening effect of the SMA actuators. Numerical modeling will be performed in order to show the correlation between the measured and predicted responses.

Results from measurements of the static response of the SMAHC beam specimens, under thermal load by resistive heating, will be presented. This requires the application of an electrical current through the embedded SMA ribbon. The A_s temperature (40 °C (104 °F)) for the embedded SMA actuators is above ambient temperature thus once the temperature initially increases the SMAHC beam will be subjected to in plane compressive forces due to thermal expansion thus inducing buckling and post-buckling phenomena. The in plane compressive forces responsible for the post-buckled deflection will be overcome by the adaptive stiffening of the actuators once the temperature is high enough for activation of the SME. This highly nonlinear response behavior is quantified by a laser displacement transducer, Projection Moire' Interferometry (PMI), and infrared thermal imaging measurements. These measurement techniques also accurately determine initial geometric imperfections of the SMAHC beam specimens to help obtain accurate numerical models of the experimental response.

Additionally, the steady-state dynamic response of the SMAHC beams, under random inertial loads is measured. Once the dynamic response time histories are captured for the beam specimens this data is post-processed into FFT, FRF, PSD, and coherence functions, which are used for damping estimates, and displacement RMS values of the SMAHC's vibration response. The results demonstrate the adaptive stiffening characteristics of the SMA actuators, and provide accurate data to be used in the numerical simulation of the experiments.

A new thermo-elastic model was recently developed, that makes use of engineering property measurement, by Turner³². This effective coefficient of thermal expansion model (ECTEM) is relatively simplified, and easily integrated into commercial structural analysis codes such as ABAQUS. The other aforementioned constitutive models are based on the micro-mechanical behavior of the SMA and typically calculate the stress in SMA material based on three components; an elastic component, transformational component, and a thermal component, that are all dependent on a martensitic volume fraction. The calculations of the volume fractions differ from model to model but are usually functions of stress and temperature. In the ECTEM the stress in an SMA material is based purely on an elastic component, and an effective thermal strain component. This effective thermal strain term represents both the thermal and transformational components of other models. As a consequence, the ECTEM model is limited to thermally activated transformations, but is particularly attractive for SMAHC because it only requires the experimental measurement of fundamental engineering properties. Therefore it can easily be used in commercial structural analysis codes that have classical nonlinear thermo-elasticity capabilities. In the case of SMAHC structures, the micro-mechanical models are not efficient at modeling many spatially distributed SMA actuators. The ECTEM allows this to be done easily, by implementing the composite properties from measurements of the material properties of each individual material making up the composite. The formulation of the ECTEM model will be explained in detail in Chapter 5 in order to show how a model making use of thermo-elastic properties can be

implemented easily into a finite element formulation for efficient structural analysis. Also, the reader is referred to the more detailed formulation, Turner³².

Chapter 2

EXPERIMENTAL MEASUREMENT OF THE STATIC THERMOELASTIC RESPONSE OF THE SMAHC BEAM

In this chapter a background is given on the fabrication of the SMAHC beam specimens, the buckling/postbuckling behavior, and geometric imperfections. Then the experimental set-up and instrumentation functionality are described. Then a brief overview of the Projection Moire' Interferometry (PMI) measurement technique is given. Finally, the experimental results of the laser displacement measurement and PMI measurements are presented and compared.

2.1 Background

The project consists of static/dynamic response experiments on two SMAHC beam specimens, which were previously fabricated. The fabrication procedure will briefly be described. For a more detailed explanation of the fabrication process the reader is referred to previous work at NASA LaRC³². The beam specimens were fabricated from glass-epoxy prepreg and Nitinol ribbon materials with a ply orientation sequence of $(45/0/-45/90)_{2s}$. The glass epoxy prepreg has a thickness of 1.27×10^{-4} m (.005 inches) and the Nitinol ribbon had cross section dimensions of $.0023 \times 1.5 \times 10^{-4}$ m (.09x.006 inches). Therefore, 5 pre-strained (4%) SMA ribbons were placed side by side in the middle of the 0° glass-epoxy layer to represent the 0.45-inch actuator width called for by design. The schematic of the SMAHC beam specimen can be seen in Figure 2.1 with dimensions of $0.5588 \times 0.0254 \times 0.0019$ m (22x1x0.078 in). The SMA actuator ribbons had a length of 0.6604 m (26 in), therefore there is an excess of SMA actuator material extending from the boundaries of the beam used as electrical leads for resistive heating.

The SMAHC fabrication procedure consisted of pre-straining the SMA actuator ribbons (4%), stacking of each glass-epoxy ply in the corresponding orientation while placing the actuators in the 0.45 inch width strips cut from the middle of 0° plies, curing the laminate while restraining the actuators, and machining of the two beam specimens from the consolidated SMAHC laminate structure. The curing cycle consists of placing the laminate lay-up in vacuum drawn to an internal pressure of .0475 atm, and then subjected to an autoclave cure cycle in which a max temperature of 176.7°C (350°F) is reached. Upon curing of the lay-up, the laminate constituents are integrated into one hybrid composite structure. The whole hybrid composite structure panel and the beam specimens after machining can be seen in Figure 2.2.

Typically when a beam is subjected to compressive loads in the axial direction, the beam loses stability. The Euler Load is the critical load at which the beam loses stability. Theoretically a lateral load is applied to cause deflection to a new position from which the beam will not return when the lateral load is removed. In reality this deflection occurs not as a result of an applied lateral load, but to geometric imperfections in the beam. The SMAHC beams were installed into a beam fixture with clamped boundary conditions. The first experiments will involve applying only a thermal load to the SMAHC beam by electrically activating the embedded SMA actuators. The heating of the constituent materials with

clamped boundary conditions will generate a compressive load within the SMAHC beam. Once this compressive load reaches the critical value (Euler buckling load) the beam buckles undergoing a large deflection. In classical theory the stiffness of the beam goes to zero and deflection goes to infinity at the critical load (P_{cr}). Mathematically the solution path of the beam “bifurcates” to a new equilibrium position.

As previously mentioned the laminate consists of geometric imperfections, which dictate the direction of the buckling phenomena. As temperature of the post-buckled beam continues to increase, the embedded SMA actuators will be activated and generate in-plane tensile recovery forces that will overcome the compressive forces and render the post-buckled state of the beam back to its flat position. Therefore it is important to study these static responses of the SMAHC beams because the buckling/post-buckling states are part of the dynamic response as well. During the static response experiments accurate measurement techniques using Projection Moire’ Interferometry, laser displacement transducer, and infrared thermal imaging will be conducted to accurately capture the static response characteristics.

2.2 Experimental Set-up

In these static response experiments a thermal cycle, which consisted of increasing the temperature of the SMA actuators from 23°C (74 °F) to 121 °C (250 °F), was conducted 10 times for 2 separate beam specimens for repeatability investigation. The SMAHC beam was installed into the beam fixture as shown in Figure 2.3 with clamped boundary conditions. Each SMAHC beam has an unsupported length of .4572m (18 in). The aluminum beam fixture consists of a mechanical grip, which applies fixed boundary conditions on each end, and electrical grips that apply the electrical current to the SMA actuators embedded within the beam. Figure 2.4a shows the mechanical and electrical grips from the front of the beam fixture. The positive power supply lead can be seen connected to the electrical grip block. This entire block is electrically activated but is isolated from the mechanical gripping block by a layer of Garolite G-10 insulation. The SMAHC beam is also thermally isolated from the beam fixture by layers of Garolite G-10 installed between the mechanical grip surfaces. The Garolite G-10 is a glass fabric-epoxy insulator, which is a relatively hard/stiff material that should eliminate any compression under in-plane loads caused by the SMA recovery stress during testing. In similar tests a fibrous ceramic insulator was in service, which showed signs of compression during testing, thus relieving some of the recovery stress in the activated SMA actuators. Type-T thermocouples were attached to the beam specimen on the center of the beam 1 inch from the left mechanical grip, to both of the mechanical grips, and one is measuring the surrounding ambient air temperature. These thermocouples can be seen attached to the left mechanical grip and the beam specimen in Figure 2.2b, which shows the backside of the beam fixture. Thermocouple measurements are subject to large error due to contact resistance, and “fin” effect, in which the attached thermocouple lead conducts heat away from the contact and the heat is lost into the surrounding air due to convection. Therefore, the thermocouple measurements are used for monitoring purposes only. An infrared thermal imaging camera (FLIR Thermacam SC2000) was used for control measurements of the beam specimen temperature. The thermal camera eliminates the measurement uncertainty of contact resistance and “fin” effect, but does require calibration to the target emissivity. The average total hemispherical emissivity of the beam specimens was measured to be 0.8 and it was assured that the beam radiates as a gray-body.

A Hewlett Packard DC Power Supply, model #6652A, is connected to the two electrical grips of the beam fixture, and is controlled via a LabView virtual instrument (VI). The LabView VI controller was previously configured and designed at NASA LaRC. The VI controller makes sensor measurements through the infrared thermal imaging camera, the type-T thermocouples, and controls the power supply current output through general-purpose interface bus (GPIB) commands. Optimal gains are set to use proportional-integral-derivative (PID) control to supply current to raise the temperature of the SMAHC beam centerline to desired set points where data is recorded. The LabView VI system is capturing data from a laser displacement transducer (Keyence model LK-081). The laser displacement transducer was attached to an optical positioning traverse, which was used to precisely align the laser to the mid-span point of the SMAHC beam specimen, and calibrate the initial laser transducer/beam surface distance to zero. This was done before every run. Therefore as the VI controller runs through a thermal cycle, the beam temperature is sensed by the thermal camera, current is applied to raise the temperature from 23 °C (74 °F) (ambient) to 121 °C (250°F) capturing set points in increments of every 5.55°C (10 °F), and the mid span displacement values are being recorded continuously approximately every 4.2 seconds during the thermal cycle except for beam 3 run 2 and beam 3 run 3, in which laser data was captured at set-point only. One entire cycle took approximately 480 seconds. As an added feature the VI controller was designed to automatically trigger the PMI imaging system to capture images at every set point during a thermal cycle. Therefore, the laser displacement transducer is capturing the mid-span displacement measurements, and the PMI system is capturing the full-field displacement of the SMAHC beam specimen, throughout the thermal cycle. Figure 2.5 is a schematic showing an overview of the components and functionality of the experimental set-up. Figure 2.6 is an image of the entire experimental set-up and all measurement components can be seen. The PMI measurement of full-field displacement will be explained in more detail in the subsequent section.

The results of the full-field displacement measurement give great insight into the buckling behavior of the beam, and initial imperfection measurements can be captured. Also the PMI displacement measurements can be compared to the laser displacement transducer measurements of the SMAHC beam mid-span to reduce uncertainty.

2.3 Projection Moire' Interferometry

Projection Moire' Interferometry is an optical surface deformation measurement technique used to measure the full-field deformation of a structure. PMI is an optically simple, non-contacting measurement technique used since the 1970's for surface topology and shape characterization^{33,34}. A projection system with an installed Ronchi ruling is used to project a grid of equally spaced, parallel lines onto the structures surface. A CCD camera is positioned to view the structure at some angle θ inclined from the projector optical axis, which is perpendicular to the structure surface. Images are captured of the projected grid lines during the initial unloaded state and during loading of the structure. As previously mentioned for this experiment, images were captured every 5.55°C (10°F) from 23-121°C (74-250°F). At each set-point the PMI system is triggered, and it takes 10 images and averages them. Image processing routines are used to remove camera perspective distortion and interfere the captured images with a numerically generated reference grid. This results in interferograms containing moire' fringes. The fundamentals of PMI measurement and its applications have been studied

and quantified at NASA LaRC by G.A. Fleming for use in wind tunnels³⁵. Figure 2.7 shows a schematic of the PMI imaging system.

Imagine that the grid lines are projected onto a flat surface located at coordinate z_0 in the schematic. The CCD camera captures this reference image. Then when the plate is deformed or translates in the z direction the spatial locations of the gridlines change, thus producing a deformed image. This change can be represented mathematically by distorting the reference image grid by this phase function:

$$\varphi(i, j) = \frac{2\pi z(x, y) \tan \theta}{d} \quad (1)$$

where $\varphi(i, j)$ is the spatial phase at a pixel in the CCD camera image plane corresponding to point (x, y) on the un-deformed object surface, $z(x, y)$ is the out-of-plane deformation at that point, and d is the distance between grid lines. It is known that taking the absolute difference of the reference grid and the deformed grid produces an interferogram. The interferogram will contain moiré fringes occurring when $\varphi(i, j) = 2\pi m$, thus:

$$z(x, y) = \frac{nd}{\tan \theta} \quad (2)$$

Therefore, the moiré fringes in each interferogram represent the contours of the deformation in the z direction. The fringe contour interval is then defined as:

$$\Delta z = \frac{d}{\tan \theta} \quad (3)$$

This is the basic idea of how the PMI measurement theory is implemented. Further techniques of image processing such as phase shifting, phase unwrapping, choosing anchor point, and grid-line nonlinearity issues are addressed in more detail in the following references^{35,36,37}.

2.4 Static Thermoelastic Response Experimental Results

Laser Displacement Transducer Results

The mid-span deflection measurements of the SMAHC beam2 and beam3, by the laser displacement transducer, are presented in Figure 2.8, 2.9, respectively. The figures show the mid-span deflection as a function of average temperature of the centerline along the length of the beam. Data from thermal cycles 1-9 on SMAHC beam specimen #2, and thermal cycles 1-10 on SMAHC beam specimen #3 are presented. The adaptive stiffening mechanism is evident in all runs for both beams. Recall that the austenite start temperature for the Nitinol ribbon is greater than the ambient temperature ($A_s > T_o$). Therefore, buckling of the clamped beam will occur immediately when the temperature of the beam begins to change. As the temperature of the beam is increased the midspan of the beam deflects until a critical temperature at which the SMA recovery forces overcome the in-plane compressive forces due to thermal expansion and the beam is rendered flat. The experimental data shows a relatively large variation between maximum buckling deflection. This is a highly nonlinear phenomenon and dependent upon many parameters such as initial deflection, initial stress, geometric imperfections, and

boundary conditions. Each thermal cycle test and possible reasons for the behavior will be described in the next paragraph.

In Figure 2.8 for beam 2, runs 1-9 are the first 9 thermal cycles on this beam specimen. In Figure 2.9 for beam 3, runs 1-10, correspond to thermal cycles 5-14. Actuator degradation with thermal cycle reduces the maximum tensile recovery force in the beam at higher temperatures. Figure 4.4 shows the measured recovery stress as a function of temperature for numerous thermal cycles of the pre-strained Nitinol ribbon used in this project. Notice, even at high thermal cycles the temperature range that corresponds to where the post-buckled deflection is recovered ($\sim 32\text{ }^{\circ}\text{C} - 65.5\text{ }^{\circ}\text{C}$) shows no significant degradation with thermal cycle. Therefore thermal cycle degradation is not a factor in the observed variation of maximum deflection. In run 1 for beam 2, and runs 1, 2, and 10 for beam 3 a relatively large max deflection occurs. All these runs occurred as the first thermal cycle on the SMAHC beam after a relatively long period of storage time, and could be attributed to moisture absorption in the beam. It is common for glass-epoxy composite materials to exhibit moisture absorption after relatively short periods of time. The absorption of moisture in the composite beam laminate could possibly cause swelling of the layers of the structure. The presence of moisture in the composite structure could enhance the thermal expansion effect at the initial temperature increase. As temperature continues to increase the maximum buckling deflection is increased and the point of deflection recovery is pro-longed to a higher temperature. It is likely that at some temperature the moisture is driven out of the structure, thus causing a rapid recovery of the deflection. This could be the explanation for the rapid deflection recovery observed in the large deflection cases. Beam 3 Run 1 was the first thermal cycle on the beam in approximately one year. Beam 3 Run 2 occurred 9 days after the first run. Beam 3 Run 10 occurred 14 days after the previous run. Beam 2 Run 1 was the first thermal cycle on the beam, which was fabricated approximately one year before the experiment. So, it seems probable that the buckling phenomenon and deflection behavior are very sensitive to hygrothermal effects, and indicates that the numerical modeling to match the buckling phenomenon will require precise knowledge of all parameters that can affect the environmental state of the beam.

Another contributing factor to the variation could also be a result of pre-tension on the SMA actuator leads once installed. It is important to have no stress present in the installed SMAHC beam initially, but it is also necessary to have the beam installed “taught” so the beam is not initially buckled. The experimental procedure involved pulling the leads “taught” just before clamping at the boundaries. It is a possibility that some pre-stress may be present in the SMA actuator ribbons initially before the run. Recall that the transformation temperatures are a function of stress, and typically vary linearly with applied stress. The buckling deflection is very sensitive to the recovery force of the SMA, which would be effected by the shift in the A_s transformation temperature. During the buckling and post-buckled state of the beam, there are two mechanisms competing. The compressive forces being generated due to thermal expansion, and the recovery stress that is generated at A_s temperature of the embedded SMA actuators. A small change in either mechanism could result in a large change in the deflection behavior.

It should also be mentioned that another possible contribution to the pre-stress variation could perhaps be due to small deformation of the Aluminum beam fixture in which the SMAHC beam is clamped within. During the experiment procedure thermal cycles were performed in succession, once the infrared thermal imaging camera measured the beam’s centerline cooling from elevated temperatures back to ambient ($\sim 74\text{ }^{\circ}\text{F}$). In cases, where the

thermal cycles were performed in quick succession, the Aluminum fixture may have been somewhat soaked with thermal energy, which it loses rather slowly relative to the SMAHC beam specimen. As a result, when the SMAHC beam was re-gripped during these cyclic runs the fixture could be continuing to lose heat and contract. Thus, the beam would be under compressive stress at the beginning of a thermal cycle, which was performed in quick succession from a previous one.

Another observation from the laser displacement data is the variation of the initial imperfection of the mid-span. Beam 2 seems to exhibit a larger variation in initial deflection values between runs, than does beam 3. This could be attributed to the fact that beam 2 had never been subjected to a thermal cycle before, thus the internal stress state probably has a large variation in the first couple of thermal cycles. After curing of the laminate, residual stresses are present in the composite matrix. Upon the first thermal cycle the largest recovery forces are seen within the beam, causing a large chance of internal slipping, and settling of the composites components during early runs. Thus the initial deflection of the mid-span, which is due to geometric imperfections of the composite, and also induced by the boundary condition imperfections of the fixture, could have larger variations if the internal state of the beam is changing. Another interesting observation is that during all runs for both SMAHC specimens the buckling phenomenon always occurred in the same direction towards the laser displacement transducer. For Beam 2 run 9 the SMAHC specimen was flipped over in the beam fixture, and still exhibited buckling towards the laser. This suggests that boundary conditions of the beam fixture are contributing to the initial shape, and buckling direction of the beams.

Following the static experiments in which the laser displacement data and PMI data was captured, another experiment was run to capture the geometric imperfections of the beam and capture the full-field initial shape of the SMAHC beam installed in the fixture to confirm the PMI results. The experiments uncovered some of the initial conditions contributing to the initial state of the beam.

The experimental configuration consisted of a Klinger Scientific motorized linear traverse and controlled via the Labview VI. The translation stage was mounted parallel to the SMAHC beam fixture with installed beam as seen in Figure 2.10. The laser displacement transducer was mounted to the translation stage, and traversed via a programmable stepper motor the length of the beam and recorded displacement measurements in .10 inch increments along the 18 inch length of the beam. This data shows the initial imperfection of the beam, when mounted. The laser is calibrated to zero at the left end of the beam from a front view, and all subsequent measurements during a run are relative to that first set point. Multiple cases were studied, and these experiments uncovered some interesting results.

The initial imperfection data was captured on the beams in one direction and then flipped to the other side in the beam fixture. These results in Figure 2.11 show that the SMAHC beams take on the same shape even once flipped. This figure shows the out of plane deflection of the beam at ambient temperature as a function of the length of the beam. These measurements represent the initial imperfection profile of the beam when installed in the fixture. Notice that the blue colored line represents the out of plane deflection measurement for beam 2. Then beam 2 was flipped over and installed again in the fixture, which it would be expected to see the opposite deflection profile. But the magenta line results for Beam 2 flipped produces the same deflection profile. This confirms that the boundary conditions are contributing to the initial shape of the beam. Approximately the same deflection profile results

for beam 3 specimen as well. The laser data is also compared to one of the data sets for the PMI absolute imperfection measurement. As will be explained in the next section the absolute PMI measurement is the first image of the beam captured at ambient differenced from a reference image of a perfectly flat calibration plate. It is evident in Figure 2.11 that the laser displacement initial imperfection results are in excellent quantitative agreement with the black dashed line representing the PMI absolute measurement at ambient temperature. This is true for all runs of the PMI absolute measurements for both beams at ambient and confirms that the PMI absolute measurements are correct.

An interesting observation is that the beam is skew in all cases from one grip to the other in Figure 2.11. At 18 inches represents the left boundary grip therefore it is expected that deflection measurement should be zero relative to the other right boundary grip. This was noticed in the PMI results and first attributed to the possibility of the calibration plate not being perfectly aligned with the beam fixture. But, the laser displacement measurements confirm that there is an offset in the actual fixture from one grip to the other while a beam is installed. A measurement of the distributed thickness of the Garolite G-10 insulation blocks that the beam is clamped within show that they are not symmetric. In fact the difference in thickness of the inside edges of the two back G-10 insulation blocks that the beam is clamped against have a difference of approximately .020 inches. This difference closely corresponds to the skewness observed in the PMI, and laser displacement measurements of the initial imperfection. Subsequent measurements using the laser displacement transducer traverse with multiple G-10 block arrangements were performed to show that the effect the boundary conditions have on the initial shape of the beam. The results in Figure 2.12 show a totally different initial shape of the beam for different orientations. The corresponding configurations are best described by the schematic showing the G-10 block arrangement and each G-10 thickness at the edges in Figure 2.13.

Thus, based on the above observations the laser displacement transducer translation experiments prove that the boundary conditions are the primary factor to the initial shape of the beam, and confirm the PMI absolute measurements at ambient. The offset of the beam between boundaries is a physical entity of the experimental results, but is just a rotation of the beam. All numerical modeling in ABAQUS will be relative to a flat plane, so for comparison purposes all skewness present in the initial geometric imperfection experimental data has been subtracted before input into the ABAQUS input file.

Projection Moire' Interferometry Results

The PMI measurements captured the full-field displacement of the beam and are represented as pixels. The full-field PMI images showed no variation in displacement in the vertical width direction, thus the centerline data points along the length of the beam are representative of the full-field image of the beam. The PMI data presented for this experiment shows the out of plane displacement of the centerline of the SMAHC beam for various SMA actuator temperatures. The x-axis represents the beam length. PMI data points were only captured for 0 - 17.83446 inches along the length of the beam due to the angle of the PMI projector creating a shadow at the right boundary. PMI data is relatively noisy due to surface roughness, and processing techniques. To adjust for this, experimental data was fit to a 6th order polynomial of the form: $Y = A + Bx + Cx^2 + Dx^3 + Ex^4 + Fx^5 + Gx^6$, in which data points from -1.006 to 0 and 18 to 19.012 inches were manually zeroed to produce accurate line fits representing the deformation profile of the beam. The zero padded data sections represent

the x-locations in the clamped boundaries and it is a fair assumption that displacement values are zero. Thus, the line fit was used to extrapolate data for the small beam length section from 17.83446 - 18 inches. The positive sense deformation represents deflection away from the PMI imaging system. An example of the captured PMI data and corresponding line fit for a differential measurement at 48.8 °C (120 °F) is presented in Figure 2.15 for Beam 2 Run 4.

There are two types of PMI measurements made for these experiments. As explained the PMI data can only represent deformation from an initial reference image. Differential measurements use the initial ambient temperature image as this reference image. This reference image is considered the zero state. Subsequent images taken as temperature increases are the deformations relative to the reference state. Therefore any initial imperfection of the SMAHC beam is not present in these measurements. Additionally, the skewness is not present in the differential measurements for the same reasons.

The other type of PMI measurement is the absolute measurement. In reality it is known that the SMAHC beam specimen in the initial ambient temperature is not perfectly flat, due to imperfections in the composite laminate lay-up, initial stress state within the beam, and imperfect boundary conditions. The absolute PMI measurements use a reference image of a flat plate in the plane of the beam fixture (See Figure 2.14). The first ambient temperature image captured from the SMAHC beam is then differenced with the flat plate image. This results in a measurement representing the full-field initial imperfection of the SMAHC beam at ambient temperature.

The Differential PMI measurements were post-processed by interfering the reference image at ambient with each elevated temperature image, which gives the difference. The fact that the reference image was skewed, as well as all elevated temperature images it is differenced with, results in no offset present in the differential measurements. Therefore the confirmed initial imperfection, with skewness subtracted off, can be added to each differential measurement to give the absolute shape of the beam for all temperatures in order to show comparison with the numerical simulations. Each run's absolute measurement, giving the initial geometric imperfection, was added to each differential measurement. Therefore, there now is a representative absolute measurement for every temperature in 5.55°C (10°F) increments between ambient and 121.11 °C (250 °F). The PMI results are shown for selected runs 1, 4, and 8 for beam 2, and beam 3 respectively in Figures 2.16-2.21. The plots show the full field out of plane deflection of the beam for a few individually selected temperatures. These presented results in the aforementioned figures show the same trends as all runs, which are included in Appendix A. Notice that in all runs the initial shape of the beam takes on the same S-shaped geometric imperfection at ambient temperature. This will be the initial geometric imperfection data input into ABAQUS for accurate modeling of the experiments. Also notice that the adaptive stiffening is also evident in all the PMI data and matches the laser displacement results for the midpoint of the beam.

The midspans of the centerline PMI deflection profiles were extracted for each temperature and plotted with the laser displacement transducer midpoint deflection measurements in Figure 2.22, and Figure 2.23 for beam 2 and beam 3 respectively. It is evident that there is good agreement between the two measurements. Note that there are fewer data points making up the PMI data curve because there is only PMI midspan data at the temperature set points. Also, small differences in the data sets can be attributed to the fact that the PMI data system was triggered to take data once the temperature reached a certain set point. The PMI system is triggered after the set point temperature is reached and laser data is already

written. Thus, 10 averages are collected as the thermal controller starts raising the temperature to achieve the next set-point. A similar scenario is likely in Beam 3 Run 1 because this is the only run where the control voltage was operated manually. Therefore there is a greater chance that the set point temperature drifted from the desired temperature by the time the PMI was manually triggered. This can explain the large difference in this particular data set. There are also small differences between data points at ambient temperature. This can be attributed to the fact that they are two separate measuring devices that are not referenced to the same initial position. The midspan data point for the PMI is referenced to the flat calibration plate image in the plane of the beam, whereas the laser displacement transducer's initial data point is referenced to the beam's flat position at 121.1 °C (250 °F).

Overall the PMI measurements prove to be extremely accurate, and in excellent agreement with the laser displacement transducer measurements. This validates the accuracy of the PMI measurement technique for this experiment. The PMI measurements give additional insight into the full-field deformation of the SMAHC beam throughout a thermal cycle, and give the important initial imperfection data to be used for accuracy in numerical modeling.

Chapter 3

EXPERIMENTAL MEASUREMENTS OF THE DYNAMIC RESPONSE OF THE SMAHC BEAM

The dynamic response chapter is arranged as follows. First, a background is given on the dynamic response measurement of the SMAHC beams. Then the experimental set-up and instrumentation functionality are described. Then a brief overview of the post-processing of the captured data is presented. Finally, experimental results of the SMAHC beam specimen's responses are presented and compared for a repeatability investigation.

3.1 Background

All the SMAHC beam vibration results in this study result from random base acceleration excitation. Resulting responses will be presented at various temperatures corresponding to the different stiffness states during the thermomechanical response. Using a random inertial excitation requires a statistical analysis to be used to process the response data. Randomness in vibration analysis can be thought of as the result of a series of experiments all performed in an identical fashion under identical circumstances, each of which produces a different response⁴². Multiple time histories of the input and corresponding responses are sampled. From these multiple samples Fast Fourier Transforms can be done and averaged to produce dynamic response characteristics. By demonstrating control over the dynamic response, i.e. adaptive stiffening, and RMS value reduction, implications of weight-efficient vibration and acoustic radiation reduction methods are eluded too. Also analysis of the resulting frequency responses will result in beneficial modal parameter values to improve modeling attempts. The beam fixture was designed not to have any resonance in the excitation bandwidth used in the experiment. Transducers are placed on the fixture and the beam in order to obtain the relative response of the SMAHC beam, and allow for comparison to response spectra generated numerically by ABAQUS. During excitation a thermal load will be applied to the beam as in the previous static tests. The SMAHC beam will be brought to a desired temperature set point, in which dynamic data will be captured. One run will consist of capturing dynamic data at all the chosen set points through a thermal cycle from ambient to 121.11 °C (250 °F).

3.2 Experimental Set-up

The aluminum beam fixture with installed SMAHC beam specimen is mounted to a large electromechanical shaker (Model T1000) configured horizontally and attached to a magnesium slip table, which oscillates over a bed of oil in a horizontal plane during operation, as seen in Figure 3.1. The excitation of the beam during operation is measured by 3 Endevco Model 2250A-10 accelerometers mounted in 3 different positions along the length of the SMAHC beam specimen. There are also 2 PCB model T352M92 accelerometers mounted to each end the beam fixture itself. Two of the PCB accelerometers are used for control of the shaker table, and the other two are used to subtract off the base motion from the absolute motion measured by the accelerometers mounted to the beam. The dynamic response

experiments of each SMAHC beam specimen consisted of 3 thermal cycles where the beam was heated from ambient to 121.11 °C (250 °F) in increments of 5.55 °C (10 °F). At each set point the dynamic acceleration data was captured. The experimental set up can be seen in Figure 3.1. The infrared thermal imaging camera is aligned at the end of the shaker table focused on the SMAHC beam, and used for control. A DC power supply voltage is applied to the beam via the Labview VI controller in the same manner as the static experiments described previously. The Labview VI controller is sensing measurements from thermocouples for monitoring, and the infrared thermal imaging camera for control. An addition to the Labview controller was made to hold once a set point temperature is reached, and then can be released when specified by the user. This allowed the dynamic data to be captured for that temperature, and then the set point is released and the beam's temperature is elevated to the next set point.

In Figure 3.2, there are Endevco (2250A-10) accelerometers mounted on the SMAHC beam in positions 1-3. Position 1 is 4.5 inches from the right mechanical grip from the back view, position 2 is at the midspan, and position 3 is 14.5 inches from the right mechanical grip. There are also 2 PCB (model T352M92) accelerometers mounted on the back of each of the mechanical gripping blocks. One pair is used for control of the shaker table, and the other pair is used to capture the fixture response. Time histories with a total length of 200 seconds were captured with a sampling rate of 1024 Hz to allow 50-frame averages with a bandwidth of 0-512 Hz and a frequency resolution of .25 Hz for every set point. The SMAHC beam was excited by random base acceleration over a 10-400 Hz bandwidth with a RMS value of .25 g. The excitation's power spectral density (PSD) is shown in Figure 3.3. All three response transducers are capturing acceleration data, and one pair of the fixture transducers are being integrated to displacement data, while the other pair for control of the shaker is capturing acceleration data. All of the transducers are connected to a Hewlett Packard VXI mainframe (model E8403A) with a 16 channel E1432A module data acquisition card. The dynamic data is captured and processed using MTS IDEAS software. Upon capturing all of the time histories for each temperature set point, the data is post-processed into relative response quantities by subtracting off the base acceleration. Then response quantities are generated including frequency response functions (FRF) between the beam specimen's response and the fixture's input, power spectral densities (PSD) of the acceleration input and relative beam responses, and coherence functions, which indicate data quality in general. A schematic of the dynamic experimental set-up can be seen in Figure 3.4.

Before the dynamic response experiment the beam specimen was weighed and installed into the beam fixture. Beam 2's mass without mounted transducers was 75.97e-3 kg (.1675 lbf) and 79.15e-3 kg (.1745 lbf) with mounted transducers. Beam 3's mass without mounted transducers was 74.84e-3 kg (.1650 lbf), and 78.25e-3 kg (.1725 lbf) with transducers. Just prior to activating the excitation to the base, the mechanical and electrical grips are torqued to 13.56 Nm (120 in lbf). Once the random broadband excitation begins the thermal controller is activated and holds at the designated set point. The dynamic data acquisition system then acquires the acceleration data for all accelerometers. Following three runs for each beam the acceleration time histories are post-processed, which included averaging 50 times.

3.3 Dynamic Response Data Post-Processing Overview

In general a transducer used to measure input and output during a vibration test usually contains noise. Additionally, performing a number of identical tests and averaging the results increase confidence in a measurement of random vibration. In this experiment it was desirable

to obtain displacement response data, because it is more intuitive. Direct hardware integration was attempted during testing by PCB model 480B10 Signal Conditioners. In this case 4-second time history samples were taken to construct a 200 second time history for each temperature set point in MTS IDEAS. The integrated time signals were swamped with a low frequency noise. The acceleration time signals were processed, and the FRF's and PSD's showed large low frequency peaks representing the noise. Therefore, upon integration of the acceleration data in the frequency domain the low frequency noise dominates the resulting displacement time history. Thus, it was determined that all transducers would capture the acceleration data, and integration to displacement would be performed offline. A MATLAB m-file was written to perform a Fast Fourier Transform (FFT) on the acceleration time history, integrate in the frequency domain to get displacement FFT values, "zero out" the low frequency noise below 10 Hz, and then perform an inverse FFT to convert to a displacement time history data file. Additionally this m-file computes the displacement PSD's, and RMS values from the generated displacement time history (See attached m-file in Appendix B).

The Fast Fourier Transform is defined as

$$X(f, t) = \Delta t \sum_{n=0}^{N-1} x_n \exp[-j2\pi f n \Delta t] \quad (4.1)$$

assuming that there is a time history record $x(t)$ that is sampled at N equally spaced points a with time increment Δt , where Δt has been selected to produce a sufficiently high cutoff frequency. Therefore, $x_n = x(n\Delta t)$ where $n = 0, 1, 2, \dots, N-1$. The selection of the corresponding frequency values for the computation of $X(f, t)$ is

$$f_k = \frac{k}{T} = \frac{k}{N\Delta t} \quad k = 0, 1, 2, \dots, N-1 \quad (4.2)$$

At these particular frequencies, the transformed values give the Fourier components defined as

$$X_k = \frac{X(f_k)}{\Delta t} = \sum_{n=0}^{N-1} x_n \exp\left[-j \frac{2\pi k n}{N}\right] \quad k = 0, 1, 2, \dots, N-1 \quad (4.3)$$

The Fourier components repeat after the index number $k=N/2$ since the Nyquist frequency occurs at this point. Thus, in the m-file the corresponding frequency vector generated for the Fourier components is folded back on itself in order to retain the phase information to transform back to the time domain.

Matlab generates the PSD's using the specified time data, number of points per data segment, sampling rate, window vector, and number of points to overlap. The output of the PSD function in Matlab must then be normalized to the Nyquist frequency to obtain the proper units of $(\text{in})^2/\text{Hz}$. The RMS value is then calculated from the auto spectra (PSD) values. In Figure 3.4, a particular displacement PSD at ambient temperature generated by the m-file is plotted with its corresponding acceleration PSD to confirm that the m-file is correct. It is observed that the low frequency noise is filtered out, and the frequency information is retained, providing excellent correlation with its corresponding acceleration PSD.

3.4 SMAHC Beam Dynamic Response Experimental Results

The experimental behavior of the SMAHC beam specimen observed during dynamic testing will briefly be described. As described in chapter 3, the beam exhibits a thermal post-buckling deflection over a particular range of temperatures. Within this temperature range the beam undergoes interesting dynamic responses because the stiffness of the beam is changing rapidly. Recall from the post-buckling analysis in chapter 2 that the stiffness theoretically drops to zero at the point where the beam loses stability and buckles. When the beam is in the post-buckled state the stiffness increases with deflection. When the SMA actuators are activated and return the beam flat, the stiffness again decreases but rapidly increases with continued heating from this state. For accurate numerical predictions in this temperature range a nonlinear dynamic analysis is needed, and will prove difficult to get good correlation for the simple fact that the beam's dynamic characteristics are changing rapidly. During excitation of the beam, its relative response was very noticeable at temperatures where the SMA actuators were not activated; where-as at high temperatures the relative response was small, and unnoticeable once the SMA ribbon is fully activated. Dynamic results will be presented for these temperature ranges. The SMAHC beam is returned to the flat configuration at approximately 65.55 °C (150 °F).

In Table 3.1 and Table 3.2 the RMS displacement values are presented as a function of temperature for all 3 positions on beam 2, and beam 3 respectively. The results show a decrease in RMS displacement of the beam with increasing temperature, which is evidence of the adaptive stiffening of the beam. The modal parameter estimates for beam 2 and beam 3 were obtained and are presented in Table 3.3 and Table 3.4 for each run. The modal damping ratio estimates are particularly useful as input into the numerical modeling of the experiments in ABAQUS. These modal damping ratio values are obtained in MTS IDEAS by performing a single degree of freedom curve fit (SDOF method). In this method each peak is analyzed by assuming that it is the frequency response of a SDOF system. This assumes that near each resonant peak, the FRF is dominated by that single mode. The damping estimates for mode 1 and mode 3 show a decrease in damping from the non-activated state relative to the high temperature activated state of the SMA. Interestingly, at the higher temperatures near 121.1 °C (250 °F) the damping estimates begin to increase slightly. This may be attributed to the glass epoxy matrix material heating up and softening, and is not associated with the SMA actuator material.

In Figures 3.6-3.11 the displacement PSD's for selected temperatures of 23.3 °C (74 °F), 71.1 °C (160 °F), 93.3 °C (200 °F), and 121.1 °C (250 °F) are presented for the various positions along the SMAHC beam specimens. The PSD's for position 2 differ from the corresponding PSD's for positions 1 and 3 in that the midspan of the beam does not contain the anti-resonant peaks between mode 1 and mode 3 resonance peaks. Also position 2 contains a larger displacement RMS value, which makes sense at the midspan of the beam. The experimental results show excellent repeatability between runs 1, 2, and 3, as well as between beam 2 and beam 3. Therefore the presented data sets in Figures 3.6- 3.11 are representative of all other captured dynamic data. The PSD's for both beams at all positions demonstrate the stiffening effect of the SMA actuators as the modal frequencies of the response are increased with increasing temperatures above 60 °C (140 °F). Figure 3.12 best shows the variation of the modal frequencies with temperature. Notice that the fundamental frequency increases from 30.1 Hz to 125.1 Hz from ambient temperature to 121.1 °C (250 °F). Also, mode 3's frequency nearly is increased out of the bandwidth of excitation.

Thus the dynamic response experiments demonstrate the adaptive stiffening mechanism of the embedded SMA actuator ribbons. The dynamic data gives a good overview of the full dynamic behavior for multiple positions along the beam length. The fact that the RMS values decrease with temperature, and the beam is stiffened indicates the reduction in the dynamic response. This has implications of improving sonic fatigue, and noise transmission reduction. Finally, accurate modal parameter estimates are captured to include in the dynamic numerical modeling of the SMAHC beam in ABAQUS.

THERMOELASTIC CONSTITUTIVE MODELING FORMULATION

4.1 Background

The ECTEM developed by Turner³² makes use of experimentally measured engineering properties. This makes the ECTEM easily implemented into a commercial code that is capable of nonlinear thermoelastic analysis of composite materials. This chapter will briefly summarize the development of this model, to give the understanding of how the engineering property measurement becomes the determining parameter of the modeling. The model is based on a mechanics of materials approach and the reader is referred to numerous sources^{18,38,39,40}.

4.2 Thermoelastic Constitutive Model/Stiffness Property Formulation

Figure 4.1 shows a schematic of a representative volume element of the SMAHC laminate, within the plane of the structure. The principal material coordinates for the composite matrix are 1, and 2. Note that in general the figure can represent embedding between or within layers and no limitation is placed on SMA orientation relative to the composite matrix fiber directions. The following constitutive relation is the fundamental equation of the ECTEM developed by Turner³² for the SMA element in the 1-direction.

$$\sigma_{1a} = E_a(T) \left[\varepsilon_1 - \int_{T_0}^T \alpha_{1a}(\tau) d\tau \right] \quad (4.1)$$

where, E_a is the Young's modulus of the SMA, ε_1 is the strain in the 1-direction, α_{1a} is the coefficient of thermal expansion (CTE). This equation represents the stress-strain relation specifically for the SMA material only (hence the subscript a for actuator). The key feature of

this constitutive relation is the $-E_a(T) \int_{T_0}^T \alpha_{1a}(\tau) d\tau$ term. This term embodies the effects of both

the thermal strain and transformational strain of the SMA. In the constrained recovery application, this term is related to the recovery stress, and elastic modulus of the SMA *i.e.* $\sigma_r(T, \varepsilon_p)$, and $E_a(T)$, still capturing the nonlinear effects when the temperature is above austenitic start ($T > A_s$).

$$-E_a(T) \int_{T_0}^T \alpha_{1a}(\tau) d\tau = \sigma_r \quad \text{or} \quad \int_{T_0}^T \alpha_{1a}(\tau) d\tau = -\frac{\sigma_r(T, \varepsilon_p)}{E_a(T)} \quad (4.2)$$

When the temperature is below austenitic start ($T < A_s$) the thermoelastic relation remains the same, and the ECTE of the SMA is due to thermal expansion only, and can be measured

experimentally. Therefore, the temperature dependent constitutive relation in the 1-direction for the SMA actuator specific to constrained recovery can be expressed as:

$$\sigma_{1a} = E_a(T) \left[\varepsilon_1 - \int_{T_0}^T \alpha_{1a}(\tau) d\tau \right] \quad T < A_s \quad (4.3)$$

$$\sigma_{1a} = E_a(T) \left[\varepsilon_1 + \frac{\sigma_r(T, \varepsilon_p)}{E_a(T)} \right] \quad T \geq A_s$$

Only the engineering properties of $\alpha_{1a}(\tau)$ for $T < A_s$ and σ_r, E_a for $T \geq A_s$ need to be measured in experimental set-ups that imitate the application (pre-strain $\varepsilon_p=4\%$, and boundary conditions=clamped) to implement the model. A similar constitutive relation evolves for principle material direction-2 (transverse).

$$\sigma_{2a} = E_a(T) \left[\varepsilon_{2a} - \int_{T_0}^T \alpha_{2a}(\tau) d\tau \right] \quad (4.4)$$

In this case the transverse CTE $\alpha_{2a}(\tau)$ is not related to the recovery stress, σ_r , and elastic modulus $E_a(T)$, but is still nonlinear due to the changing of the martensite and austenite phases.

Making the same assumptions, the same stress-strain relationship applies to the composite matrix material. Note, the 1,2-CTE's of the composite matrix are temperature dependent.

$$\sigma_{1m} = E_{1m} \left[\varepsilon_1 - \int_{T_0}^T \alpha_{1m}(\tau) d\tau \right] \text{ and } \sigma_{2m} = E_{2m} \left[\varepsilon_{2m} - \int_{T_0}^T \alpha_{2m}(\tau) d\tau \right] \quad (4.5, 4.6)$$

Therefore, the elastic modulus, and CTE in both directions must be measured experimentally as functions of temperature.

Now, the classical mechanics of materials approach to stiffness³⁸ can be implemented to define the material properties of the whole SMAHC lamina in terms of its constituents' measured properties. Imagine that there is only stress present in the 1 direction. The assumption is made that the strains in the SMA fiber direction are the same, as the fibers in the composite matrix, thus making the plane lamina sections perpendicular to the 1-direction remain plane after stressing. The resultant force in the 1-direction can be defined as

$$\sigma_1 A_1 = \sigma_{1a} A_a + \sigma_{1m} A_m \quad (4.7)$$

where, A_1 , A_a , and A_m are the cross-sectional areas of the SMAHC lamina element, SMA element, and the composite matrix element, respectively. Then the definition of the average stress for the SMAHC lamina element is

$$\sigma_1 = \sigma_{1a} \nu_a + \sigma_{1m} \nu_m \quad (4.8)$$

where, $\nu_a = A_a/A_1$ and $\nu_m = A_m/A_1$ are the volume fractions of SMA and composite matrix, respectively. Then, the stress-strain relationship for each constituent is substituted resulting in:

$$E_1 \left[\varepsilon_1 - \int_{T_0}^T \alpha_1(\tau) d\tau \right] = E_a \nu_a \left[\varepsilon_1 - \int_{T_0}^T \alpha_{1a}(\tau) d\tau \right] + E_{1m} \nu_m \left[\varepsilon_1 - \int_{T_0}^T \alpha_{1m}(\tau) d\tau \right] \quad (4.9)$$

From this expression the definition of the SMAHC lamina's elastic modulus and CTE in the 1-direction are formulated.

$$E_1 = E_a \nu_a + E_m \nu_m \quad \text{and} \quad \int_{T_0}^T \alpha_1(\tau) d\tau = \frac{E_a \nu_a \int_{T_0}^T \alpha_{1a}(\tau) d\tau + E_{1m} \nu_m \int_{T_0}^T \alpha_{1m}(\tau) d\tau}{E_a \nu_a + E_{1m} \nu_m} \quad (4.10, 4.11)$$

$$\text{where, } \text{sgn}(\alpha_{1a}) = \begin{cases} +1 & T < A_s \\ -1 & T \geq A_s \end{cases}$$

This formulation for the elastic modulus E_1 is physically analogous to the stiffness calculation of two springs in parallel. The similar analogy can be made for the modulus definition E_2 in the transverse direction of the SMAHC lamina. In this case, assume a uniform stress in the 2-direction only. The strain differs in each constituent, therefore an expression representing the total elongation is written.

$$\varepsilon_2 = \varepsilon_{2m} \nu_m + \varepsilon_{2a} \nu_a \quad (4.12)$$

Substituting for the strain, from equations (2.4, 2.6) results in:

$$\frac{\sigma_2}{E_2} + \int_{T_0}^T \alpha_2(\tau) d\tau = \frac{\sigma_2 \nu_a}{E_a} + \frac{\sigma_2 \nu_m}{E_{2m}} + \int_{T_0}^T [\alpha_{2a}(\tau) \nu_a + \alpha_{2m}(\tau) \nu_m] d\tau \quad (4.13)$$

Thus, the Young's modulus and CTE for the SMAHC lamina in the 2-direction result:

$$E_2 = \frac{E_{2m} E_a}{(E_{2m} \nu_a + E_a \nu_m)} \quad \text{and} \quad \int_{T_0}^T \alpha_2(\tau) d\tau = \int_{T_0}^T [\alpha_{2a}(\tau) \nu_a + \alpha_{2m}(\tau) \nu_m] d\tau \quad (4.14)$$

In this case, the formulation for the Young's Modulus in the 2-direction (E_2) is analogous to two springs in series. The same mechanics of materials approach can be used to define the SMAHC lamina's Poisson's ratio, ν_{12} , and shear modulus of a lamina, G_{12} .

The Poisson ratio is similar to the derivation of the Young's modulus E_1 . Assuming that there is a uniform stress in the 1-direction only on the SMAHC lamina, there is a negative deformation present in the 2-direction, Δ_w , due to the strain in the 1-direction. Therefore this deformation in the 2-direction can be represented as

$$\Delta_w = -W\varepsilon_2 \quad (4.15)$$

where W is the width of the SMAHC lamina (Fig 4.1). The Poisson's ratio is defined as

$\nu_{12} = -\frac{\varepsilon_2}{\varepsilon_1}$, therefore the transverse deformation can be represented as

$$\Delta_w = W\nu_{12}\varepsilon_1 \quad (4.16)$$

Additionally the same transverse deformation can be represented by the sum of the transverse deformations in the SMAHC lamina constituents, Δ_{mW} and Δ_{aW} .

$$W\nu_{12}\varepsilon_1 = \Delta_{mW} + \Delta_{aW} \quad (4.17)$$

Similar in the analysis for the transverse Young's modulus E_2 , the deformations Δ_{mW} and Δ_{aW} are approximately

$$\Delta_{mW} = W\nu_m\nu_m\varepsilon_1 \quad (4.18)$$

$$\Delta_{aW} = W\nu_a\nu_a\varepsilon_1$$

Thus, upon substitution of (2.18) into (2.17) and division by $W\varepsilon_1$, the expression for the SMAHC lamina Poisson's ratio is

$$\nu_{12} = \nu_m\nu_m + \nu_a\nu_a \quad (4.19)$$

Finally, the formulation of the in-plane shear modulus, G_{12} , of the SMAHC lamina is formulated by the assumption that the shearing stresses on the SMA fiber and the matrix are the same. The basic assumption can be made that,

$$\gamma_m = \frac{\tau}{G_{12m}} \text{ and } \gamma_a = \frac{\tau}{G_a} \quad (4.20)$$

Let Δ represent the total shearing deformation due to shear stress, then

$$\Delta = \gamma W \quad (4.21)$$

And similarly to the previous formulations, the shearing deformation can also be represented by the SMAHC lamina constituent's deformations.

$$\Delta = \Delta_m + \Delta_a = \nu_m W \gamma_m + \nu_a W \gamma_a \quad (4.22)$$

Therefore,

$$\gamma = \nu_m \gamma_m + \nu_a \gamma_a \quad (4.23)$$

Realization that $\gamma = \frac{\tau}{G_{12}}$, and substitution of equation (4.20) into (4.23) yields the expression for the in-plane shear modulus of the SMAHC lamina.

$$G_{12} = \frac{G_{12m} G_a}{\nu_m G_a + \nu_a G_{12m}} \quad (4.24)$$

Now the engineering properties of the SMAHC lamina have all been formulated in terms of the individual material constituents (Glass-Epoxy Matrix, and NiTi-SMA), and include the thermo-elastic effects due to the ECTE. These properties of the constitutive materials can all be measured. Implementing the stress-strain relationships of an orthotropic material lamina under plane stress will complete the development of the constitutive relations of a SMAHC lamina.

4.3 Stress-Strain Relation for Orthotropic Material

In a lamina if there are two orthogonal planes of material property symmetry for a material, and symmetry exist relative to a third mutually orthogonal plane, the stress-strain relations in coordinates aligned with principal material directions are defined as an orthotropic material. If an orthotropic material is subjected to a plane stress state ($\sigma_3=0, \tau_{23}=0, \tau_{31}=0$), the three-dimensional strain-stress relation below

$$\begin{Bmatrix} \varepsilon_1 \\ \varepsilon_2 \\ \varepsilon_3 \\ \gamma_{23} \\ \gamma_{31} \\ \gamma_{12} \end{Bmatrix} = \begin{bmatrix} D_{11} & D_{12} & D_{13} & 0 & 0 & 0 \\ D_{12} & D_{22} & D_{23} & 0 & 0 & 0 \\ D_{13} & D_{23} & D_{33} & 0 & 0 & 0 \\ 0 & 0 & 0 & D_{44} & 0 & 0 \\ 0 & 0 & 0 & 0 & D_{55} & 0 \\ 0 & 0 & 0 & 0 & 0 & D_{66} \end{bmatrix} \begin{Bmatrix} \sigma_1 \\ \sigma_2 \\ \sigma_3 \\ \tau_{23} \\ \tau_{31} \\ \tau_{12} \end{Bmatrix} \quad (4.25)$$

where $[D]$ is the compliance matrix, is reduced to the following stress-strain relation upon inversion.

$$\begin{Bmatrix} \sigma_1 \\ \sigma_2 \\ \tau_{12} \end{Bmatrix} = \begin{bmatrix} Q_{11} & Q_{12} & 0 \\ Q_{12} & Q_{22} & 0 \\ 0 & 0 & Q_{66} \end{bmatrix} \begin{Bmatrix} \varepsilon_1 \\ \varepsilon_2 \\ \gamma_{12} \end{Bmatrix} \quad (4.26)$$

where $[Q]$ is the reduced stiffness matrix of a composite lamina. This comes from Hooke's Law in its most basic form. This is then implemented for a SMAHC lamina, which includes the constitutive relations formulated previously in section 4.2.

$$\begin{Bmatrix} \sigma_1 \\ \sigma_2 \\ \tau_{12} \end{Bmatrix} = \begin{bmatrix} Q_{11} & Q_{12} & 0 \\ Q_{12} & Q_{22} & 0 \\ 0 & 0 & Q_{66} \end{bmatrix} \begin{Bmatrix} \varepsilon_1 \\ \varepsilon_2 \\ \gamma_{12} \end{Bmatrix} - \begin{bmatrix} Q_{11} & Q_{12} & 0 \\ Q_{12} & Q_{22} & 0 \\ 0 & 0 & Q_{66} \end{bmatrix} \int_{T_0}^T \begin{Bmatrix} \alpha_1(\tau) \\ \alpha_2(\tau) \\ 0 \end{Bmatrix} d\tau \quad (4.27)$$

The elements of the reduced stiffness matrix $[Q]$ are related to the engineering properties through the following equations.

$$Q_{11} = \frac{E_1}{1 - \nu_{12}\nu_{21}}, \quad Q_{12} = \frac{\nu_{12}E_2}{1 - \nu_{12}\nu_{21}}, \quad Q_{22} = \frac{E_2}{1 - \nu_{12}\nu_{21}}, \quad Q_{66} = G_{12} \quad (4.28)$$

Recall, that these engineering properties of the SMAHC lamina have been defined in terms of the lamina material constituents (glass-epoxy, SMA).

$$\begin{aligned} E_1 &= E_a \nu_a + E_m \nu_m & E_2 &= \frac{E_{2m} E_a}{(E_{2m} \nu_a + E_a \nu_m)} \\ \nu_{12} &= \nu_m \nu_m + \nu_a \nu_a & G_{12} &= \frac{G_{12m} G_a}{\nu_m G_a + \nu_a G_{12m}} \end{aligned} \quad .$$

$$\int_{T_0}^T \alpha_1(\tau) d\tau = \frac{E_a \nu_a \int_{T_0}^T \alpha_{1a}(\tau) d\tau + E_{1m} \nu_m \int_{T_0}^T \alpha_{1m}(\tau) d\tau}{E_a \nu_a + E_{1m} \nu_m} \quad \text{where } \text{sgn}(\alpha_{1a}) = \begin{cases} +1 & T < A_s \\ -1 & T \geq A_s \end{cases} \quad .$$

$$\int_{T_0}^T \alpha_2(\tau) d\tau = \int_{T_0}^T [\alpha_{2a}(\tau) \nu_a + \alpha_{2m}(\tau) \nu_m] d\tau \quad (4.29)$$

The above SMAHC constitutive relation (4.27) is for a lamina. This lamina will now be considered a general k-th orthotropic layer of a laminate, with an arbitrary orientation angle θ , from the principal material direction-1, from Figure 4.1. Below are the transformation equations for expressing stress and strain in an x-y coordinate system in terms of stress and strain in a 1-2 principal material direction.

$$\begin{Bmatrix} \sigma_x \\ \sigma_y \\ \tau_{xy} \end{Bmatrix} = [T]^{-1} \begin{Bmatrix} \sigma_1 \\ \sigma_2 \\ \tau_{12} \end{Bmatrix} \quad \text{and} \quad \begin{Bmatrix} \varepsilon_x \\ \varepsilon_y \\ \frac{\gamma_{12}}{2} \end{Bmatrix} = [T]^{-1} \begin{Bmatrix} \varepsilon_1 \\ \varepsilon_2 \\ \frac{\gamma_{12}}{2} \end{Bmatrix} \quad (4.30)$$

$$\text{where } [T] = \begin{bmatrix} \cos^2 \theta & \sin^2 \theta & 2 \sin \theta \cos \theta \\ \sin^2 \theta & \cos^2 \theta & -2 \sin \theta \cos \theta \\ -\sin \theta \cos \theta & \sin \theta \cos \theta & \cos^2 \theta - \sin^2 \theta \end{bmatrix}. \quad \text{Using the above transformations}$$

(2.30), the thermoelastic constitutive equation for the kth layer of a SMAHC laminate in an arbitrary orientation becomes

$$\begin{Bmatrix} \sigma_x \\ \sigma_y \\ \tau_{xy} \end{Bmatrix} = [\bar{Q}]_k \begin{Bmatrix} \varepsilon_x \\ \varepsilon_y \\ \gamma_{xy} \end{Bmatrix}_k - [\bar{Q}]_k \int_{T_0}^T \begin{Bmatrix} \alpha_x \\ \alpha_y \\ \alpha_{xy} \end{Bmatrix} \quad (4.31)$$

where

$$[\bar{Q}]_k = [T]^{-1} [Q]_k [T]^{-T} \quad (4.32)$$

There are some attractive characteristics of this model, which will be mentioned. In equation 4.27 it can be seen that the effective CTE in the 1-direction has an effect on the stress in the transverse direction, and vice-versa for the SMA actuator. This indicates that above A_s temperature the effects of the recovery stress in the 2-direction are included. Also, this model not only includes the nonlinear effects of the CTE in the 1-direction, but also in the 2-direction for the SMA actuator. Thus, the behavior of the SMA actuator element in the composite is accurately represented in the ECTEM.

Equation 4.31 represents the constitutive relation of the ECTEM in its final form for a SMAHC lamina layer. It is evident from the formulation that making use of the appropriate temperature dependent engineering property measurements and defining a composite laminate out of those material constituents is all that is needed for implementation of this model. Any commercial finite element code that is capable of analyzing composite laminates with temperature dependent material properties can then make use of the ECTEM. Work has been done in which an ECTEM research code was compared to ABAQUS, and MSC.Nastran and showed excellent correlation⁴¹.

In this work, the commercial finite element code, ABAQUS, is used in this way to model experimental results of SMAHC beam specimens with dimensions of 0.5588x0.0254x0.0019 m (22x1x0.078 in). A finite element mesh of 36x4 elements is defined with the two center element widths representing the portion of the laminate containing SMA material, and the two outer edge element widths representing the portion of the laminate containing glass-epoxy matrix material only. Each element is assigned the appropriate material stacking sequence and corresponding temperature dependent material properties. This is all accomplished in a single input file, in which a number of dynamic/static response analyses can be performed to accurately represent the experimental conditions. The corresponding material characterization, for the material constituents input into the modeling, was previously performed at NASA LaRC¹⁸. These material property measurements used for the numerical modeling in ABAQUS can be seen in Tables 4.1, 4.2, and 4.3. The Nitinol characterization stress-strain curves for 0% and 4% pre-strain, recovery force measurements as a function of thermal cycle at 4% pre-strain, and resulting elastic modulus as a function of temperature are shown in Figures 4.2, 4.3, 4.4, and 4.5 respectively. These ABAQUS input files will be more thoroughly described in chapter 5.

NUMERICAL MODELING OF SMAHC BEAM SPECIMENS IN THE COMMERCIAL FINITE ELEMENT CODE ABAQUS

5.1 Background

As previously mentioned, ABAQUS is a commercial finite element code capable of analysis of laminated composite structures with temperature dependent material properties. Recall that the beam specimen lamination involves the Nitinol ribbon material replacing the glass-epoxy matrix over approximately 0.45 inches of the beam width in the 0° layers. This can be conveniently modeled by using shell elements of two types; one having glass-epoxy layers only, and the other having alternating layers of 100% glass-epoxy and 100% Nitinol material. Therefore the ECTE model can easily be implemented by formulating the effective composite properties of each constituent material. This type of analysis has a variety of element types and solution techniques available to provide sufficient freedom to accurately model a wide range of experimental configurations. In this project an initial commercial input file for ABAQUS is generated which initially defines the SMAHC structures corresponding element, laminate, and material property definitions. Therefore, only a single temperature dependent material property data set for each constituent is defined, and used in the correct stacking sequence to define the laminate. Thus the laminated SMAHC materials, which are composed of orthotropic layers, are defined. The resulting input files in ABAQUS define the laminate by the *SHELL SECTION option, and the temperature dependent material properties are defined by the *MATERIAL, *ELASTIC, *EXPANSION options for each material constituent (SMA, glass-epoxy matrix). The user is referred to the ABAQUS User's and Reference Manuals and previous work done at NASA LaRC⁴¹. Once the element and material definitions are defined, the ABAQUS input files specify thermal and dynamic loads, and solution techniques. The ABAQUS input files will be described briefly below, and a specific input file representative of the presented modeling cases can be seen in the Appendix D.

The unsupported dimensions of the SMAHC beam are 0.4572x0.0254x0.0019 m (18x1x0.078 in). This section of the SMAHC beam is modeled by 36x4 type S4 quadrilateral shell elements in ABAQUS. As seen in Figure 5.1, the two center element widths (black) represent the hybrid composite stacking sequence (45/0/-45/90)_{2s} with the SMA comprising the 0° layers, and the two edge element widths (gold) represent the composite stacking sequence (45/0/-45/90)_{2s} consisting of all glass-epoxy material. Each glass-epoxy layer has a nominal thickness of 1.27e-4 m (.005 inches), and each Nitinol ribbon section has a thickness of 1.5e-4 m (.006 inches). The graphical representation of the beam shows the nodes at each end under clamped conditions. Each defined node is represented by the red circle symbol.

The temperature dependent material properties for each constituent can be seen in the ABAQUS input file as seen in the Appendix D. These material properties are taken from the material characterization measurements listed in Tables 4.1, and 4.2. It should be mentioned that ABAQUS uses secant CTE values as input for thermal expansion and not thermal strain

($\epsilon_T = -\frac{\sigma_r}{E} = \int_{T_0}^T \alpha d\tau \quad T > A_s$). Recall, that the thermal strain is a function of temperature, and

cycle number for the SMA material above the A_s temperature. Therefore the appropriate values of recovery stress and elastic modulus measurements in Table 4.2 were used to calculate the appropriate secant CTE for temperatures above A_s temperature. Another important detail worth noting is that these material characterization measurements were processed previously at NASA LaRC for low thermal cycles 1-4 only. This will be discussed in the subsequent sections and impact the comparison of experimental results to the numerical simulations. The appropriate CTE values for the Nitinol ribbons below the A_s temperature were taken from published data as were the transverse direction CTE values for martensitic temperature $6.6\text{e-}6$ $^{\circ}\text{C}$ ($3.67\text{e-}6$ $^{\circ}\text{F}$) and austenitic temperature $11\text{e-}6$ $^{\circ}\text{C}$ ($6.11\text{e-}6$ $^{\circ}\text{F}$). The transverse CTE values have been linearly interpolated between these two points to represent the values through the temperature range where the SME occurs.

Once the geometry, finite element mesh, and material properties are defined, the physical conditions of each experiment can be simulated. Some of the experimental measurements will serve as input into the numerical simulations. The ABAQUS input files consist of a sequence of several analysis steps progressing through the application of the thermal load. At certain load levels a desired equilibrium state is achieved, where the random response analysis is simulated for those states, thus determining the dynamic response. In each individual input file the actual measured thermal load from the thermal imaging camera for each thermal step to 121.1 $^{\circ}\text{C}$ (250 $^{\circ}\text{F}$) is applied to the SMAHC beam with clamped boundary conditions. Throughout the application of the thermal load a dynamic inertial loading is defined that represents the .25g RMS base excitation used in the dynamic experiments. The actual base excitation PSD measured from each experiment, see Figure 3.3 for an example, is input into the analysis by the *PSD-DEFINITION in ABAQUS. During the linear random response step analysis at the specified equilibrium states a modal approach is used incorporating the first 10 modes, in order to account for residual effects. The modal parameter estimates for mode 1 and 3 measured during the dynamic response experiments are used as input for damping estimates through modes 1 through 10 using the *MODAL DAMPING option. Additionally, the initial geometric imperfection measured by PMI measurements for the full-field displacement of the beam is input into the analysis by the *IMPERFECTION option, to assist in the nonlinear static solution procedure of the buckling/post-buckling of the beam. Recall the PMI measurements were for the centerline of the beam length only, but are representative of the full-width of the beam. Therefore a MATLAB m-file was written which linearly interpolates the beam length centerline initial imperfection measurements to nearest nodes corresponding to the full field of the SMAHC beam (See m-file and corresponding data set in Appendix C).

In the subsequent sections the numerical simulation input files will contain the previously discussed experimental measurements, which are beam specimen and run specific. This should improve the accuracy of the numerical simulations. Results for the analysis of nonlinear static, and linear random dynamic responses will be presented and compared to experimental results.

5.2 Static Response Modeling Results in ABAQUS

The plots of midspan deflection of the SMAHC beam vs. average centerline temperature are presented for the experimental PMI measurements and the numerical predictions in ABAQUS. Recall, from the static thermoelastic response experiments that the thermal buckling maximum midspan deflection varies greatly from run to run, and may be

attributed to moisture absorption, and varying pre-stress. Thus the specifically chosen numerical simulations will be given the initial imperfection data for runs that correspond to the middle of the varying deflection range where repeated experimental results occurred.

As previously mentioned, during the numerical simulations the specific material property measurement data for each constituent (SMA, Glass-Epoxy) is input into the model. Looking at figure 4.4 the recovery force data shows that A_s temperature begins when stress is starting to be generated at 28 °C (82.4 °F). Isolength (constant strain) tests were performed on a nominal .254 m (10 inch) length of Nitinol ribbon material to obtain these recovery stress results as a function of pre-strain, and thermal cycle. Thermocouple's were used to measure the corresponding temperature. There is a large error associated with thermocouple measurement at high temperatures due to 'fin' effect. There is also error due to 'fin' effect even at low temperature if the thermocouple is attached to a small surface area, as the case with the SMA ribbon. This recovery stress data for thermal cycle 4 is used for numerical modeling, but it is suspected that there is some error in the corresponding temperatures. This is validated by a discrepancy in the measured A_s temperature by differential scanning calorimetry (DSC) measurements.

Figure 4.6 shows the DSC results for small SMA ribbon samples (<10mg). The exothermic and endothermic peaks correspond to the transformation of the SMA material. During the first-heat there is an ill-behaved endothermic peak associated with the austenitic transformation recovery shear deformation induced from cutting the samples. This peak was not repeatable after the first heat, where as the other endothermic peak was. Therefore the measured A_s temperature is near 40 °C (105 °F). These measurements are accurate and indicate a possible error with the recovery stress measurements. This will be shown in the results of the modeling.

For each static thermoelastic response simulation the corresponding experimental measurement for a given initial imperfection, and thermal load is plotted. The numerical simulations for the original material property measurements, and after shifting the recovery force data 10-20 °F to account for the possible measurement error are included. Material property data is input into ABAQUS as elastic modulus data (E) and coefficient of thermal expansion (CTE) data. Recall, from the model, that the Nitinol effective CTE values are obtained from the measured E and the measured recovery stress (σ_r) at temperatures above A_s . Therefore the σ_r data is shifted and the corresponding CTE values are obtained from equation 4.2. These shifted CTE values are then used as input into ABAQUS to adjust for the measurement error.

In Figure 5.2 the predicted static response for Beam 2 Run 6 is shown. This numerical prediction for clamped boundary conditions, and the original recovery stress (CTE) measurements indicates that the SMA recovery force is overcoming the compressive forces due to expansion at a lower temperature than indicated by experiment, thus resulting in a lower max deflection, and smaller post-buckled temperature range (see green dashed line). The recovery stress measurements were shifted 15 °F and the corresponding new CTE values were input instead. This results show great qualitative agreement between the numerical simulation and the experimental measurement (See blue dashed line). The same results were produced in multiple simulations for Beam 2 and Beam 3 (Figures 5.3 – 5.7). Some cases required varying shifts between 10-20 °F. These results indicate that the pre-stress initially present could be varying for run to run slightly affecting the recovery force behavior. These static experimental results are based on thermal cycles 5-14 for beam 3 and cycles 1-9 on beam 2. The recovery

force measurement data was only captured for thermal cycles 1-4. Therefore thermal cycle 4 data was used in modeling. This could be attributed to the small differences between experiment, and simulation. The recovery force data adjustment seems to give great qualitative agreement with experiment and indicates the sensitivity of the buckling behavior to the interaction between the SMA recovery stress generated and the compressive forces due to thermal expansion.

The recovery stress temperature shift now activates the recovery forces at the correct corresponding temperature to more accurately capture the actuation, which returns the midspan deflection to zero. In all simulations the measurements of the initial imperfection, the thermal load, and material property measurements were input directly into the model to achieve accuracy. These results verify the capability of the commercial finite element code ABAQUS, to accurately predict the static thermoelastic response of SMAHC structures by implementing the ECTE model. Additional material characterization measurements could be made for the recovery stress of the constrained Nitinol actuator ribbons using infrared thermal imaging to produce even more accurate material property data to be used in the model. This could even further improve the accuracy of the numerical prediction with the experimental results.

5.3 Dynamic Response Modeling Results in ABAQUS

Experimentally measured and numerically predicted displacement PSD's for measurement position 2, representing the midspan accelerometer, are shown for various temperature values in Figures 5.8-5.15. Results are presented only for beam 2 run 8 and beam 3 run 8, but are representative of all other dynamic results for that measurement position, and beam specimen. Dynamic response PSD's are presented for both beam specimens at 21.7 °C (71 °F), 71.1 °C (160 °F), 93.3 °C (200 °F), and 121.1 °C (250 °F). These temperature values demonstrate the stiffening of the beam due to the SMA actuation and the ability of the numerical simulation to accurately capture the effect. For these numerical simulations the adjusted recovery stress material data was input for the material properties (15 °F shift).

Recall, from experimental results in chapter 2 it was discovered that the boundary clamped G-10 insulation was unsymmetrical and the boundary conditions are contributing to the initial imperfection of the beam. Also the experimental initial imperfection measurements show that the boundary conditions are dominating in the initial shape of the beam. The fact that the G-10 insulation thickness was not uniform for all samples indicates that the boundary conditions are most likely not exhibiting perfectly clamped conditions, and would be difficult to accurately model. The unsymmetrical G-10 insulation clamps likely allow some torsional rotation of the beam at the boundary. This was attempted to be accounted for in the model by applying torsional spring elements to the 5th degree of freedom (out of plane of the beam) of the end nodes at the boundaries of the beam model. This is defined in ABAQUS by the *SPRING function. Torsional springs with a rate of 60 (in·lbf/rad) were applied to match the fundamental frequency.

As indicated in previous work¹⁸, in the physical system the beam continues through the mechanical grips and the Nitinol leads are terminated beyond that in the electrical grips. Therefore the main restraint for the Nitinol is the mechanical termination at the electrical grips. Thus, the compliance of the entire support structure needs to be considered. Although, Garolite G-10 material was used as insulation between the electrical and mechanical grips, it is likely that there is still some compression occurring, partially relieving the recovery stress. This effect was captured in the model by applying axial springs with a spring rate of 7000 (lbf/in) to each

of the nodes at the boundary of the beam model in degree of freedom 1 (in-plane). This spring rate was obtained by matching the fundamental frequency of the simulation to the measured fundamental frequency at the elevated temperature of 250 °F.

The same explanations described in the previous static thermoelastic response modeling sections correspond to the over prediction of stiffness initially seen in dynamic results. The application of the boundary springs previously discussed produce the PSD comparison in Figures 5.8-5.15, for beam 2 run 8 and beam 3 run 8 at position 2 (midspan). The displacement PSD predictions show excellent agreement with the experimental results. It can be seen that at 21.7 °C (71 °F), 71.1 °C (160 °F), 93.3 °C (200 °F), and 121.1 °C (250 °F) temperatures, the ABAQUS predicted responses closely correspond with the experimental modal frequency values and RMS displacement values. In Figures 5.16 and 5.17, the same temperature values are compared to the experimental measured PSD's for positions 1 and 3, along the length of the beam all in one plot. Again the ABAQUS predictions show excellent agreement with the experimental results in modal frequency values, and RMS displacement values.

In Figures 5.18-5.23 displacement PSD's of the numerical simulations and experimental dynamic responses are compared for temperatures corresponding to the buckled and post-buckled range of the SMAHC beam specimen. These particular data sets correspond to beam 3 run 1 of the dynamic experiments. This is the only dynamic experimental run in which dynamic data was captured through this temperature range of buckling/post-buckling. The static deflection behavior of the beam doesn't correspond closely the numerical simulation of the static deflection for this particular run in that temperature range. Therefore the PSD comparison at these temperatures is expected to suffer as well. If dynamic data was captured for this temperature range for the thermal cycles presented in Figures 5.2-5.7 then the post-buckled temperature range PSD's would be expected to compare reasonably well. Through this temperature range the beam goes through the buckling phenomenon in which the stiffness theoretically drops to zero. Once the beam is buckled the stiffness is increased, until the SMA recovery forces begin to return the buckling deflection back to a flat configuration. At this point the stiffness of the beam is decreasing. So during this temperature range the SMAHC beam exhibits complex dynamic behavior, and would be difficult to model accurately. The PSD comparison in Figures 5.18-5.23 demonstrates the difficulty in modeling this behavior with the current analysis, and the complex dynamic behavior evident in the experimental PSD's can be seen.

In Figure 5.18 the displacement PSD at ambient temperature 21.7 °C (71 °F) is plotted for position 3 along the length of beam 3. This particular dynamic response demonstrates some nonsymmetrical modes as seen by the additional spectral peaks in the experimental PSD. Also nonlinearity is demonstrated by peak shifting and peak broadening in the experimental PSD's. ABAQUS numerical model shows good agreement with the stiffness prediction even though a linear dynamic response is predicted. Recall that a linear random analysis is being implemented in ABAQUS to predict the dynamic response. That explains the difference in the PSD's comparison, but the modal frequency peaks still match indicating a good prediction of the stiffness state of the SMAHC beam. In Figure 5.19 the displacement PSD comparison for a temperature of 37.7 °C (100 °F) is shown for Beam 3 Run1 at position 3. At this temperature the beam has buckled. The experimental PSD's show again the complex nonlinear behavior of the dynamic response, and shows a slight increase in the fundamental frequency from the ambient state. The numerical simulation in ABAQUS does not agree with the experimental results in that it is predicting a large decrease in stiffness by the decrease in the modal

frequency values. The same prediction error is shown in Figure 5.20 at a temperature of 43.3 °C (130 °F). At this temperature, recovery stresses are being generated because it is above A_s temperature, but they have not overcome the compressive forces due to thermal expansion, thus the beam is still in a buckled state. The experimental PSD is again showing complex dynamic behavior by the nonlinear peaks. In Figure 5.21 the PSD comparison at 60 °C (140 °F) shows a good agreement in modal frequency values. At this temperature state the beam has been just rendered flat by the SMA recovery forces. Since the beam has just been returned flat it is still demonstrating some nonlinear dynamic behavior, but ABAQUS is able to make better predictions now using its linear analysis. Then in Figure 5.22 at 65.55 °C (150 °C) the experimental PSD shows that the linear dynamic behavior has returned as the beam is flat and an increase in stiffness is occurring. The ABAQUS numerical simulation now is in good agreement with the behavior for the rest of the temperature range and accurately predicts the stiffness of the structure as seen in subsequent Figure 5.23 at 71.1 °C (160 °F).

So the dynamic response modeling results demonstrate the ability of ABAQUS to accurately model the dynamic behavior of the SMAHC beam specimens' experimental results by using a linear random analysis. The adaptive stiffening effect and RMS values of the vibration are accurately predicted by input of the measured modal parameters, the random excitation from experiment, and the measured material properties of the constituents directly into the numerical model. Accurate simulations are produced in the temperature range below and above the buckling range, and demonstrate the stiffening effect of the embedded SMA actuators. An attempt to model the dynamic behavior through the temperature range, where buckling occurs, demonstrates that there is complex dynamic behavior occurring when the SMAHC beam is in this state. If the static deflection behavior of the beam corresponds closely to the numerical simulations as in Figures 5.2-5.7, it is expected that the numerical PSD prediction would correspond closely in this post-buckled temperature range except at the start of the buckling and at the point of returning flat. These two locations are theoretically the only cases where linear analysis fails due to the nonlinear and complicated dynamics. This limits the accuracy of a linear random analysis to predict the behavior. It would be desirable perhaps for application advantages to use Nitinol actuator ribbons with a Ni and Ti composition which produces an A_s temperature below ambient temperature to avoid the buckling behavior of the structure.

CONCLUSIONS

This study consisted of a thorough experimental investigation into the response behavior of SMAHC beams. The attractive functionality of SMA's was demonstrated as an adaptive stiffening mechanism to composite beam specimens in all experimental cases. The ECTE constitutive model was implemented into the commercial finite element code ABAQUS, to accurately predict the response of the SMAHC structure. The experimental measurement investigations uncovered important contributing factors to the behavior of the SMAHC beam, such as initial geometric imperfections, contributions of the boundary conditions, distributed thermal load over the beam, and the real base excitation that was used to induce the dynamic response. These measurements, and discoveries were able to be accounted for in the numerical modeling to produce an accurate prediction of the SMAHC beam responses, and further validate the use of the ECTE model to be used in the commercial finite element code ABAQUS.

Numerous experimental tests were performed to determine the thermoelastic response in a clamped boundary configuration with a thermal load applied via resistive heating. The out of plane deflection of the midspan was measured as a function of temperature and uncovered a possible dependency of maximum deflection on moisture absorption in the hybrid composite structure. Excellent correlation was demonstrated between the PMI measurement technique and the laser displacement transducer measurements. The PMI measurements enabled the discovery of the initial geometric imperfections of the beam, and the extreme involvement of the beam fixture boundary conditions on this imperfection. This validates the accuracy of the PMI measurement technique for this application, and gives the valuable understanding of the full-field displacement of the structure during testing.

The SMAHC beam specimen's dynamic response was investigated with a generated thermal load by resistive heating, and application of a 10-400 Hz random base excitation. The dynamic measurements were post-processed into FRF's, PSD's, RMS values, and coherence functions. The post-processing of the experimental results not only demonstrated the adaptive stiffening mechanism of the SMAHC beams, but also enabled the modal parameter estimation of damping, and modal frequency of each mode. The displacement RMS values were shown to decrease with temperature. The modal damping estimates decreased once the Nitinol ribbon was above A_s temperature, until higher temperatures near 121.1 °C (250 °F) were reached, where a slight increase in damping estimates occurred most likely due to the softening of the heated glass epoxy material.

The precise experimental measurements were used as input into the commercial finite element code ABAQUS to accurately predict the static and dynamic responses of the SMAHC beam specimens. In the static thermoelastic response comparisons of numerical prediction and experimental results, ABAQUS showed excellent qualitative agreement with experiment for multiple runs. It was discovered that there is most likely a temperature correlation error in the Nitinol recovery force measurements of 10 - 20 °F. When this error is accounted for in the CTE material property input values excellent agreement with the experimental results is

demonstrated. This indicates that it is critical that the appropriate material characterization measurements are accurately measured for the state that the embedded SMA material is in.

The numerical prediction of the dynamic response of the SMAHC beams proved to be in excellent agreement with experimental measurements after the application of boundary springs, and shifting of the CTE material property values. The displacement PSD's comparison showed agreement for all positions 1, 2, and 3 along the length of the beam for both beam specimens. The results were achieved by a linear random analysis in ABAQUS using accurately measured modal parameters, material property data, thermal loads, and random base excitation as input into the model. An additional investigation into the dynamic behavior of the beam at temperatures corresponding to the buckling phenomena (80 °F – 140 °F) showed the limitations of the numerical model using a linear random analysis to capture the complex dynamic behavior which occurs through this temperature range.

The motivation for the static and dynamic response investigation of SMAHC beams is to demonstrate the decrease in the dynamic response amplitude when under random excitations. Random excitation of a structure can lead to sonic fatigue and undesirable noise transmission characteristics of a structure. By demonstrating a reduction in the response, and the adaptive stiffening mechanism introduced by the SMA actuators, the implications of vibration and noise transmission reduction are evident. It is possible that finding an optimal lay-up or embedding position of the SMA actuators to demonstrate most efficient control over the structure could result in increased performance of the SMAHC structure. Also, the fabrication of other SMAHC structures such as a panel specimen was previously done at NASA LaRC, although experimental validation wasn't completed. Numerical studies have shown that a weight-efficient SMAHC panel demonstrates superior dynamic response and sonic fatigue behavior over other conventionally noise-treated panels. Also, the SMAHC panel numerically shows superior transmission loss (TL) characteristics in the low frequency, stiffness-controlled region. The weight-efficient stiffening effect has significant implications for dynamic response and sonic fatigue reduction. For further research, the fabrication of another SMAHC panel could be done, in which an extensive experimental investigation could be performed measuring the vibration response, acoustic radiation, and transmission loss characteristics using the more thorough measuring techniques used in this study. The acoustic radiation and transmission loss experimental investigation could produce a multitude of additional discoveries. With the addition of increased commercial code capabilities the numerical simulation study could also be investigated to compare.

In conclusion, this study uses fundamental engineering property measurement to accurately model SMAHC beam specimens. The experimental investigation of the static and dynamic response of the SMAHC structures was performed using accurate measuring techniques, which uncovered interesting and complex behavior of the SMAHC beam specimens. The SMA actuators demonstrated an adaptive stiffening effect to the structure, which was successfully, modeled in the commercial finite element code ABAQUS.

Chapter 7

REFERENCES

1. L.C. Chang and T.A. Read, *Trans. AIME*, 89 (1951) 47.
2. W.J. Buehler, J.W. Gilfrich and R.C. Wiley, *J. Appl. Phys.*, 34 (1963) 1475.
3. T.L. Turner, "Experimental Validation of a Thermoelastic Model for SMA Hybrid Composites," *Smart Structures and Materials 2001; Modeling, Signal Processing, and Control in Smart Structures*, SPIE Vol. 4326, Paper No. 4326-24, Newport Beach, CA, 2001.
4. O. Heintze, S. Seelecke, Interactive WWW page for the simulation of shape memory alloys, <http://www.mae.ncsu/homeages/seelecke>, 2000.
5. Liang, C., Rogers, S.A., and Fuller, C.R.: "Acoustic Transmission and Radiation Analysis of Adaptive Shape Memory Alloy Reinforced Laminated Plates," *Journal of Sound and Vibration*, 145(1), 1991, pp. 23-41.
6. Funakubo, H. (Editor) (Translated by J.B. Kennedy): *Shape Memory Alloys*, Gordon and Breach Science Publishers, New York, NY, 1987.
7. Cross, W.B., Kariotis, A.H., and Stimler, F.J.: "Nitinol Characterization Study," NASA CR-1433, 1969.
8. T.L. Turner, "Fabrication and Characterization of SMA Hybrid Composites," *Smart Structures and Materials 2001; Active Materials: Behavior and Mechanics*, SPIE vol. 4333, Paper No. 4333-60, Newport Beach, CA, 2001.
9. Otsuka, K. and Wayman, C.M. (Editors): *Shape Memory Materials*, Cambridge University Press, Cambridge, CB2 2RU, UK, 1998.
10. Buehler, W.J. and Wang, F.E.: "A Summary of Recent Research on the Nitinol Alloys and Their Potential Application in Ocean Engineering," *Journal of Applied Physics*, Vol. 34, 1963, pp. 1475-1477.
11. T. Saburi, T. Tatsumi and S. Nenno, *J. de Phys.*, **43** (1982) C4-261.
12. S. Miyazaki, Y. Ohmi, K. Otsuka and Y. Suzuki, *J. de Phys.*, **43** (1982) C4-255.
13. M. Kapgan and K.N. Melton, in *Engineering Aspects of Shape Memory Alloys*, ed. T.W. Duerig, K. N. Melton, D. Stockel and C..M. Wayman, Butterworth-Heinemann (1990) pp.137-148.
14. Janocha, Hartmut (Editor): *Adaptronics and Smart Structures: basics, materials, design, and applications*, Springer-Verlag Berlin Heidelberg, Germany, 1999.
15. T.L. Turner, "Structural acoustic response of a shape memory alloy hybrid composite panel (lessons learned)," *Smart Structures and Materials 2001; Smart Structures and Integrated Systems*, SPIE Vol 4701, Paper No. 4701-60, San Diego, CA, 17-21 March 2002.
16. C.A. Rogers, and H.H. Robertshaw, "Shape Memory Alloy Reinforced Composites," *Engineering Science Preprints* 25, Society of Engineering Science, Inc., ESP25.8027, 1988.
17. T.L. Turner, "SMA Hybrid Composites for Dynamic Response Abatement Applications," *7th International Conference on Recent Advances in Structural Dynamics*, 1, 453-465, ISVR, University of Southampton, Southampton, UK, 2000.
18. T.L. Turner, "Thermomechanical Response of Shape Memory Alloy Hybrid Composites," NASA/TM-2001-210656, 2001.
19. Baz A, Poh S, Ro J and Gilheany J 1995 "Control of natural frequencies of NITINOL-reinforced composite beams," *J. Sound Vib.* **185** 171-85.
20. Ostachowicz W, Krawczuk M and Zak A 1999 "Natural frequencies of a multiplayer composite plate with shape memory alloy wires," *Finite Elem. Anal. Des.* **32** 71-83.
21. Choi S, Lee JJ, Seo D C and Choi S W 1999 "The active buckling control of laminated composite beams with embedded shape memory alloy wires," *Compos. Struct.* **47** 679-86.

22. Thompson S P and Loughlan J 2000 “The control of the post-buckling response in thin composite plates using smart technology ,” *Thin-walled Struct.* **36** 231-63.
23. Ostachowicz W, Krawczuk M and Zak A 2000 “Dynamics and buckling of a multiplayer composite plate with embedded SMA wires,” *Compos. Struct.* **48** 163-7.
24. Tawfik M, Ro J J and Mei C 2002 “Thermal post-buckling and aeroelastic behaviour of shape memory alloy reinforced plates,” *Smart Mater. Struct.* **11** 297-303.
25. Chaudhry, Z. and Rogers, C. A.: “Bending and Shape Control of Beams Using SMA actuators,” *Journal of Intelligent Systems and Structures*, Vol. 2, 1991, pp.581-602.
26. Turner, T.L., Zhong, Z. W., and Mei, C.: “Finite Element Analysis of the Random Response Suppression of Composite Panels at Elevated Temperatures Using Shape Memory Alloy Fibers,” AIAA-94-1324-CP, *Proc. of the 35th AIAA/ASME/ASCE/AHS/ASC Structures, Structural Dynamics and Materials Conf.*, Hilton Head, SC, April 18-21, 1994, pp. 136-146.
27. Birman, V.: “Stability of Functionally Graded Shape Memory Alloy Sandwich Panels,” *Smart Materials and Structures*, **6**, 1997, pp. 278-286.
28. Tanaka, K. and Nagaki, S.: “A Thermomechanical Description of Materials with Internal Variables in the Process of Phase Transformation,” *Ingenieur-Archiv*, 51, 1982, pp. 287-299.
29. Liang, C. and Rogers, C.A.: “One-Dimensional Thermomechanical Constitutive Relations for Shape Memory Materials,” *Journal of Intelligent Material Systems and Structures*, Vol. 1, April, 1990, pp. 207-235.
30. Brinson, L. C.: “One-Dimensional Constitutive Behavior of Shape Memory Alloys: Thermomechanical Derivation with Non-Constant Material Functions,” *Journal of Intelligent Material Systems and Structures*, 4(2), 1993, pp. 229-242.
31. Boyd, J. G. and Lagoudas, D. C.: “A Thermodynamical Constitutive Model for Shape memory Materials –Part I: The Monolithic Shape Memory Alloy,” *Int. J. of Plasticity*, **12**(7), 1996, pp. 805-842.
32. Turner, T.L. “A New Thermoelastic Model for Analysis of Shape Memory Alloy Hybrid Composites,” *Journal of Intelligent Material Systems and Structures*, Vol.11, May 2000.
33. G.A. Fleming, H.L. Soto, and B. W. South, “Projection Moire’ Interferometry for Rotorcraft Applications: Deformation Measurements of Active Twist Rotor Blades”, *American Helicopter Society 58th Annual Forum*, Montreal, Canada, June 10-13, 2002.
34. G.A. Fleming, S. M. Bartram, M.R. Waszak, and L.N. Jenkins, “Projection Moire’ Interferometry Measurements of Micro Air Vehicle Wings”, *Proc. SPIE Vol. 4448*, pp. 90 –101, (2001).
35. G.A. Fleming, H.L. Soto, B. W. South, and S. M. Bartram, “Advances in Projection Moire’ Interferometry Development for Large Wind Tunnel Applications”, *SAE Paper No. 1999-01-5598, SAE World Aviation Congress*, San Francisco, CA, October 19-21, 1999.
36. D. Phillips, “Image Processing in C, Part 14: Warping and Morphing”, *C/C++ Users Journal*, pp. 55-68, October, 1995.
37. L. Pirrodda, “Shadow and projection moire’ techniques for absolute or relative mapping of surface shapes”, *Optical Engineering* 21(4), pp. 640-649, July/August (1982).
38. Jones, R. M.: *Mechanics of Composite Materials*, 2nd Edition, Hemisphere Publishing Corporation, New York, NY, 1999.
39. Shames, I. H.; and Dym, C.L: *Energy and Finite Element Methods in Structural Mechanics*, Hemisphere Publishing Corporation, New York, NY, 1985.
40. Whitney, J. M.: *Structural Analysis of Laminated Anisotropic Plates*, Technomic Publishing Company, Inc., Lancaster, Pennsylvania, 1987.
41. T. L. Turner, and H. Patel, “Analysis of SMA hybrid composite structures using commercial codes,” *Smart Structures and Materials: Modeling, Signal Processing, and Control*, SPIE Vol 5383, Paper No. 5383-12, San Diego, CA, 14-18 March 2004.
42. Inman, Daniel J.: *Engineering Vibration*, Prentice-Hall Inc., Upper Saddle River, New Jersey, 2001.

Chapter 8

TABLES

Table 3.1- Beam 2 Run 1 dynamic response RMS displacement values as a function of temperature for positions 1, 2, and 3 along the length of the beam.

	Pos1	Pos2	Pos3
Temp	RMS	RMS	RMS
°F	Displ., in	Disp, in	Displ., in
73	.838e-2	1.30e-2	.645e-2
150	.656e-2	.985e-2	.586e-2
160	.523e-2	.757e-2	.477e-2
170	.441e-2	.627e-2	.404e-2
180	.473e-2	.607e-2	.435e-2
190	.343e-2	.482e-2	.317e-2
200	.320e-2	.701e-2	.297e-2
210	.297e-2	.415e-2	.275e-2
220	.267e-2	.373e-2	.247e-2
230	.260e-2	.364e-2	.241e-2
240	.254e-2	.355e-2	.235e-2
250	.254e-2	.356e-2	.235e-2

Table 3.2- Beam 3 Run 2 dynamic response RMS displacement values as a function of temperature for positions 1, 2, and 3 along the length of the beam.

	Pos1	Pos2	Pos3
Temp	RMS	RMS	RMS
°F	Displ., in	Disp, in	Displ., in
73	.941e-2	1.69e-2	.812e-2
150	.652e-2	1.03e-2	.669e-2
160	.376e-2	.573e-2	.336e-2
170	.366e-2	.551e-2	.389e-2
180	.394e-2	.587e-2	.427e-2
190	.343e-2	.508e-2	.381e-2
200	.331e-2	.489e-2	.347e-2
210	.294e-2	.434e-2	.278e-2
220	.263e-2	.388e-2	.259e-2
230	.251e-2	.370e-2	.223e-2
240	.243e-2	.358e-2	.228e-2
250	.239e-2	.352e-2	.218e-2

Table 3.3- Beam 2 dynamic response modal parameter estimates for runs 1, 2, and 3.

Temp, °F	Run1				Run2				Run3			
	f ₁ , Hz	ζ ₁ , %	f ₃ , Hz	ζ ₃ , %	f ₁ , Hz	ζ ₁ , %	f ₃ , Hz	ζ ₃ , %	f ₁ , Hz	ζ ₁ , %	f ₃ , Hz	ζ ₃ , %
73	30.1	1.06	160.2	.66	30.9	.81	163.3	.68	30.5	.87	162.1	.73
150	59.6	.31	223.2	.66	67.1	.17	240.0	.39	66.1	.22	237.8	.43
160	80.0	.17	271.9	.26	81.7	.17	276.1	.25	81.9	.20	276.7	.29
170	91.3	.14	302.0	.27	92.3	.15	304.5	.26	92.9	.14	306.4	.29
180	99.5	.15	323.7	.19	100.8	.13	327.3	.18	101.5	.13	329.1	.18
190	106.9	.13	343.9	.15	107.5	.15	345.5	.16	108.1	.13	347.1	.14
200	112.9	.16	360.2	.17	113.1	.16	360.7	.16	112.6	.17	359.6	.14
210	117.2	.18	371.9	.18	116.9	.16	371.2	.16	116.1	.16	369	.15
220	120.3	.20	380.9	.27	119.5	.17	378.5	.20	118.4	.17	375.4	.17
230	122.5	.21	387.4	.24	121.1	.18	383.1	.27	120.0	.18	379.9	.25
240	124.1	.21	391.6	.19	122.0	.18	385.8	.23	121.1	.19	383.1	.27
250	125.1	.21	394.2	.18	122.8	.21	388	.22	121.2	.19	384.7	.25

Table 3.4- Beam 3 dynamic response modal parameter estimates for runs 1, 2, and 3.

Temp, °F	Run1				Run2				Run3			
	f ₁ , Hz	ζ ₁ , %	f ₃ , Hz	ζ ₃ , %	f ₁ , Hz	ζ ₁ , %	f ₃ , Hz	ζ ₃ , %	f ₁ , Hz	ζ ₁ , %	f ₃ , Hz	ζ ₃ , %
73	30.3	.72	162.6	.56	29.9	.81	161.9	.59	31.5	.76	163.9	.66
150	60.5	.24	222.4	.68	62.8	.24	225.2	.97	67.3	.21	237.9	.84
160	79.8	.29	269.4	.21	80.7	.29	272.3	.40	82.7	.33	276.5	.42
170	91.3	.12	298.9	.34	92.5	.20	301.9	.35	93.5	.21	304.1	.42
180	100.5	.10	324.5	.42	101.3	.15	324.6	.58	101.9	.14	326.7	.75
190	107.1	.09	342.5	.18	108.2	.14	346.4	1.13	108.3	.14	346.2	1.18
200	112.1	.11	356.3	.14	113.7	.16	362.4	.38	113.0	.15	360	.52
210	116.5	.15	368.5	.12	117.8	.16	372.2	.29	116.8	.18	369.8	.34
220	119.1	.18	375.6	.12	120.3	.20	378.7	.44	119.4	.23	375.9	.35
230	121.1	.21	381.2	.12	122.2	.21	383.8	.86	121	.23	380	.74
240	122.5	.24	384.6	.17	123.3	.22	388	1.10	121.8	.22	383.1	1.12
250	123.9	.25	388.8	.28	123.8	.20	389.9	1.31	122.3	.21	384.9	.78

Table 4.1– Thermomechanical material property measurement of the Fiberite E-glass/934 epoxy material system in principal material direction.

Temperature	E ₁	E ₂	ν_{12}	G ₂₁	α_1	α_2
°C	GPa	GPa	—	GPa	$\mu\epsilon/^\circ\text{C}$	$\mu\epsilon/^\circ\text{C}$
21.1	49.30	20.00	0.29	9.65	5.22	10.80
26.7	49.30	19.86	0.29	9.58	5.83	13.81
37.8	49.16	19.44	0.29	9.24	6.95	21.02
48.9	49.02	18.96	0.29	8.89	7.22	24.14
60.0	48.82	18.48	0.29	8.55	7.00	24.66
65.6	48.75	18.20	0.29	8.41	6.80	24.28
71.1	48.75	17.79	0.29	8.27	6.62	23.90
82.2	48.68	17.03	0.29	7.93	6.34	22.79
93.3	48.61	16.20	0.29	7.58	6.25	22.00
104.4	48.61	15.31	0.29	6.76	6.39	21.92
115.6	48.54	14.41	0.29	6.00	6.77	22.66
121.1	48.54	14.00	0.29	5.58	6.97	23.33
126.7	48.61	13.45	0.29	5.17	7.18	24.01
137.8	48.68	12.41	0.29	4.27	7.42	25.47
148.9	48.82	11.38	0.29	3.45	7.63	26.28

Table 4.2– Thermomechanical material property measurements of the Nitinol Ribbon actuator material.

Temperature	Recovery Stress			E	α_2
	Cycle 2	Cycle 3	Cycle 4		
°C	MPa	MPa	MPa	GPa	$\mu\epsilon/^\circ\text{C}$
21.1	0	0	0	27.17	6.606
26.7	2.130	1.276	2.130	24.82	6.606
32.2	7.233	5.530	7.233	22.41	6.606
37.8	16.18	13.20	14.05	20.06	6.606
43.3	31.92	28.95	28.52	25.72	6.606
48.9	70.65	70.23	78.74	31.37	7.236
54.4	135.4	137.9	151.9	36.96	7.866
60.0	192.0	199.6	217.9	42.61	8.496
65.6	240.5	256.6	269.4	48.27	9.108
71.1	297.1	301.8	309.8	54.88	9.738
76.7	341.8	341.8	341.3	61.43	10.37
82.2	374.5	373.7	372.0	64.19	11.00
87.8	402.2	399.2	399.2	63.16	11.00
93.3	425.6	419.2	418.8	62.06	11.00
98.9	449.9	438.8	437.5	63.92	11.00
104.4	469.0	451.6	448.2	65.78	11.00
110.0	481.0	464.8	458.8	67.64	11.00
115.6	491.6	475.8	467.3	69.50	11.00
121.1	500.1	485.6	472.9	71.36	11.00
126.7	508.6	490.3	478.8	70.81	11.00
132.2	515.0	496.7	481.8	70.33	11.00
137.8	520.5	500.5	485.2	69.78	11.00
143.3	523.5	502.2	487.3	69.29	11.00
148.9	527.8	503.9	490.7	68.74	11.00

Table 4.3- Nitinol Ribbon Transformation Temperatures measured by DSC.

Transformation Marker	Temperature	
	°C	°F
Austenite Start	45	113
Austenite Finish	60	140
Martensite Start	17	62.6
Martensite Finish	0	32

FIGURES

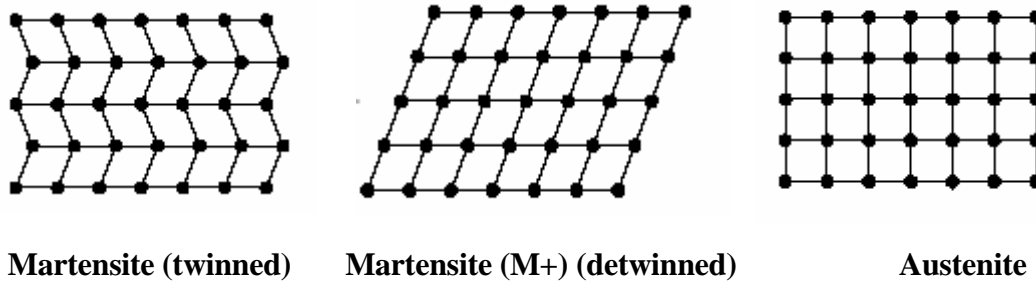


Figure 1.1- SMA Lattice Structure at different phases.

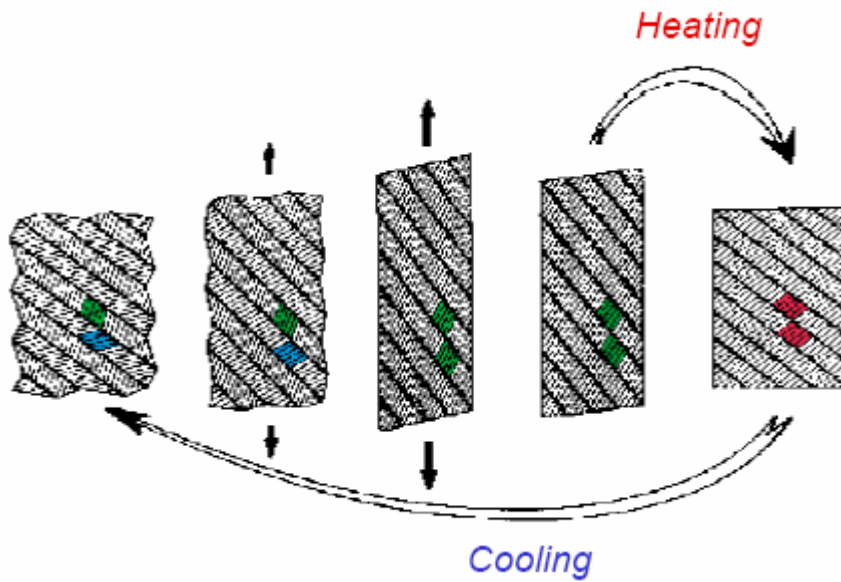


Figure 1.2– SMA body under tensile loading/unloading at low temperature, exhibiting the shape memory effect upon heating⁴.

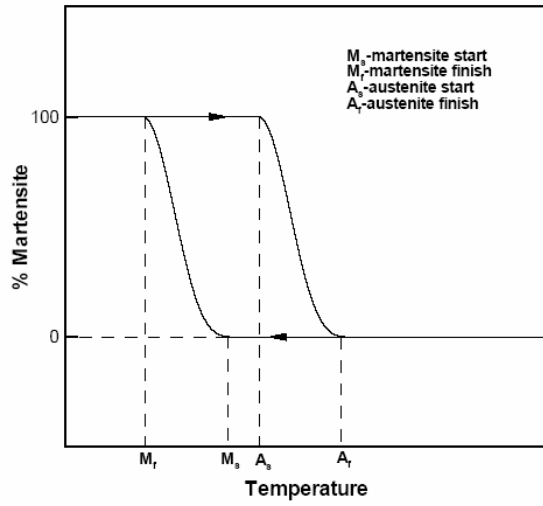


Figure 1.3– Schematic of martensitic and reverse transformations⁵.

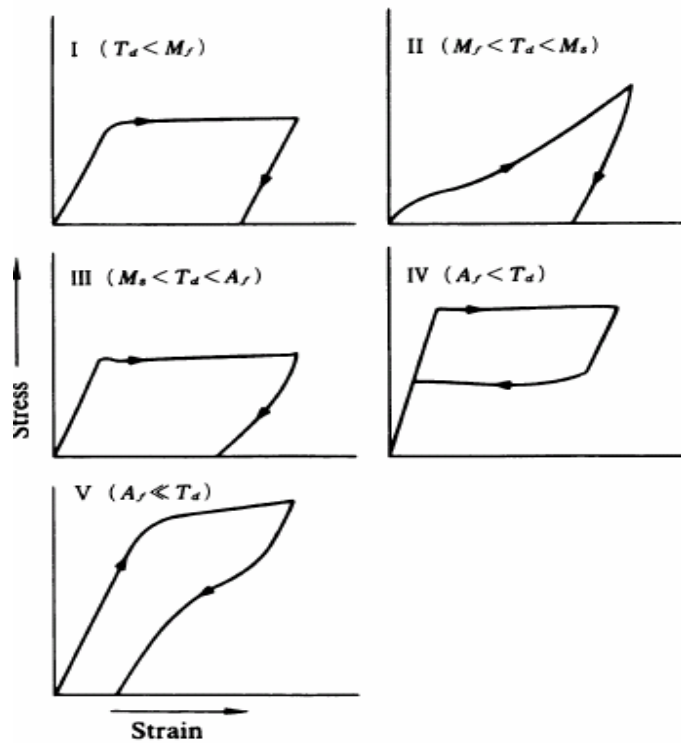


Figure 1.4– Stress-Strain Curves for Shape Memory Alloys at various intermediate temperatures⁶.

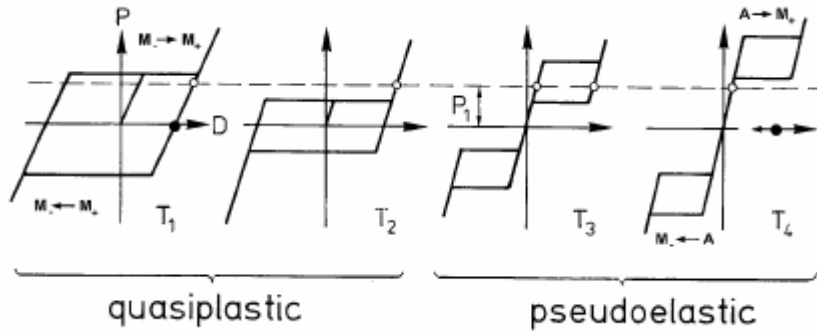


Figure 1.5- Load-Deformation diagrams for shape memory alloy at various temperatures (fully martensitic-quasiplastic) and (fully austenitic-pseudoelastic)⁴.

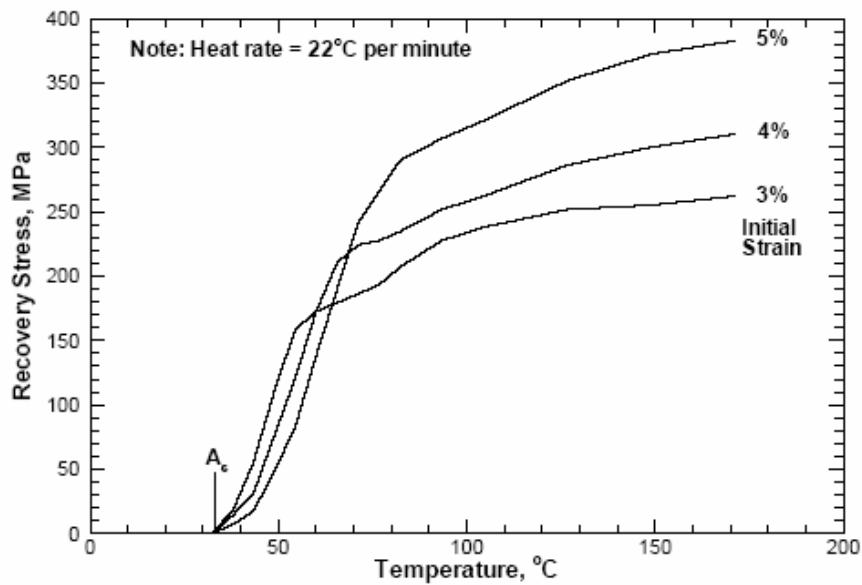


Figure 1.6– Nitinol recovery stress vs. temperature and initial strain⁷.

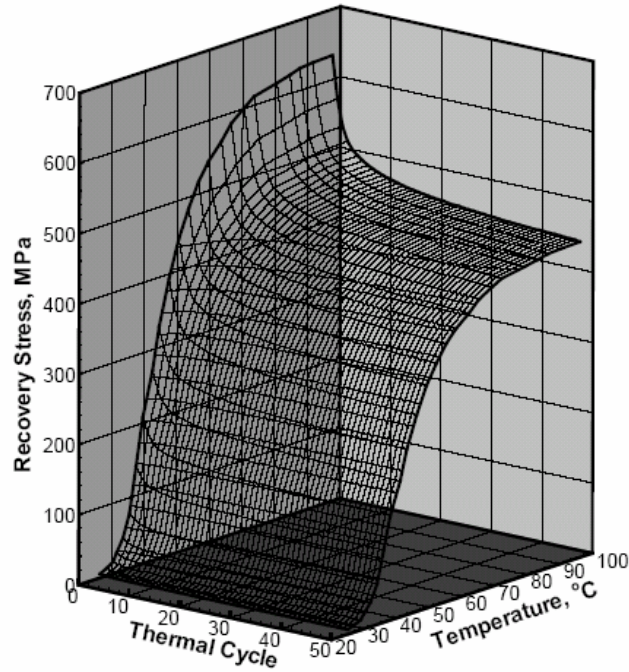


Figure 1.7– Recovery stress vs. temperature, thermal cycle for nitinol ribbon samples at 4% pre-strain⁸.

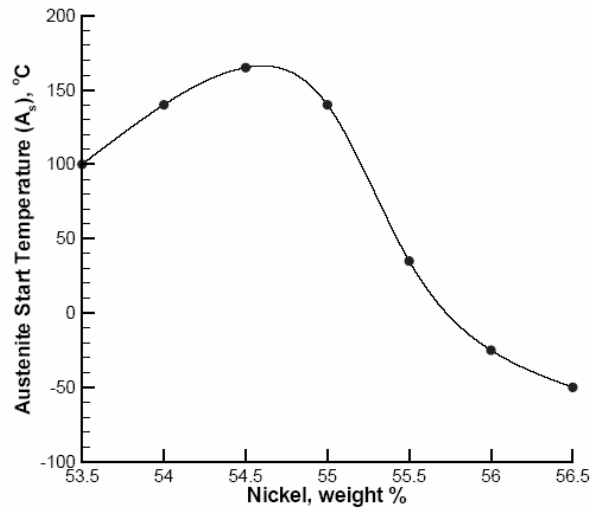


Figure 1.8– Variation of austenite start temperature with weight content (%) of Nickel in Nitinol Alloy¹⁰.

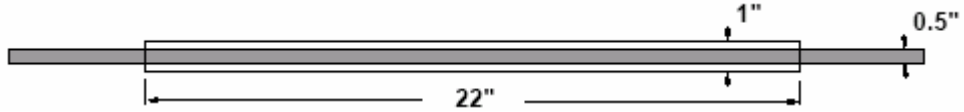


Figure 2.1- 22"x1"x0.080" Glass Epoxy/SMA Hybrid Beam (45/0/-45/90)_{2s} Lamination with SMA embedded in the 0° lamina only⁸.

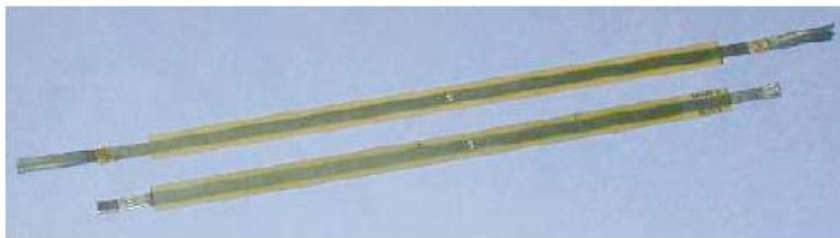
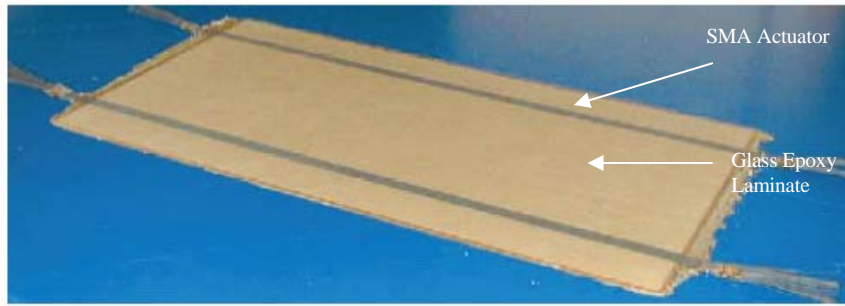


Figure 2.2- Consolidated SMAHC structure after curing cycle, and machined SMAHC beam specimens used for experiments⁸.

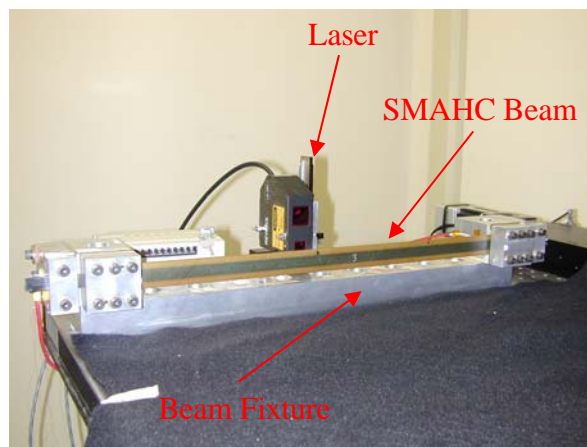


Figure 2.3– Static Experimental Set-up: SMAHC Beam3 installed in the beam fixture (front view)

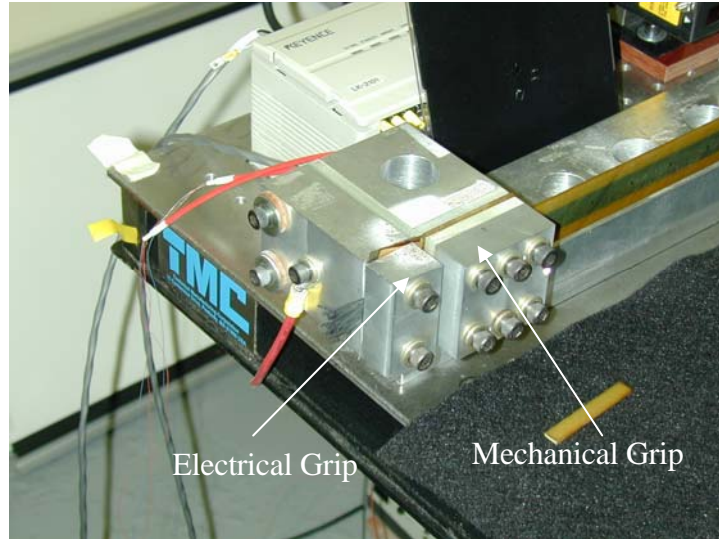


Figure 2.4a– Mechanical and electrical grip of beam fixture (front view).

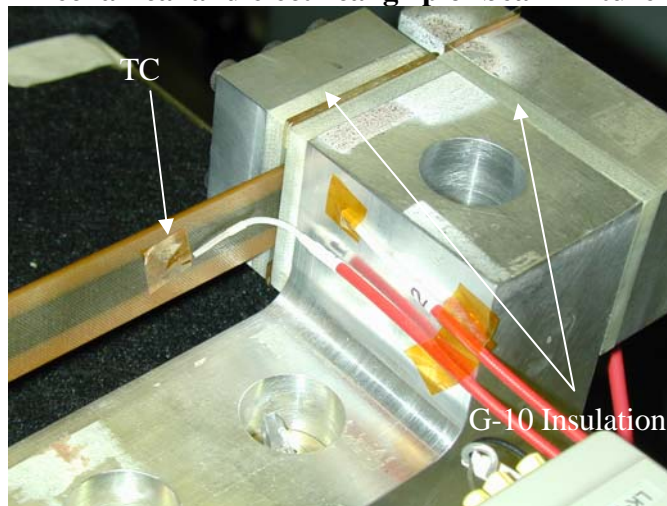


Figure 2.4b- Mechanical and electrical grip of beam fixture (back view).

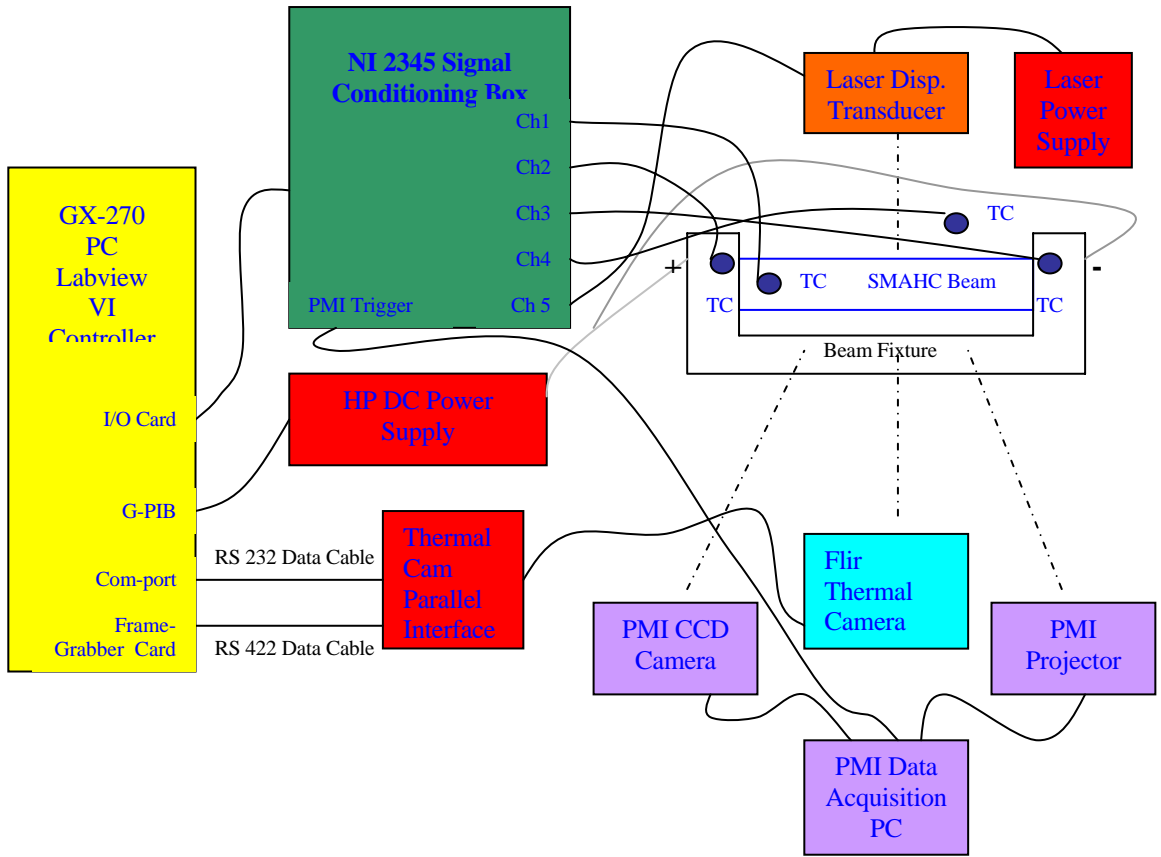


Figure 2.5- Static Thermoelastic Response Experimental Component Schematic.

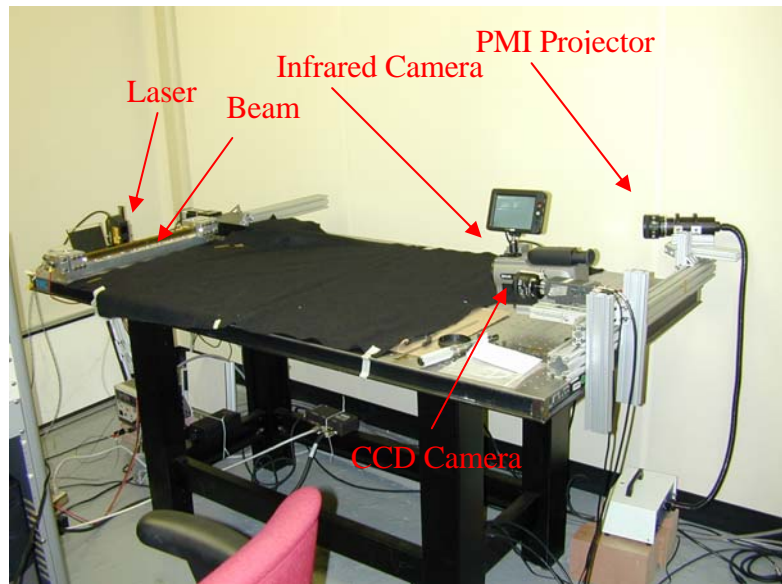


Figure 2.6– Static Thermoelastic Response Experimental Configuration Overview.

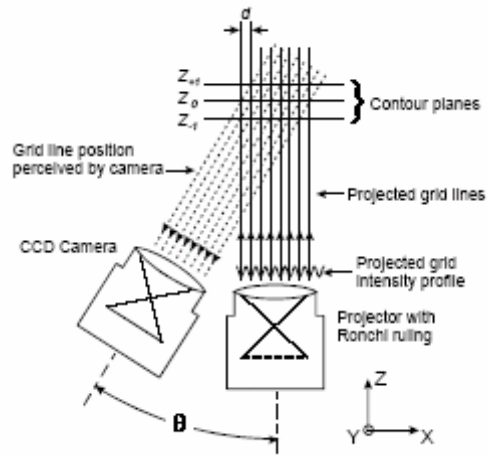


Figure 2.7- Simple PMI System Schematic³⁵.

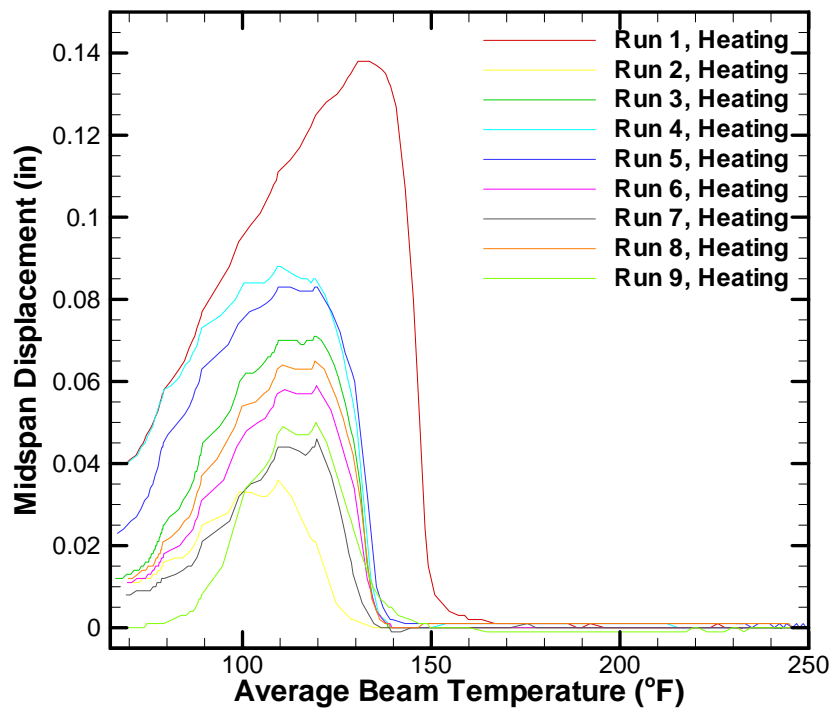


Figure 2.8– SMAHC Beam2 Laser Displacement Experimental Results of Midspan for Runs 1-9.

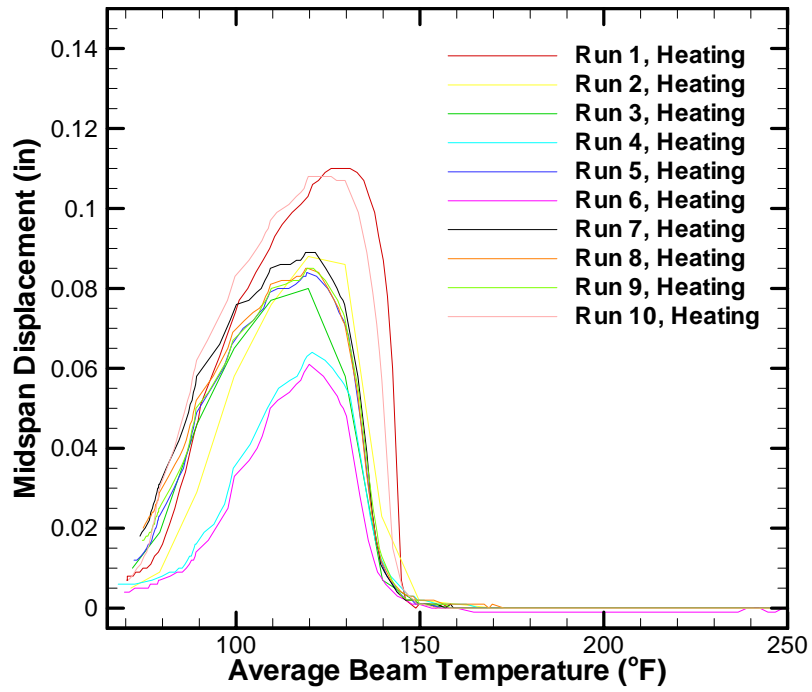


Figure 2.9– SMAHC Beam3 Laser Displacement Experimental Results for Midspan Runs 1-10.

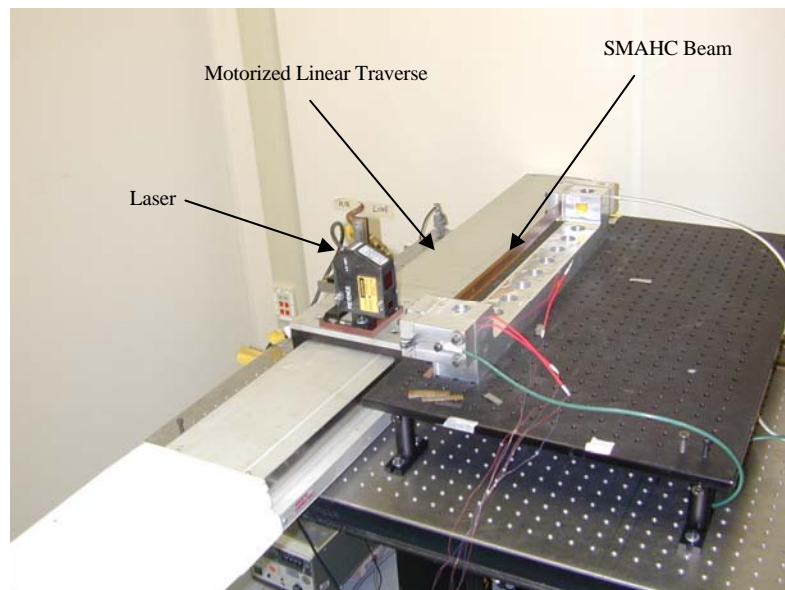


Figure 2.10– Experimental Configuration of initial imperfection measurements.

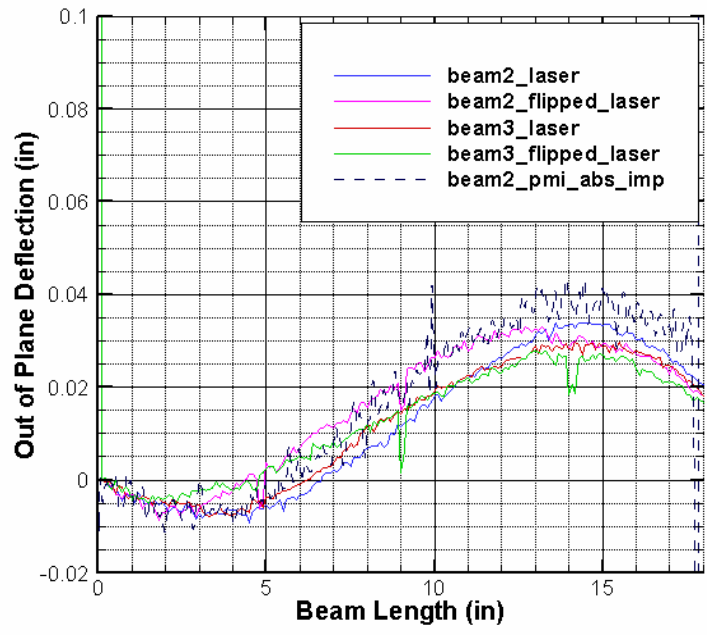


Figure 2.11- Laser Translation versus PMI initial imperfection measurements of SMAHC beams installed in beam fixture.

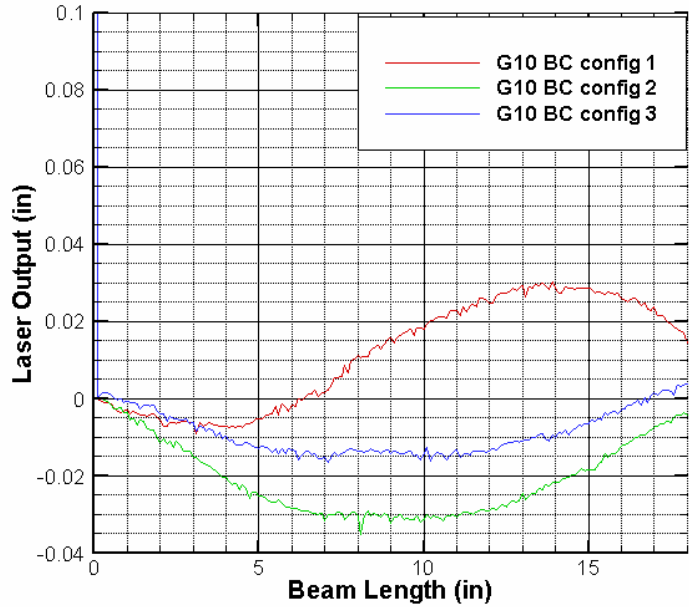


Figure 2.12- Laser Translation Measurements of SMAHC Beam3 for three different boundary condition configurations of the Garolite G-10 insulation blocks.

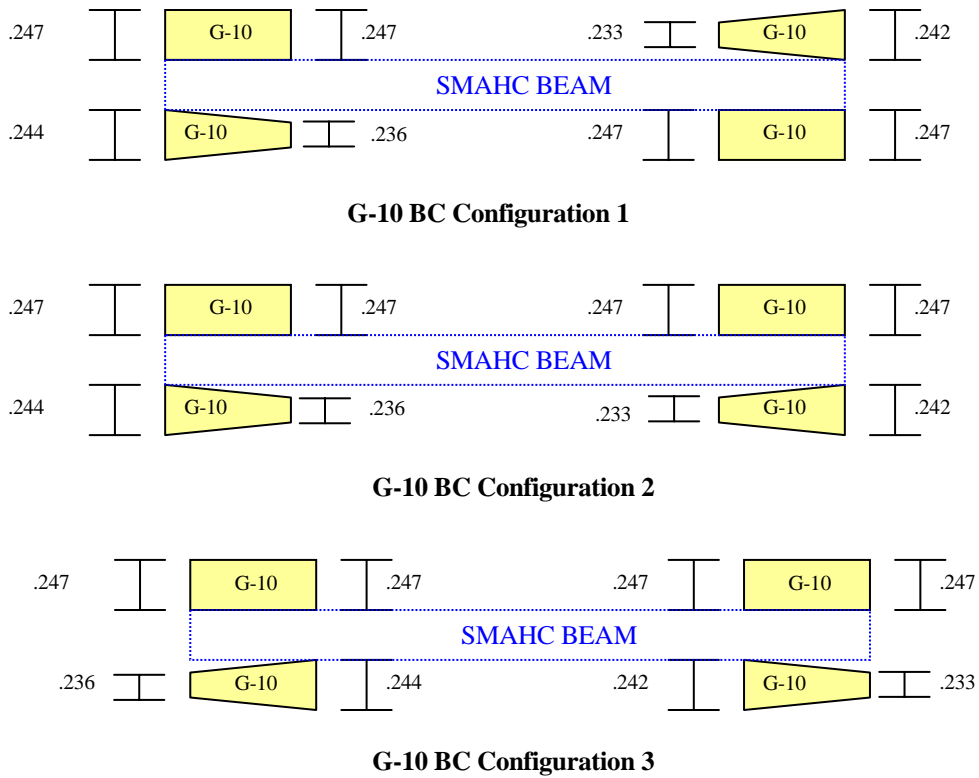


Figure 2.13- Garolite G-10 Insulation Blocks Configurations for Laser Displacement Transducer Experiments (Top view of beam fixture boundaries)

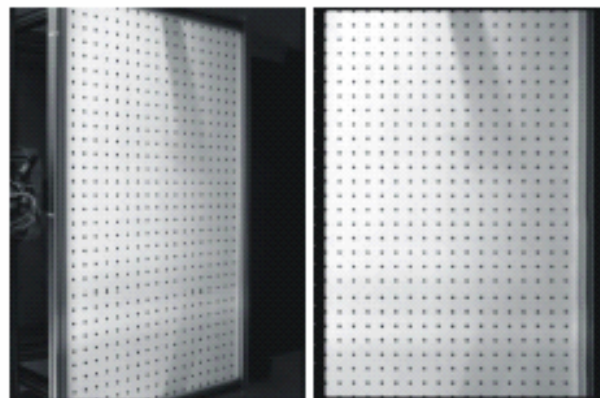


Figure 2.14- Projection Moire' Interferometry calibration plate³⁴.

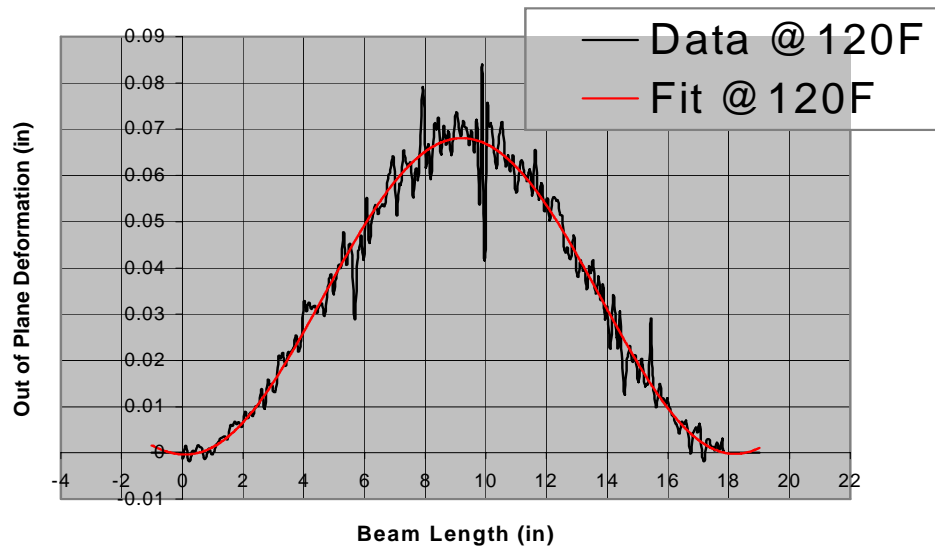


Figure 2.15- PMI differential image data and line fit for the centerline out of plane deflection for Beam3 Run3 at T=160°F.

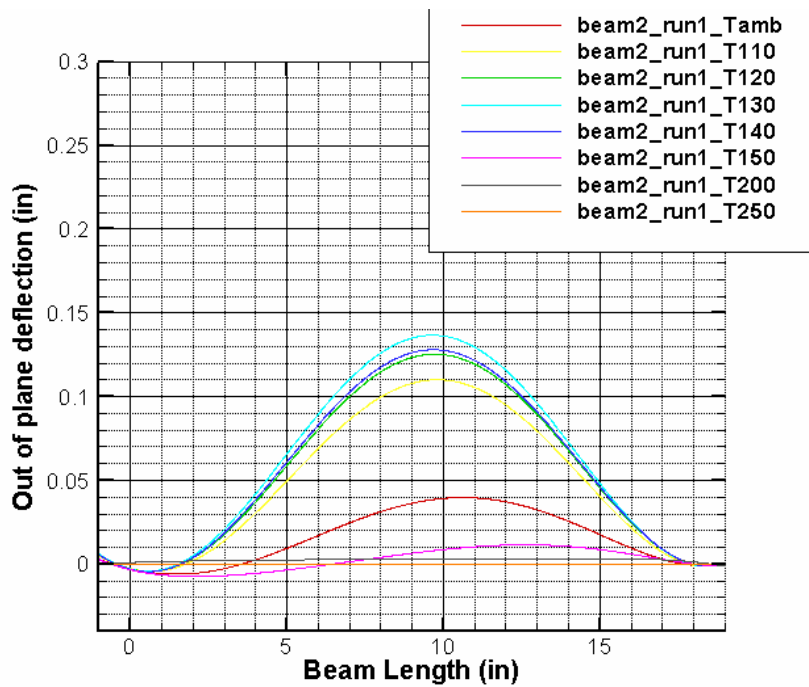


Figure 2.16- PMI full field imaging of the SMAHC Beam2 Run1

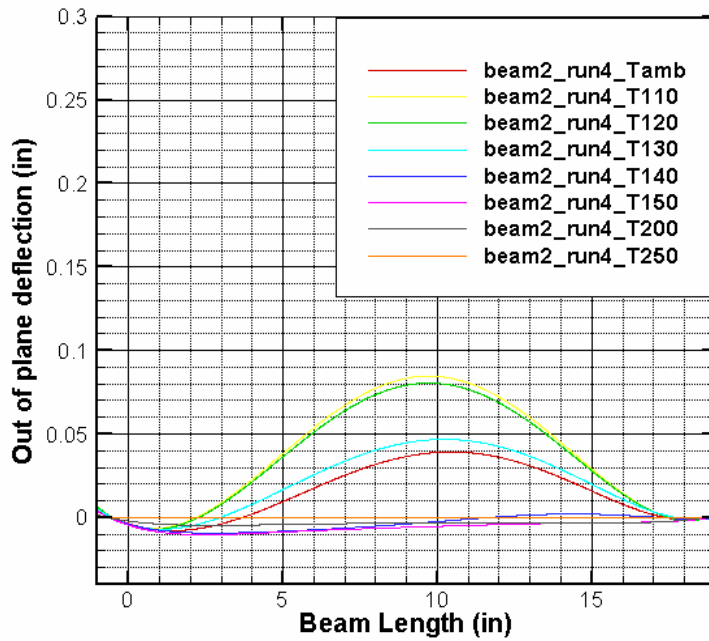


Figure 2.17- PMI full field imaging of the SMAHC Beam 2 Run 4

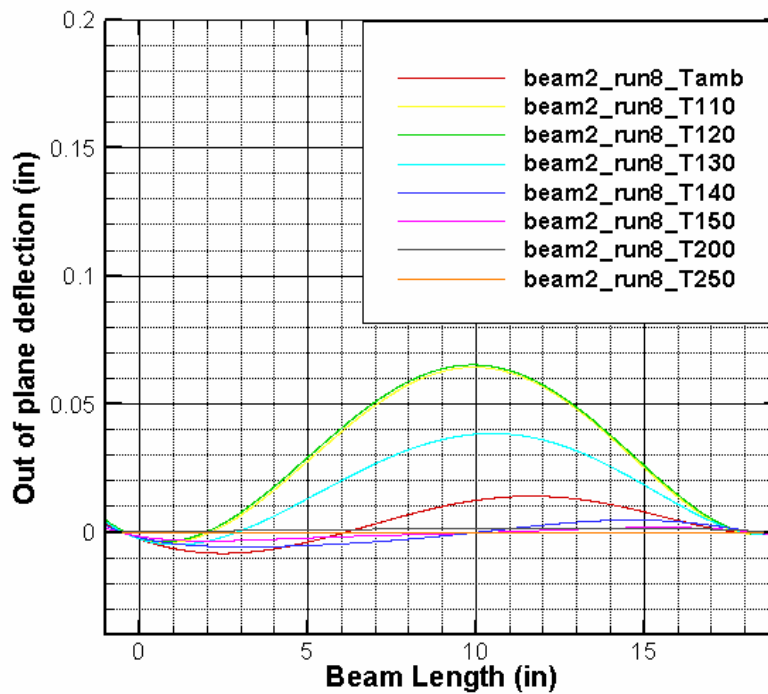


Figure 2.18- PMI full field imaging of the SMAHC Beam 2 Run 8

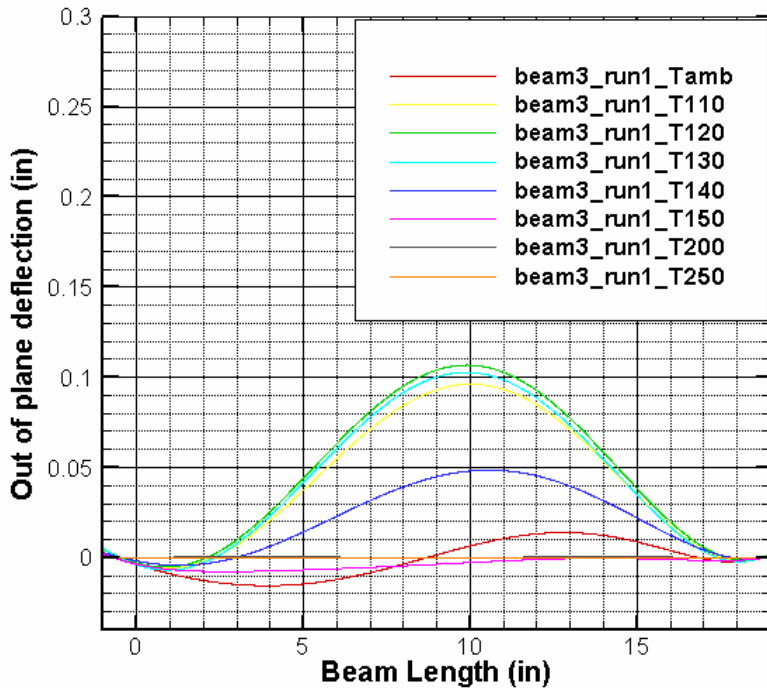


Figure 2.19- PMI full field imaging of the SMAHC Beam 3 Run 1

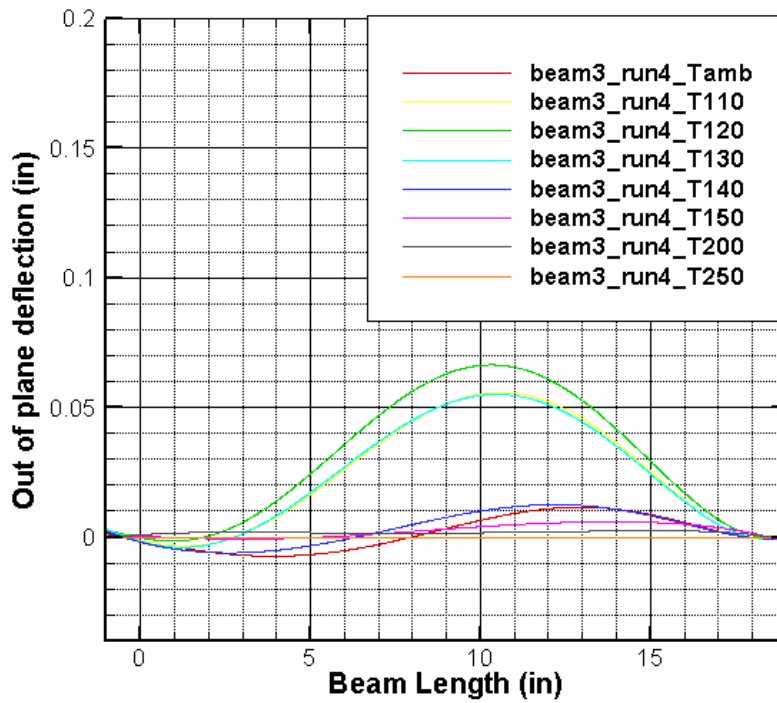


Figure 2.20- PMI full field imaging of the SMAHC Beam 3 Run 4

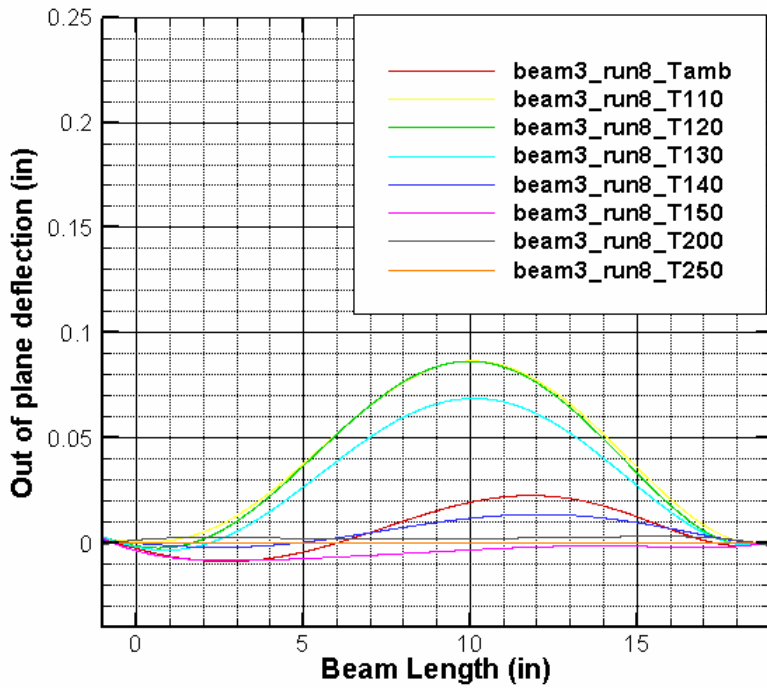


Figure 2.21- PMI full field imaging of the SMAHC Beam 3 Run 8

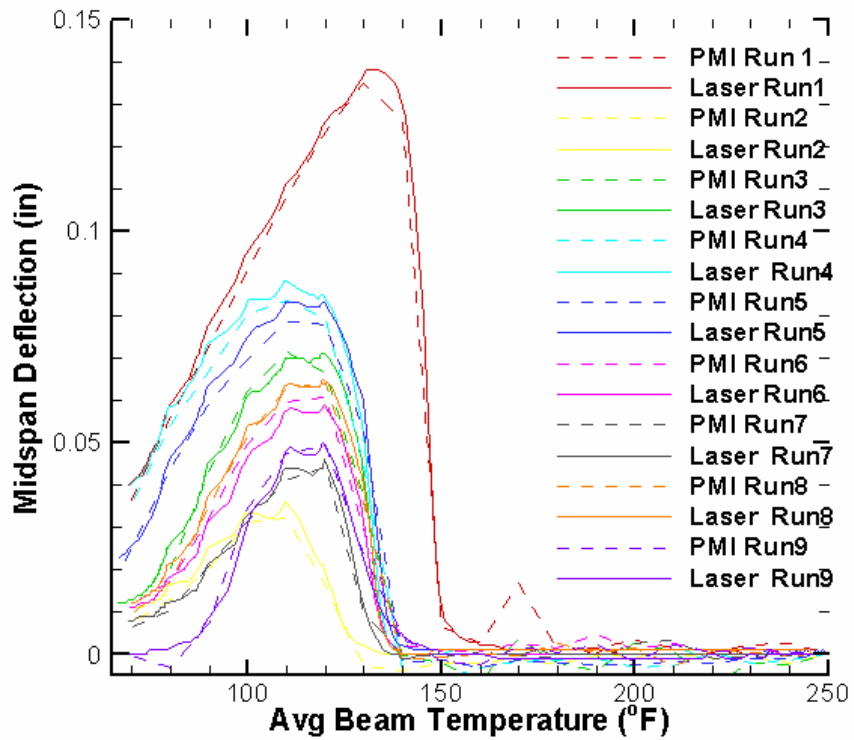


Figure 2.22- Beam2 PMI vs. Laser Static Deflection Measurements

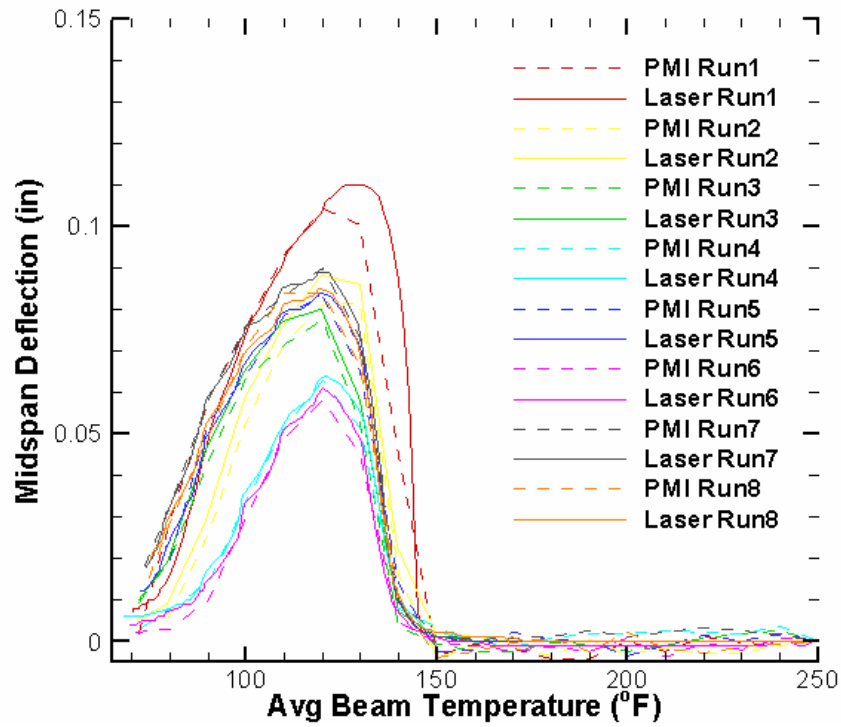


Figure 2.23- Beam3 PMI vs. Laser Static Deflection Measurements

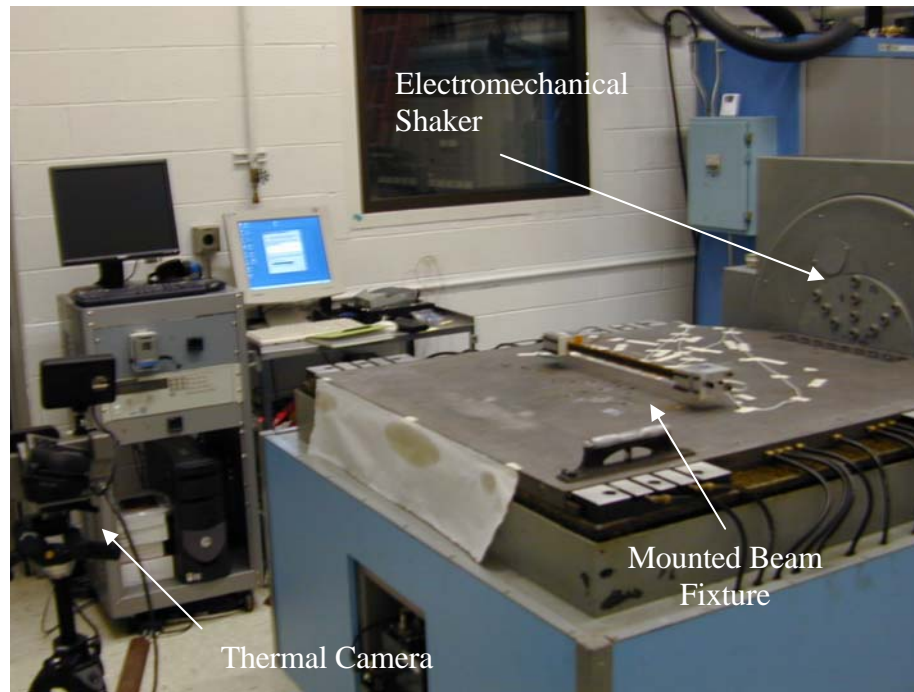


Figure 3.1- SMAHC beam dynamic response experimental configuration.

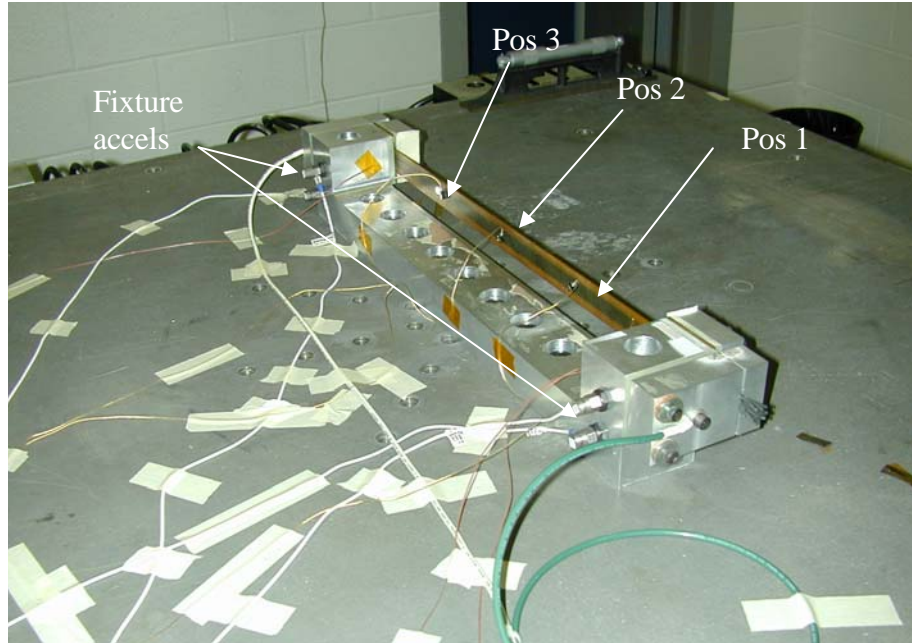


Figure 3.2– SMAHC beam specimen installed, with mounted beam response transducers and fixture transducers (back view).

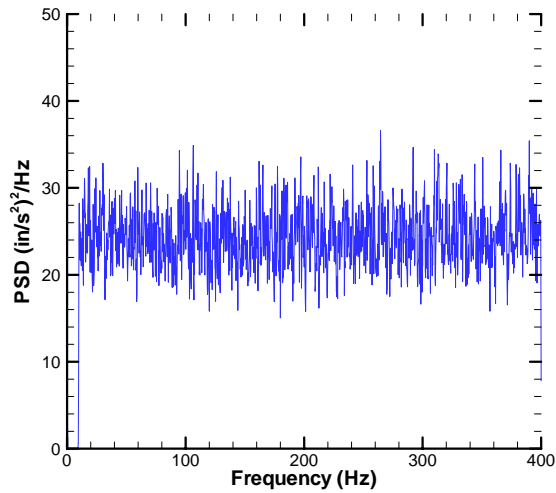


Figure 3.3– Acceleration PSD for the base excitation of the beam with a RMS value of .25g (96.5 in/s²).

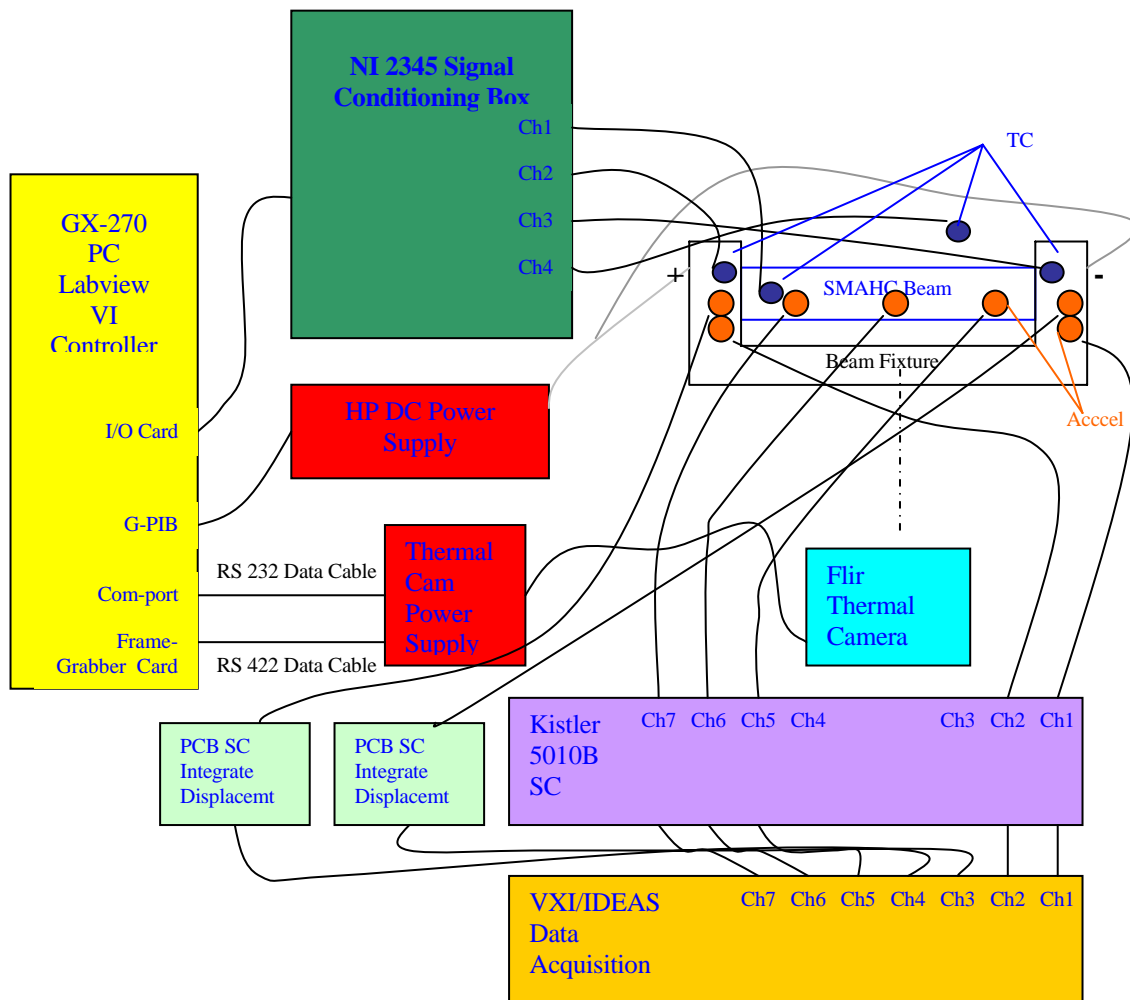


Figure 3.4- SMAHC beam dynamic response experimental component schematic.

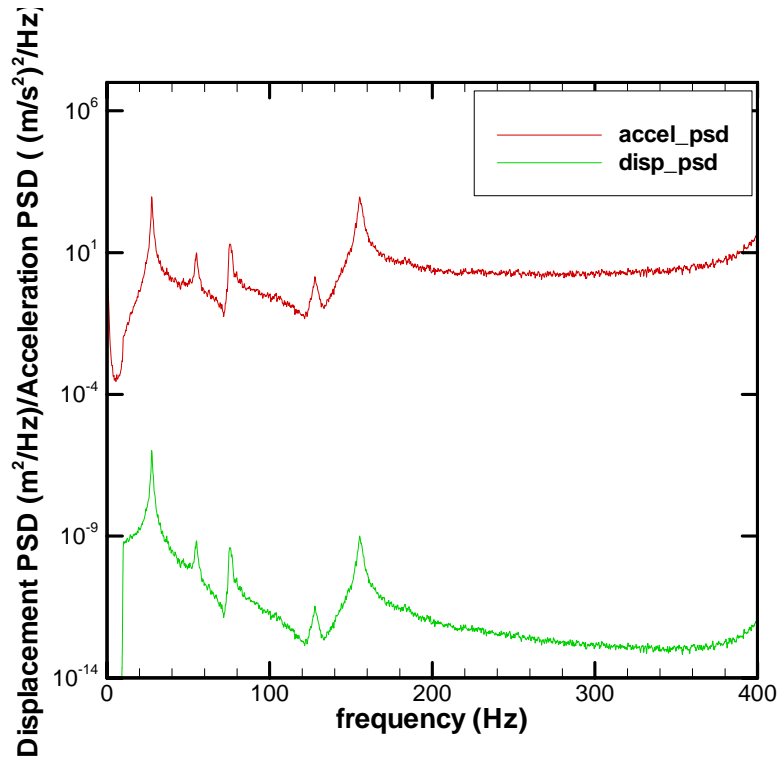


Figure 3.5- Acceleration vs. Displacement PSD generated by attached m-file, which post-processes the acceleration time history data.

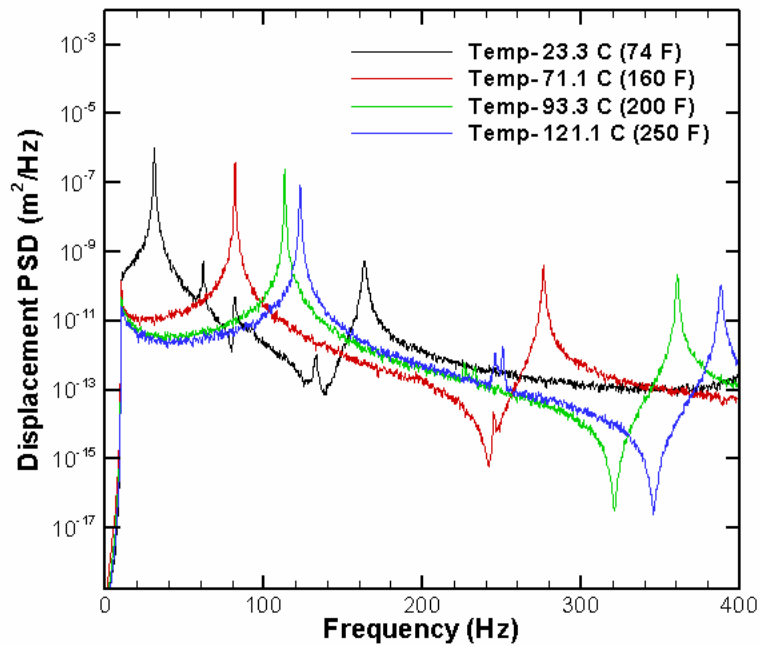


Figure 3.6- SMAHC Beam 2 PSD's for selected temperatures at position 1.

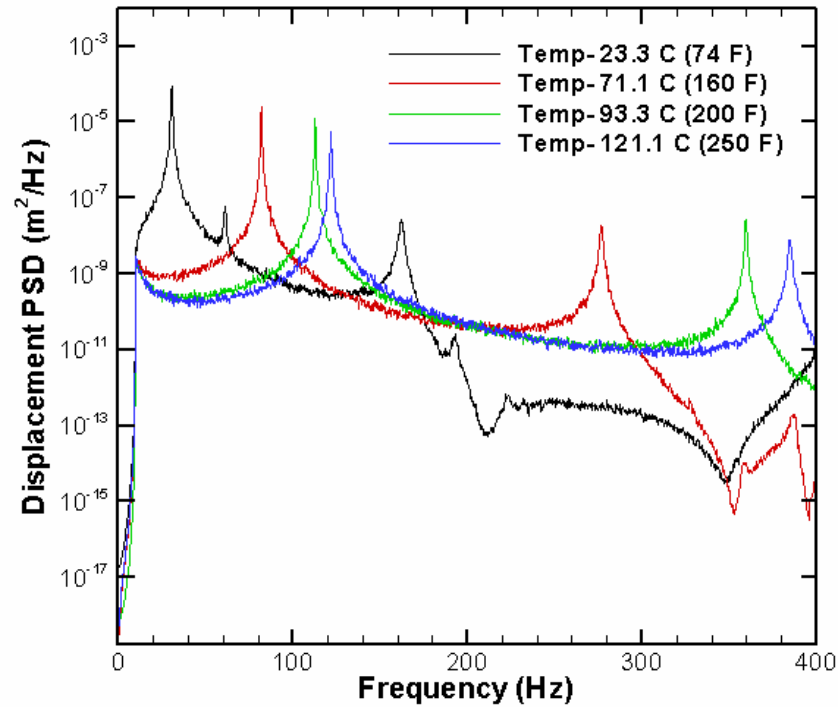


Figure 3.7- SMAHC Beam 2 PSD's for selected temperatures at position 2 (midspan).

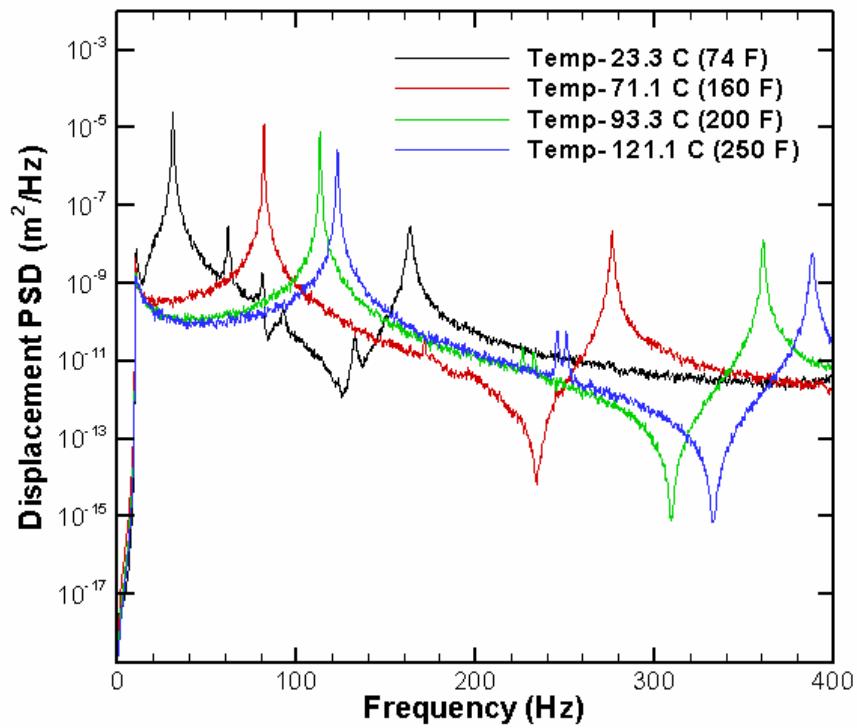


Figure 3.8- SMAHC Beam 2 PSD's for selected temperatures at position 3.

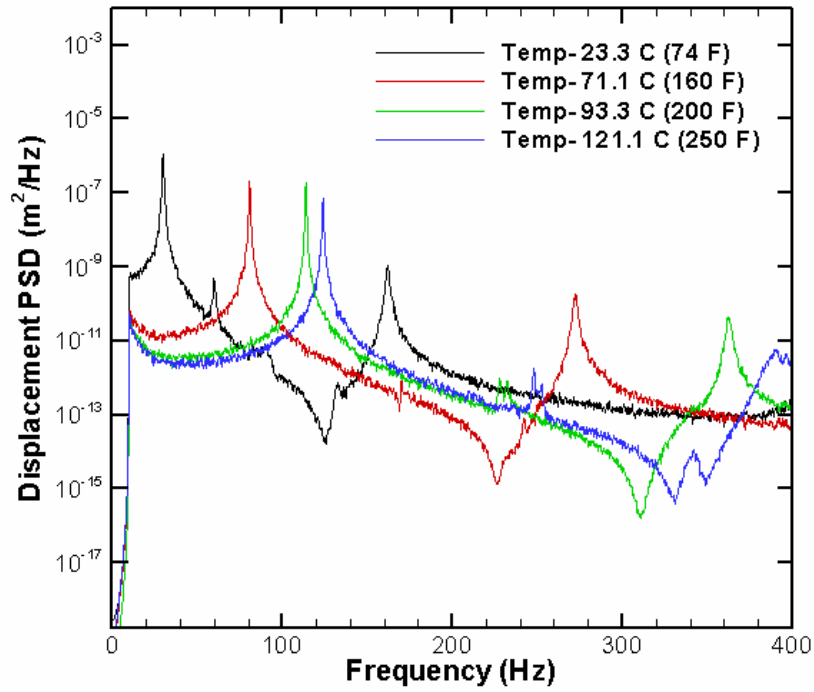


Figure 3.9- SMAHC Beam 3 PSD's for selected temperatures at position 1.

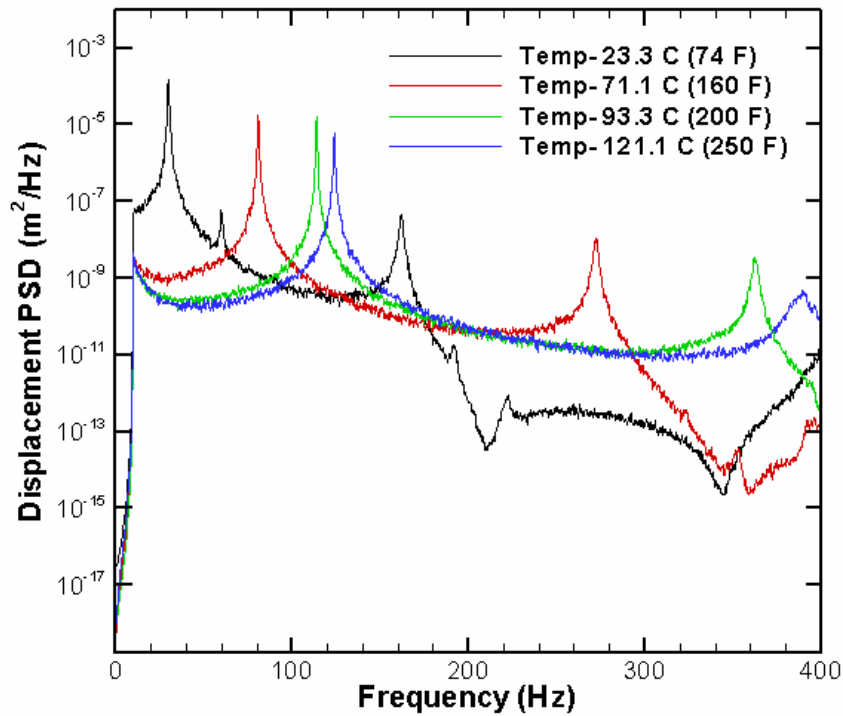


Figure 3.10- SMAHC Beam 3 PSD's at selected temperatures for position 2 (midspan).

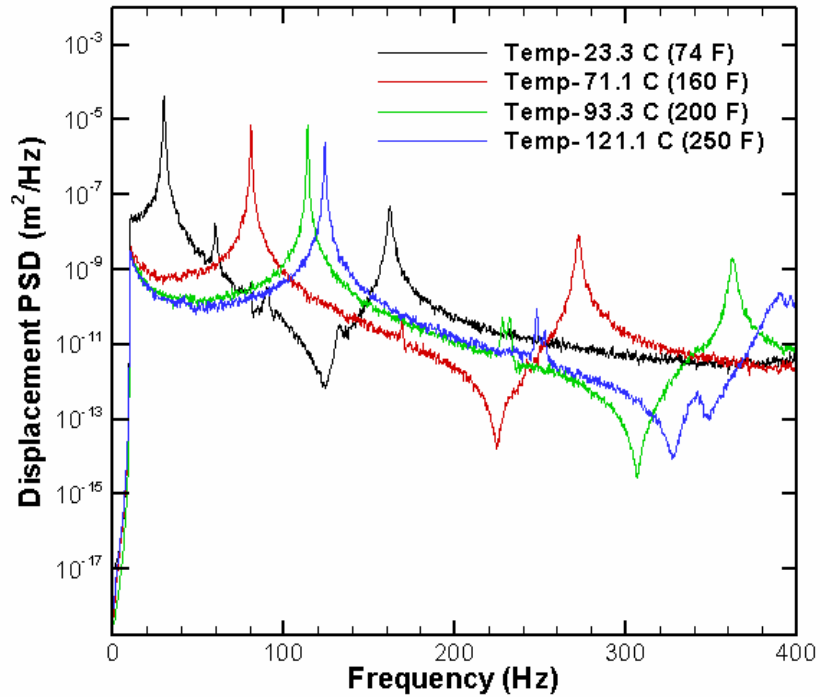


Figure 3.11- SMAHC Beam 3 PSD's at selected temperatures for position 3.

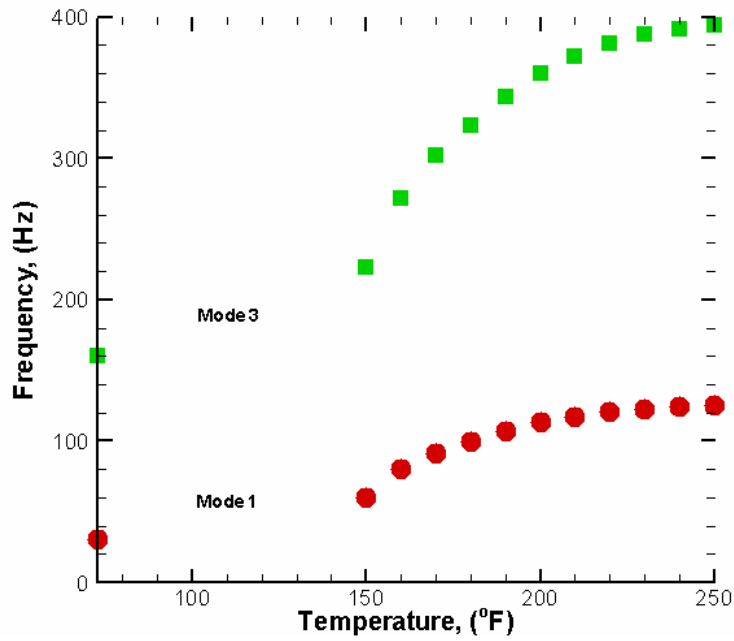


Figure 3.12- Modal frequency variation of modes 1, and 3 as a function of temperature.

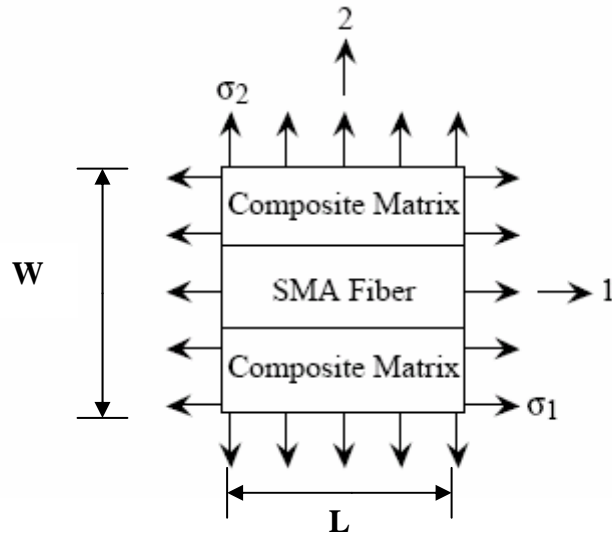


Figure 4.1- Representative volume element of SMAHC lamina¹⁸.

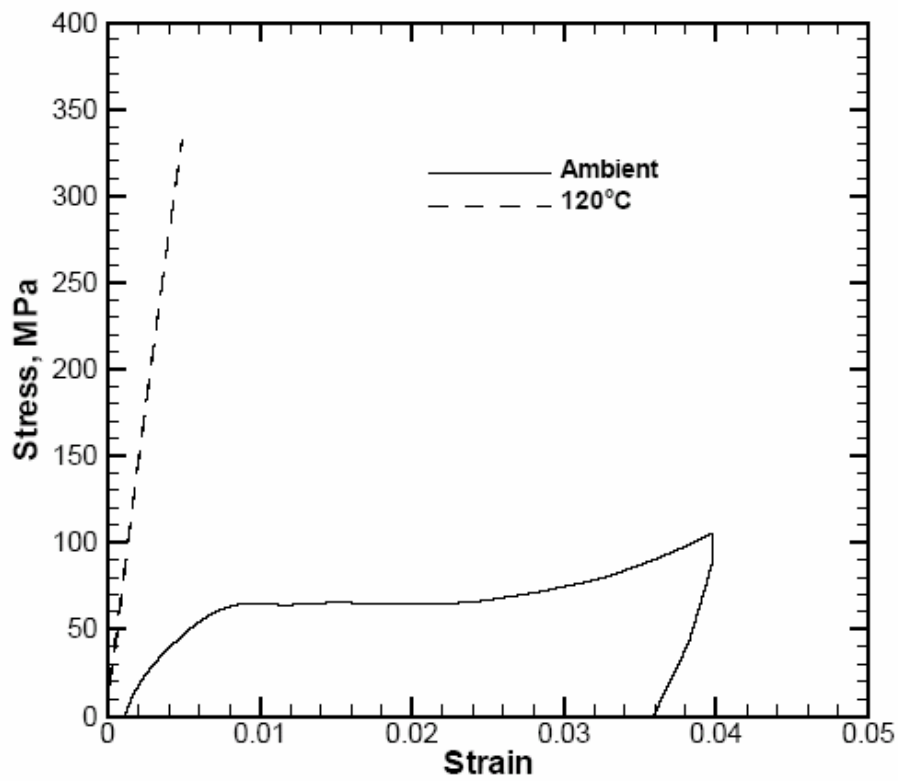


Figure 4.2- Applied stress vs. strain for .09x.006x10 inch sample with 0% pre-strain at ambient temperature and 120°C (248 °F)¹⁸.

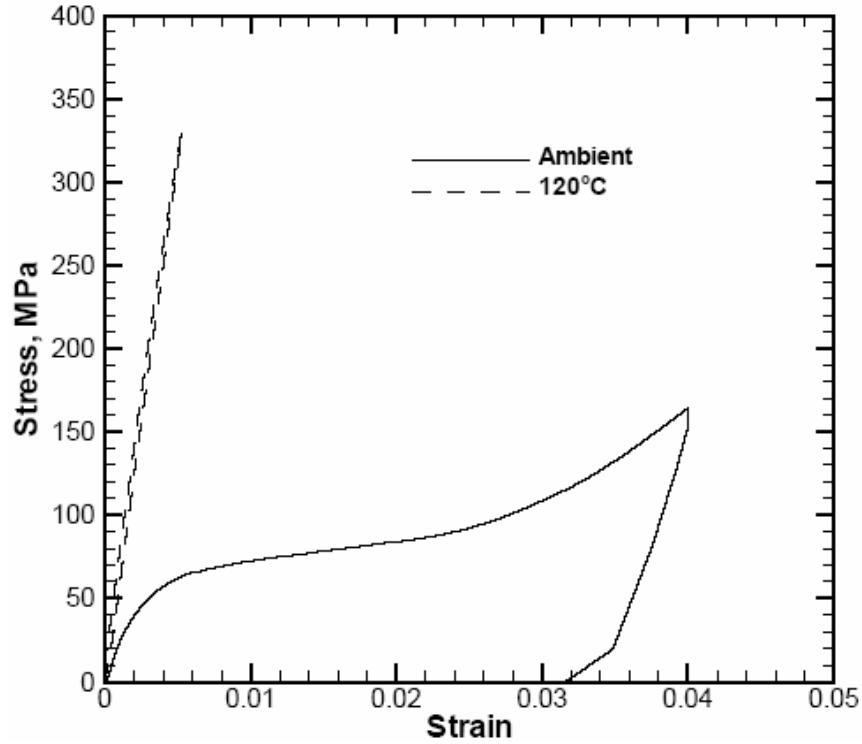


Figure 4.3– Applied stress vs. strain for .09x.006x10 inch sample with 4% pre-strain at ambient temperature and 120°C (248 °F)¹⁸.

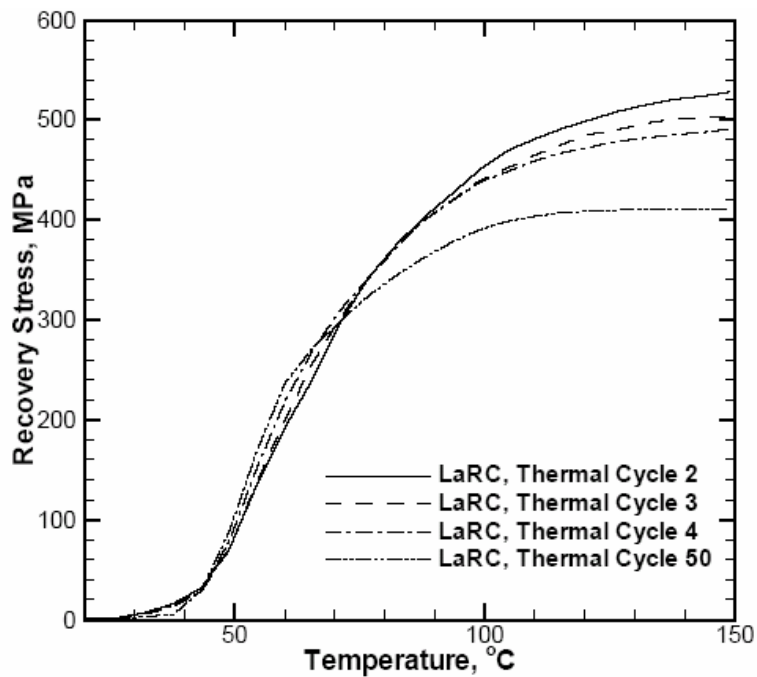


Figure 4.4– Recovery Stress vs. Temperature of the Nitinol ribbon (pre-strained 4% and released) for thermal cycles 2, 4, and 50¹⁸.

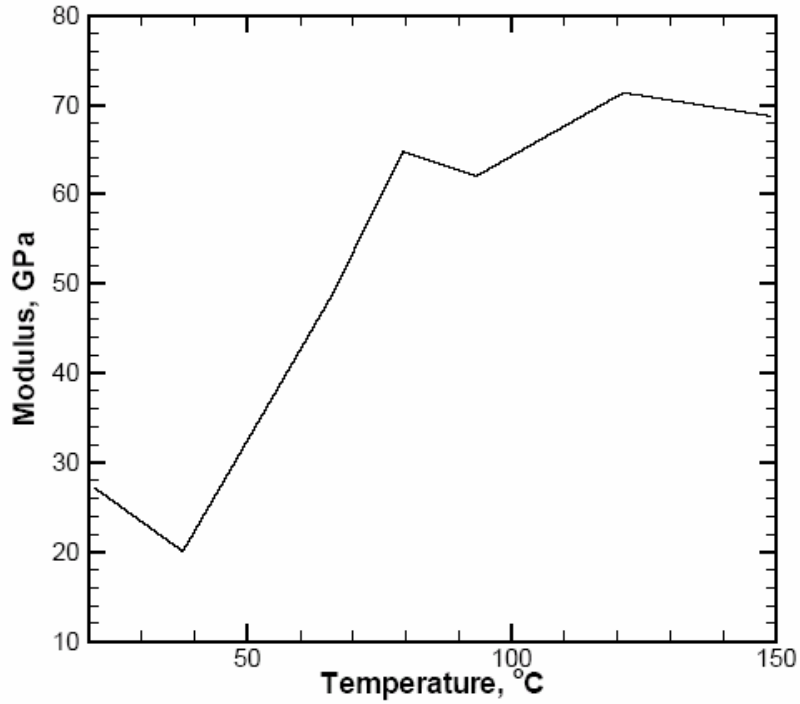


Figure 4.5– Modulus for Nitinol ribbon prestrained 4% and released as a function of temperature¹⁸.

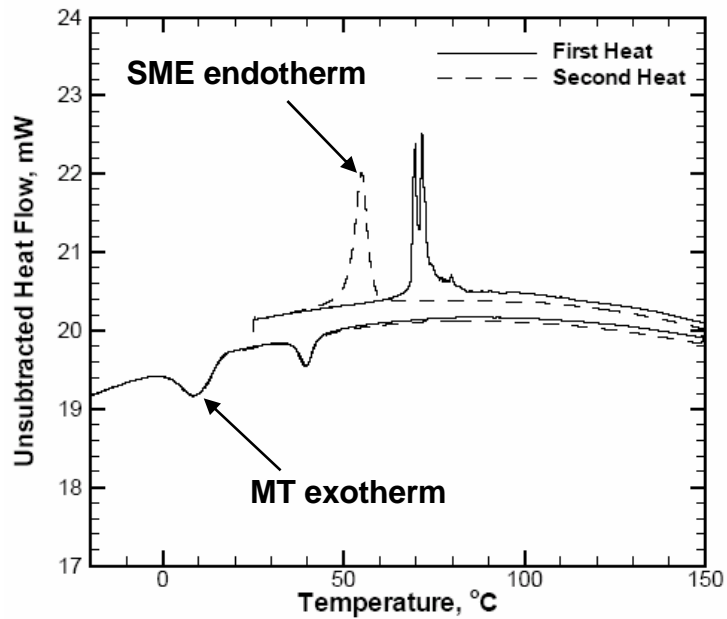


Figure 4.6- Differential Scanning Calorimetry (DSC) Results for the Nitinol ribbon sample showing transformation temperatures.



Figure 5.1- ABAQUS Finite Element Mesh of the SMAHC beam with clamped boundary conditions.

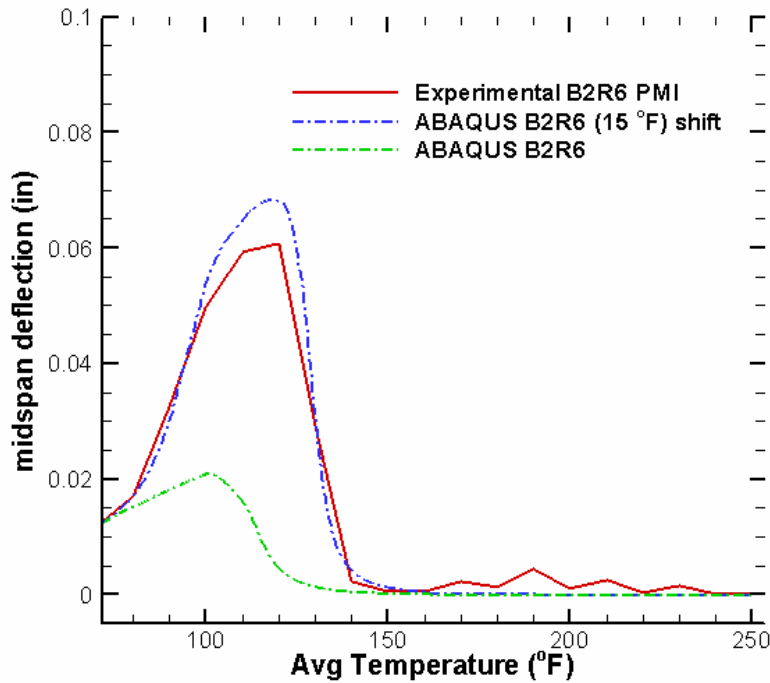


Figure 5.2- Static Response SMAHC Beam 2 Run 6 ABAQUS vs experimental results for original recovery force measurements, and 15 °F shift in recovery force input data.

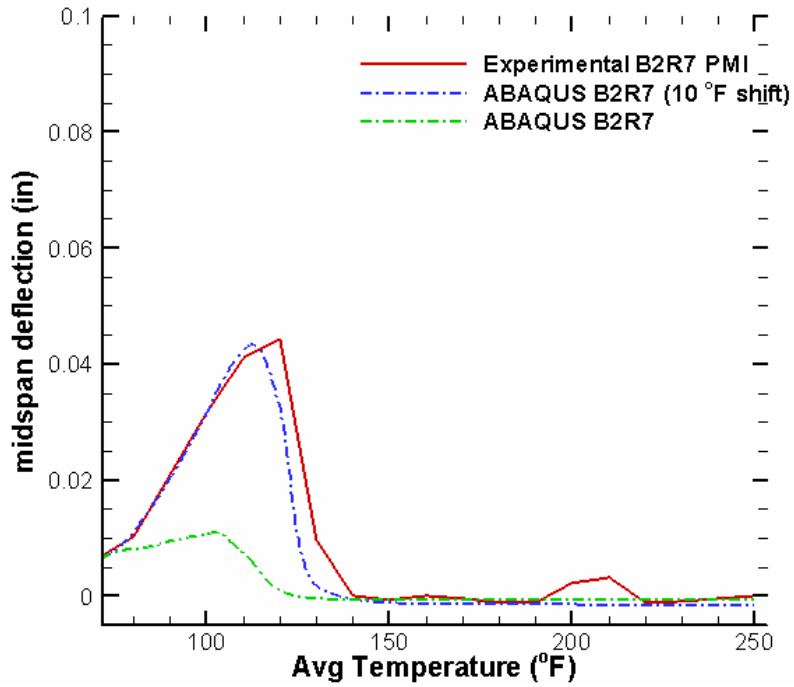


Figure 5.3– Static Response SMAHC Beam 2 Run 7 ABAQUS vs. experimental results for original recovery force measurements, and 10 °F shift in recovery force input data.

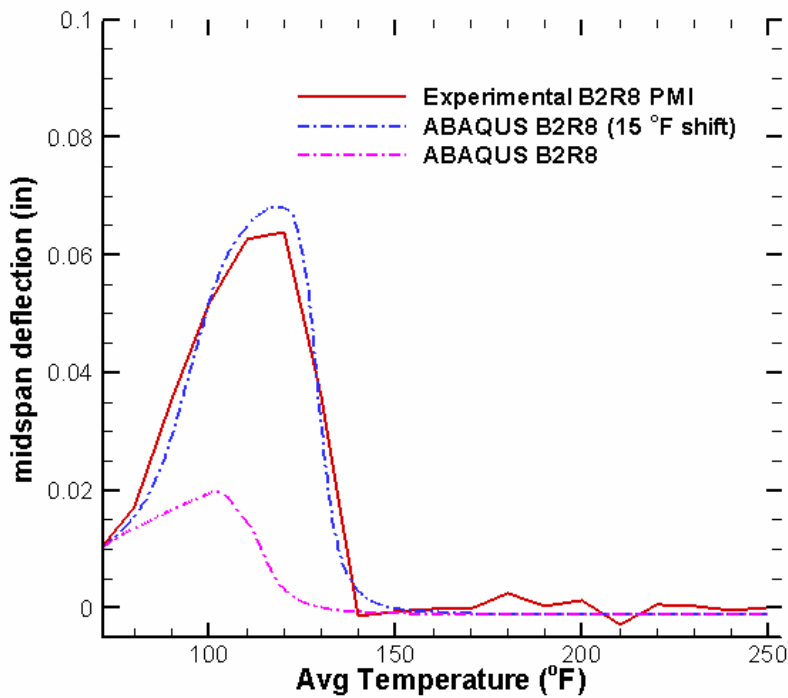


Figure 5.4- Static Response SMAHC Beam 2 Run 8 ABAQUS vs. experimental results for original recovery force measurements, and 15 °F shift in recovery force input data.

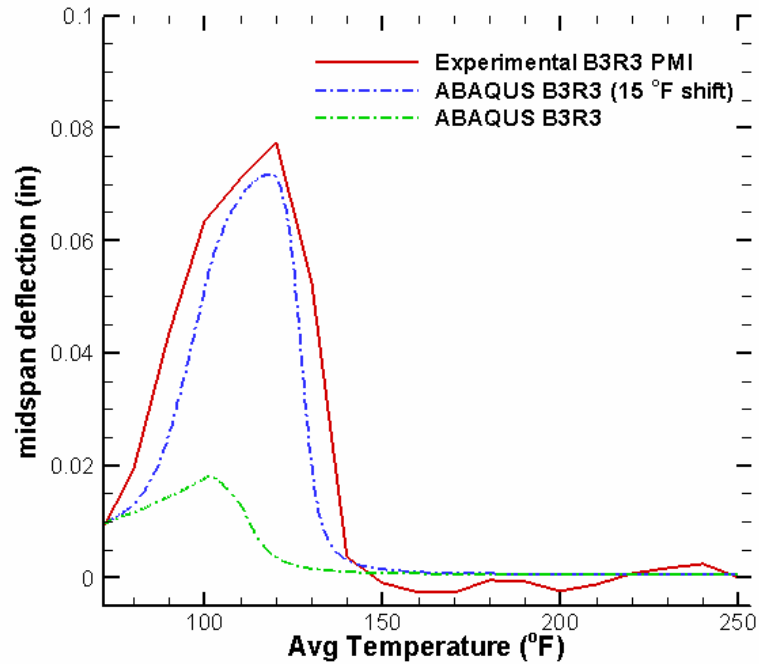


Figure 5.5- Static Response SMAHC Beam 3 Run 3 ABAQUS vs. experimental results for original recovery force measurements, and 15 °F shift in recovery force input data.

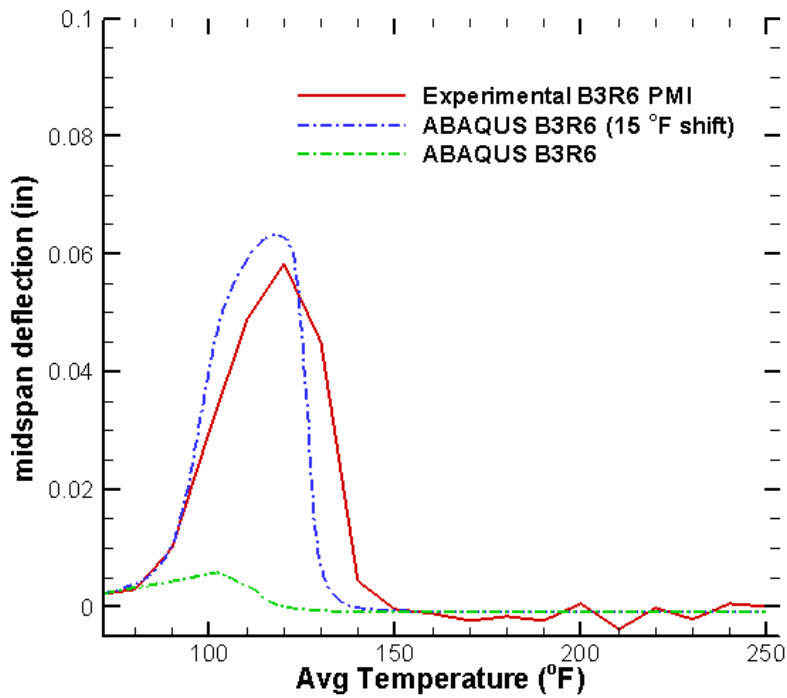


Figure 5.6- Static Response SMAHC Beam 3 Run 6 ABAQUS vs. experimental results for original recovery force measurements, and 15 °F shift in recovery force input data.

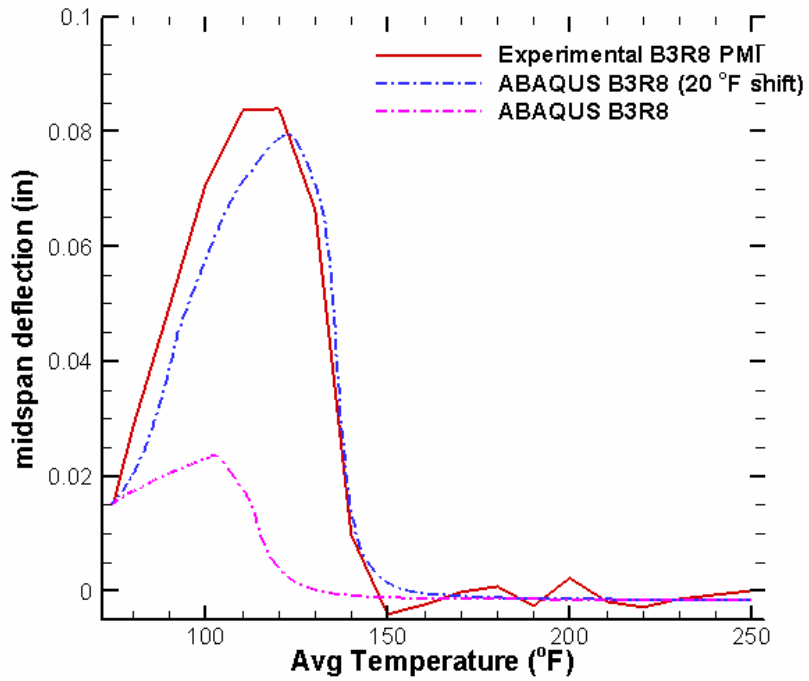


Figure 5.7- Static Response SMAHC Beam 3 Run 8 ABAQUS vs. experimental results for original recovery force measurements, and 20 °F shift in recovery force input data

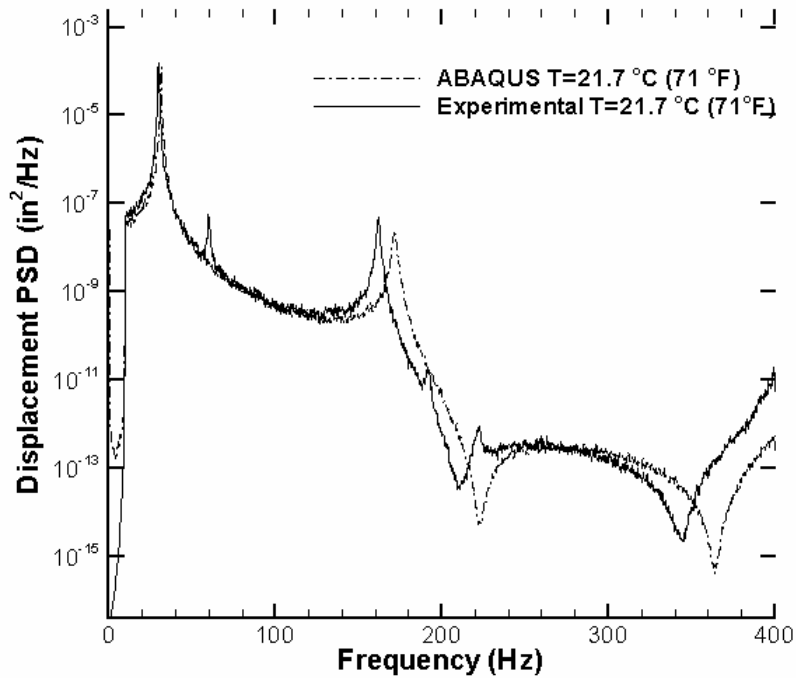


Figure 5.8- Beam 2 Run 8, position 2 (midspan) PSD comparison at ambient ($\Delta f=.25$ Hz).

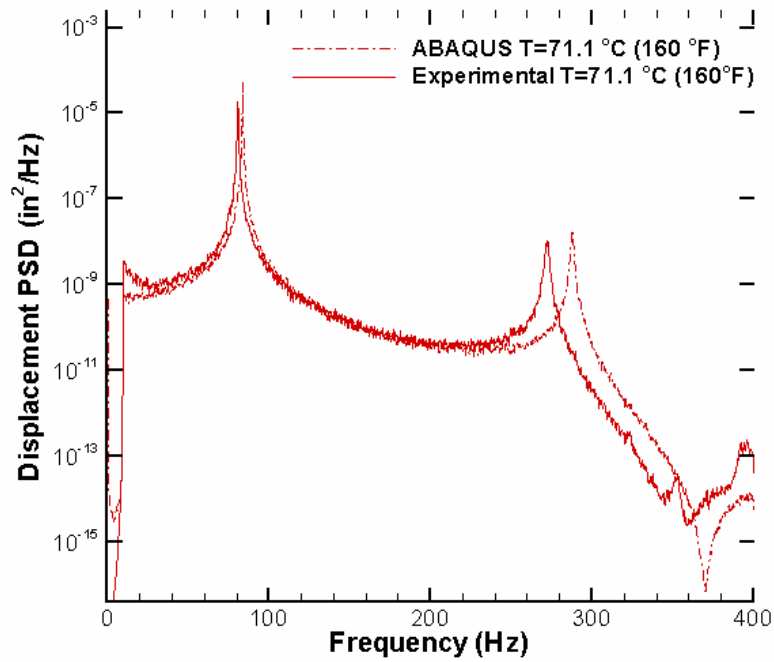


Figure 5.9- Beam 2 run 8, position 2 (Midspan) PSD comparison at 71.1 °C (160 °F) ($\Delta f=.25$ Hz).

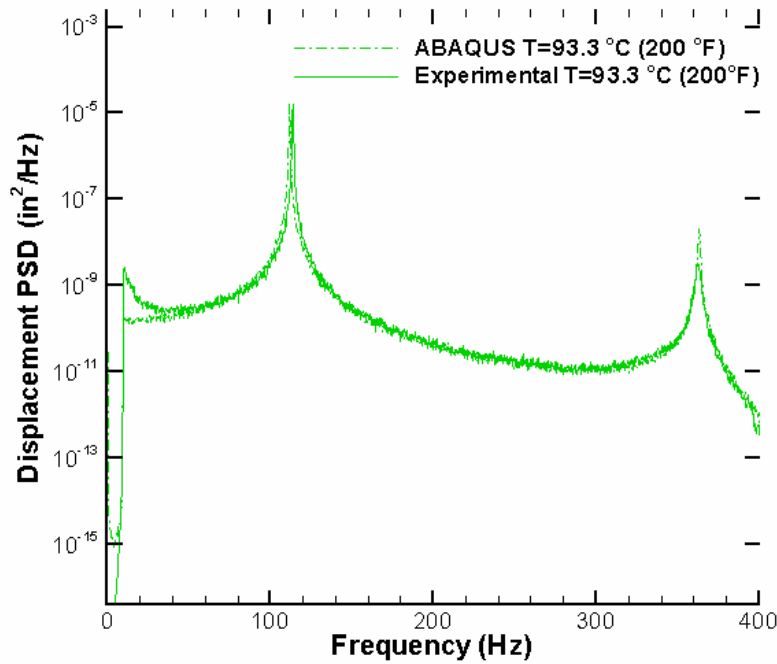


Figure 5.10- Beam 2 Run 8, position 2 (midspan) PSD comparison at 93.3 °C (200°F) ($\Delta f=.25$ Hz).

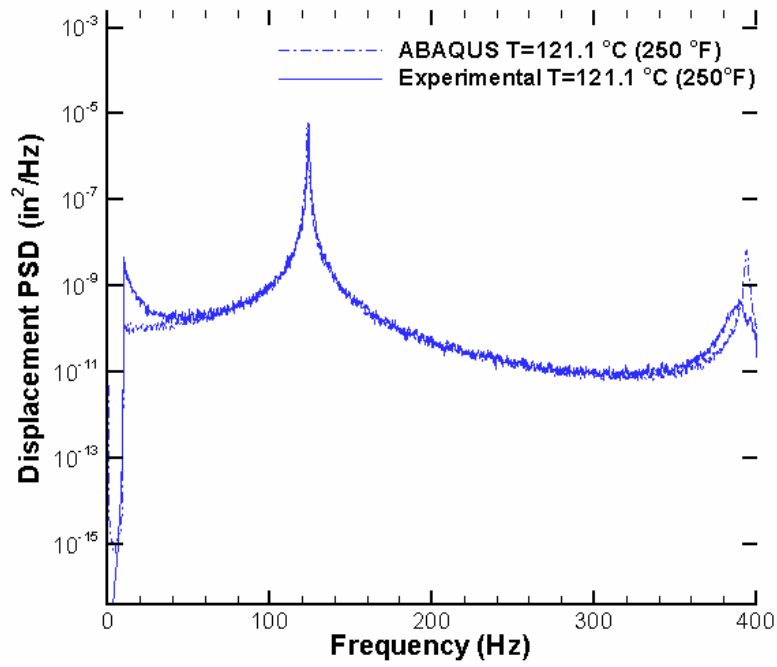


Figure 5.11- Beam 2 Run 8, position 2 (midspan) PSD comparison at 121.1 °C (250 °F).

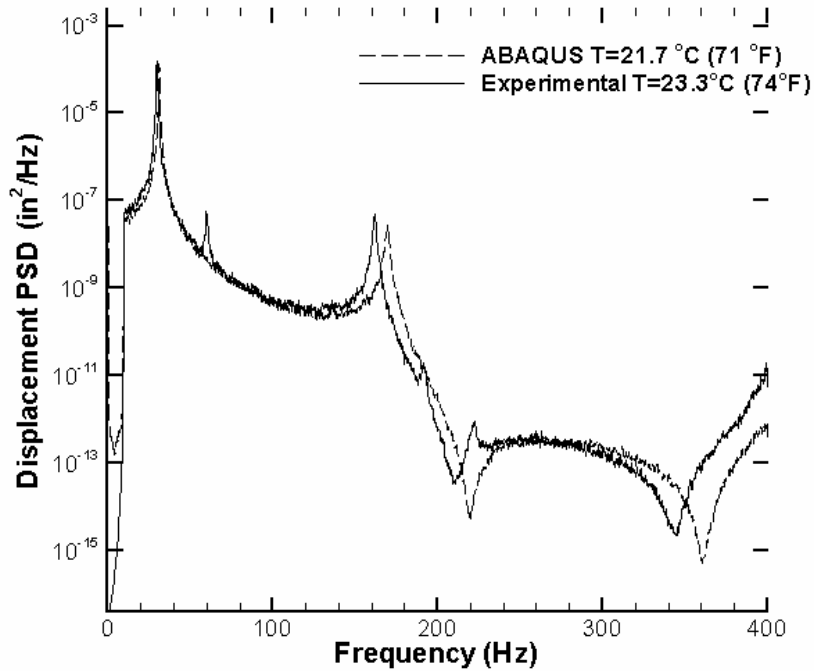


Figure 5.12- Beam 3 Run 8, position 2 (midspan) PSD comparison at 21.7 °C (71 °F) ($\Delta f = .25$ Hz).

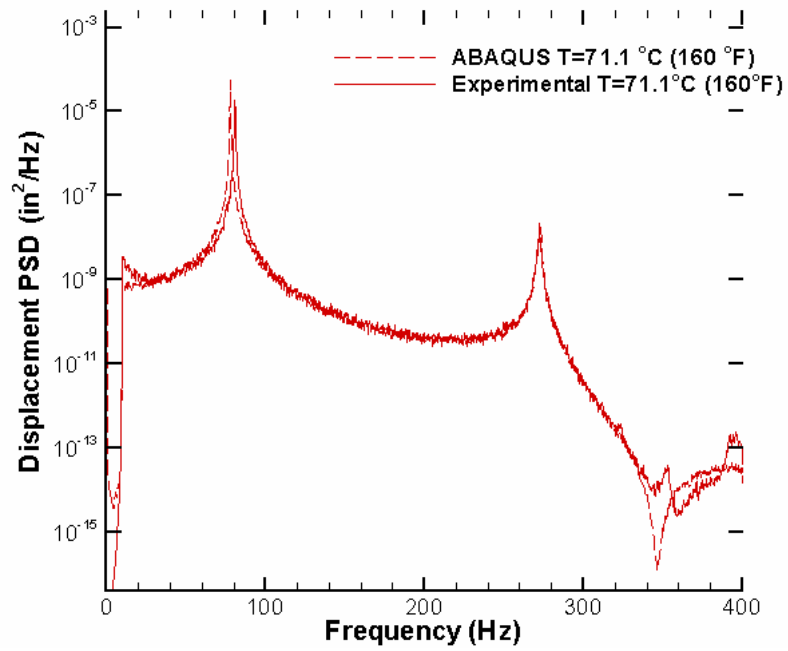


Figure 5.13- Beam 3 Run 8, position 2 (midspan) PSD comparison at 71.1 °C (160 °F) ($\Delta f=.25$ Hz).

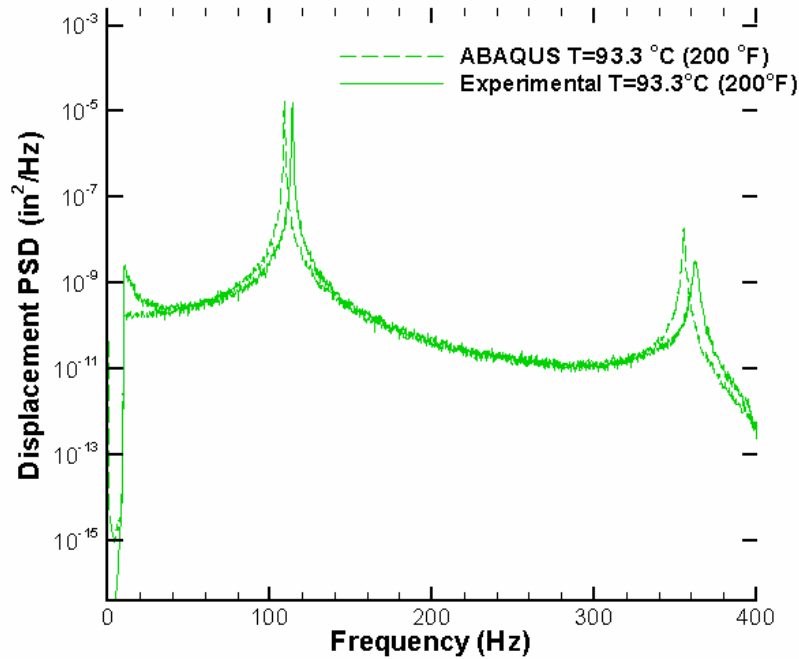


Figure 5.14- Beam 3 Run 8, position 2 (midspan) PSD comparison at 93.3 °C (200 °F) ($\Delta f=.25$ Hz).

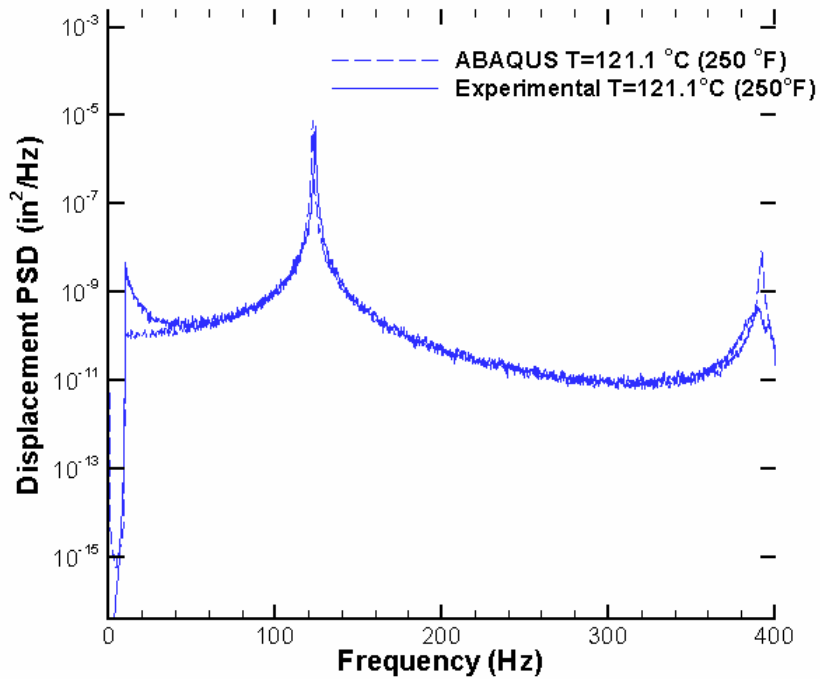


Figure 5.15- Beam 3 Run 8, position 2 (midspan) PSD comparison at 121.1 °C (250 °F) ($\Delta f = .25$ Hz).

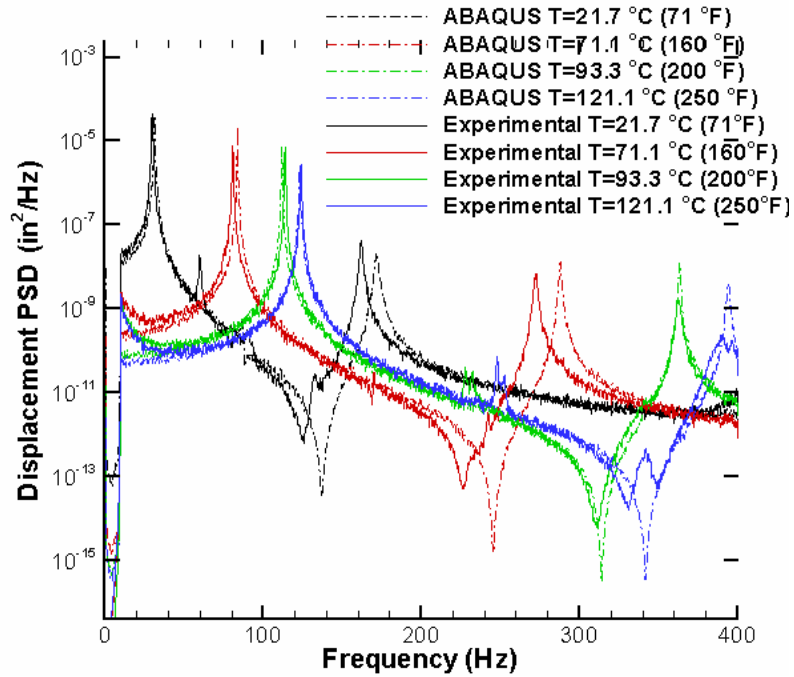


Figure 5.16- Beam 2 Run 8, position 1 PSD comparison for selected temperatures ($\Delta f = .25$ Hz).

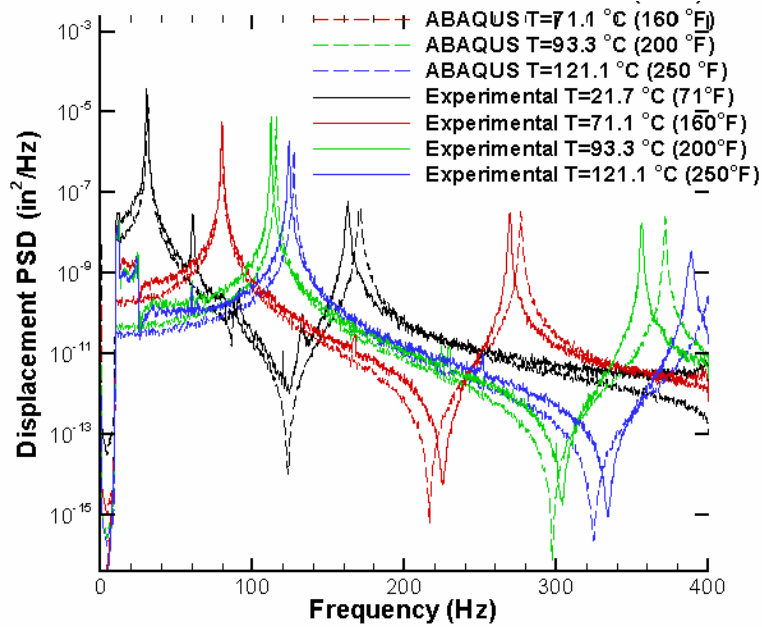


Figure 5.17- Beam 3 Run 3, position 3 PSD's comparison for selected temperatures ($\Delta f=.25$ Hz).

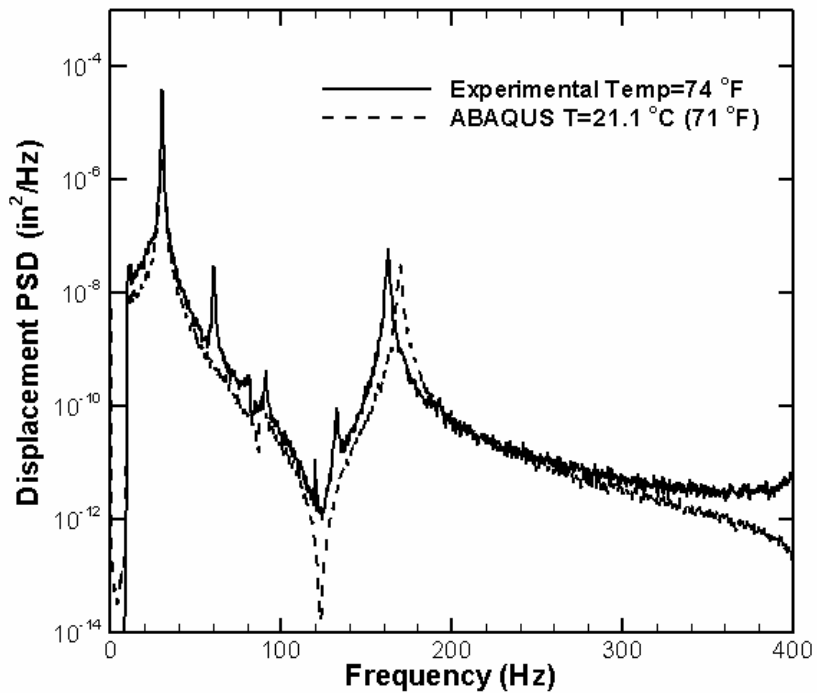


Figure 5.18- Beam 3 Run 1, position 3 PSD's comparison through the buckling range (T=71 °F).

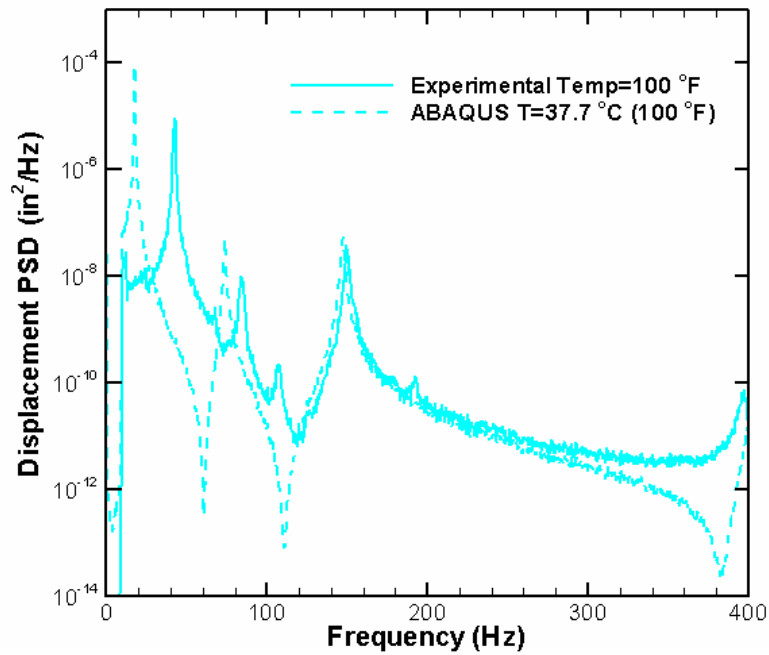


Figure 5.19- Beam 3 Run 1, position 3 PSD's comparison through the buckling range (T=100 °F).

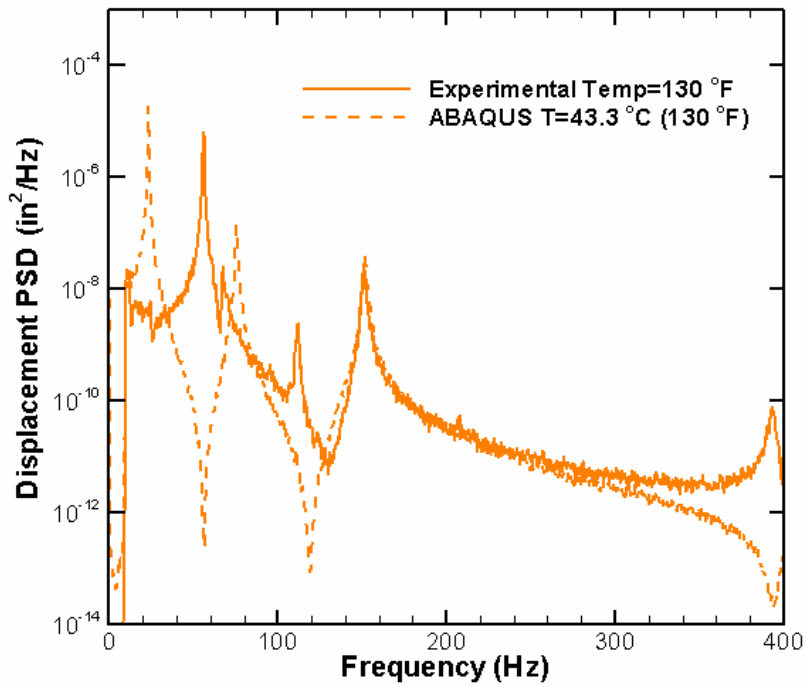


Figure 5.20- Beam 3 Run 1, position 3 PSD's comparison through the buckling range (T=130 °F).

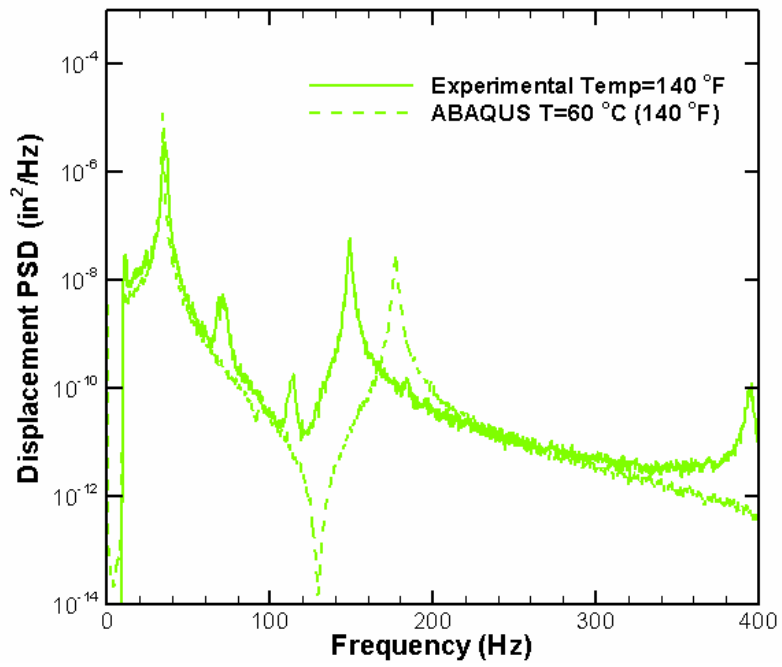


Figure 5.21- Beam 3 Run 1, position 3 PSD's comparison through the buckling range (T=140 °F).

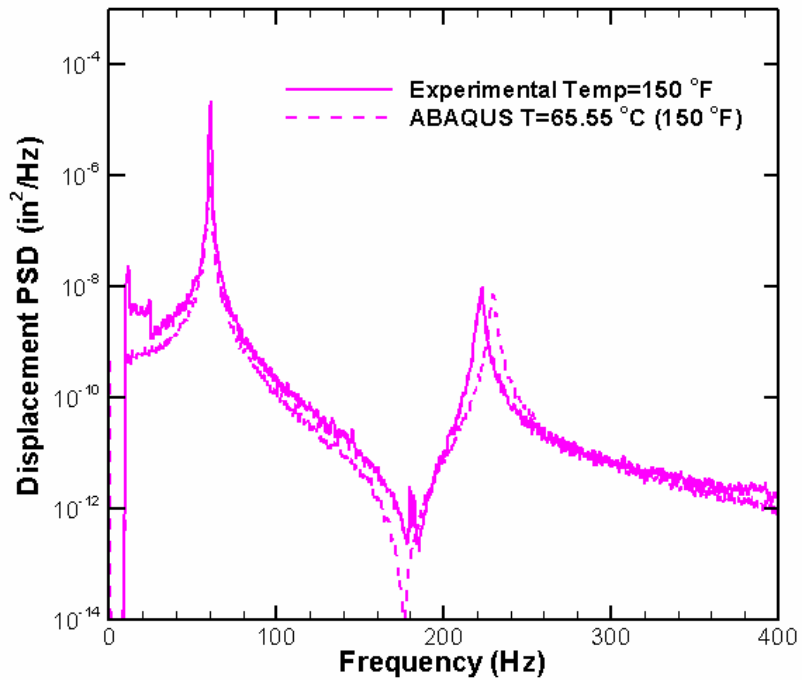


Figure 5.22- Beam 3 Run 1, position 3 PSD's comparison through the buckling range (T=150 °F).

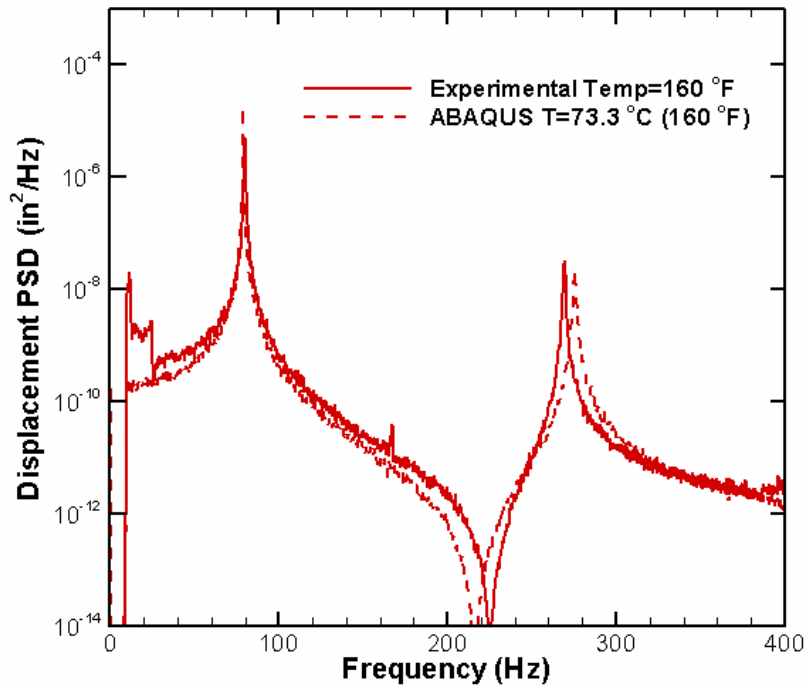


Figure 5.23- Beam 3 Run 1, position 3 PSD's comparison through the buckling range (T=160 °F).

Chapter 10

APPENDICES

APPENDIX A

Projection Moire' Interferrometry Thermoelastic Static Response Results

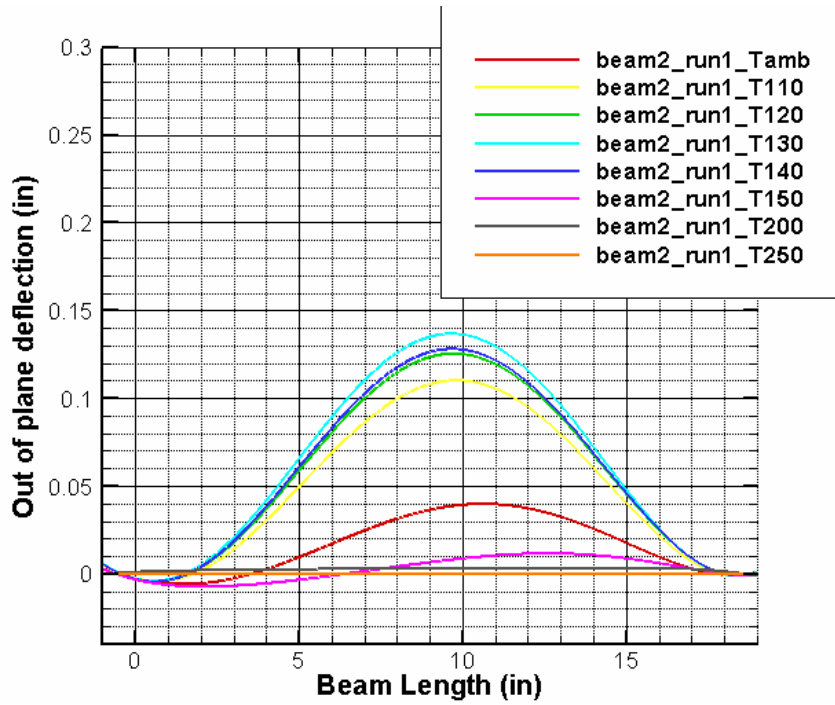


Figure 10.1- PMI full field imaging of the SMAHC Beam 2 Run 1.

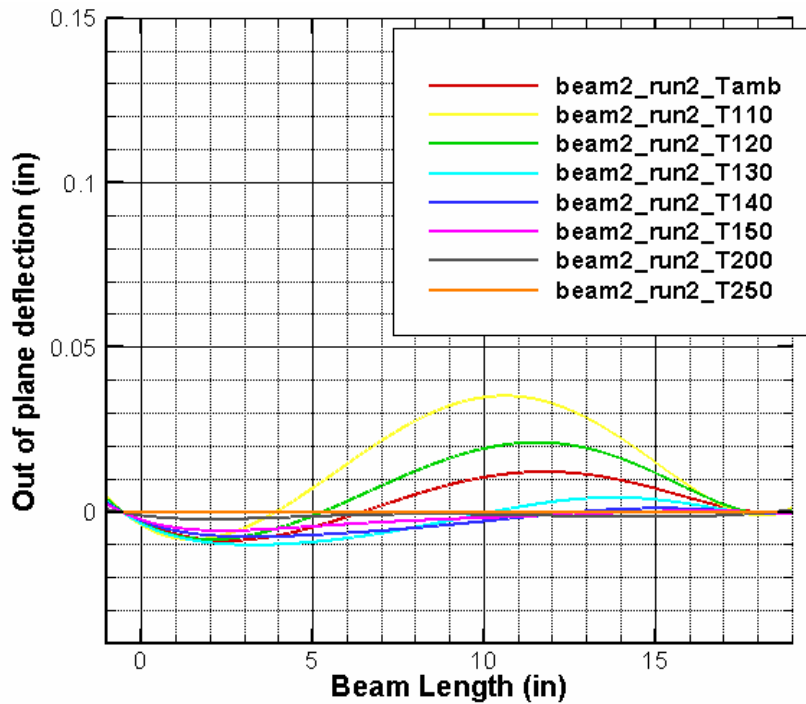


Figure 10.2- PMI full field imaging of the SMAHC Beam 2 Run 2.

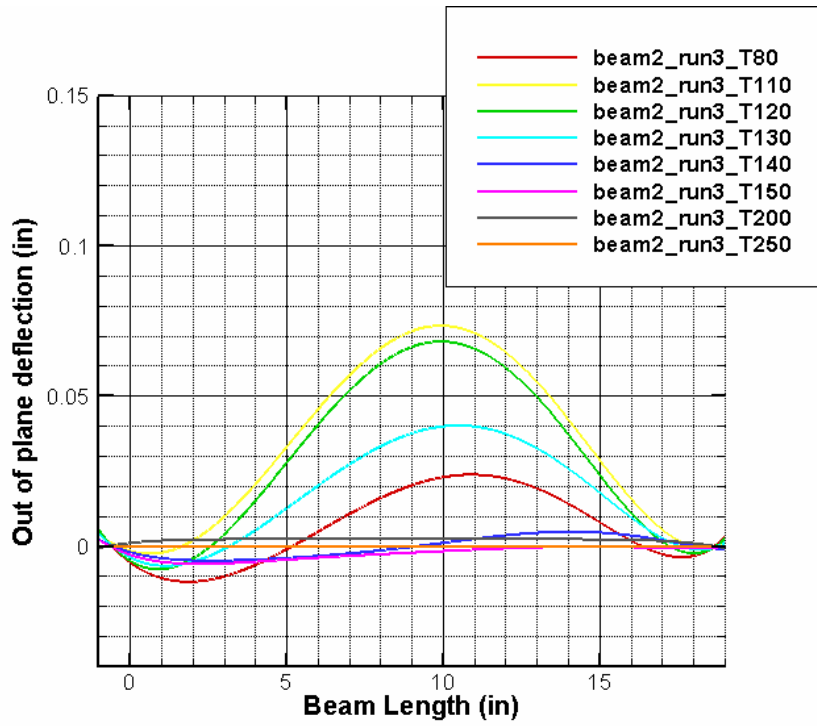


Figure 10.3- PMI full field imaging of the SMAHC Beam 2 Run 3.

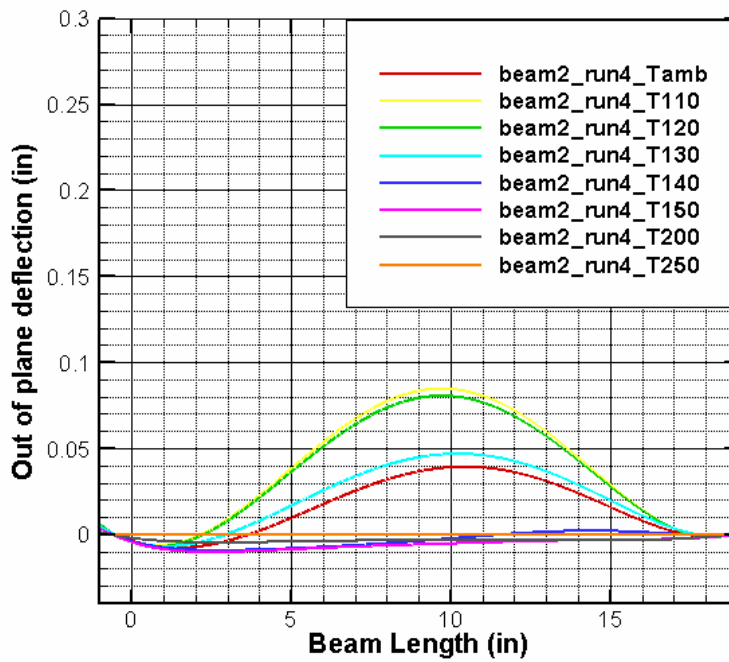


Figure 10.4- PMI full field imaging of the SMAHC Beam 2 Run 4.

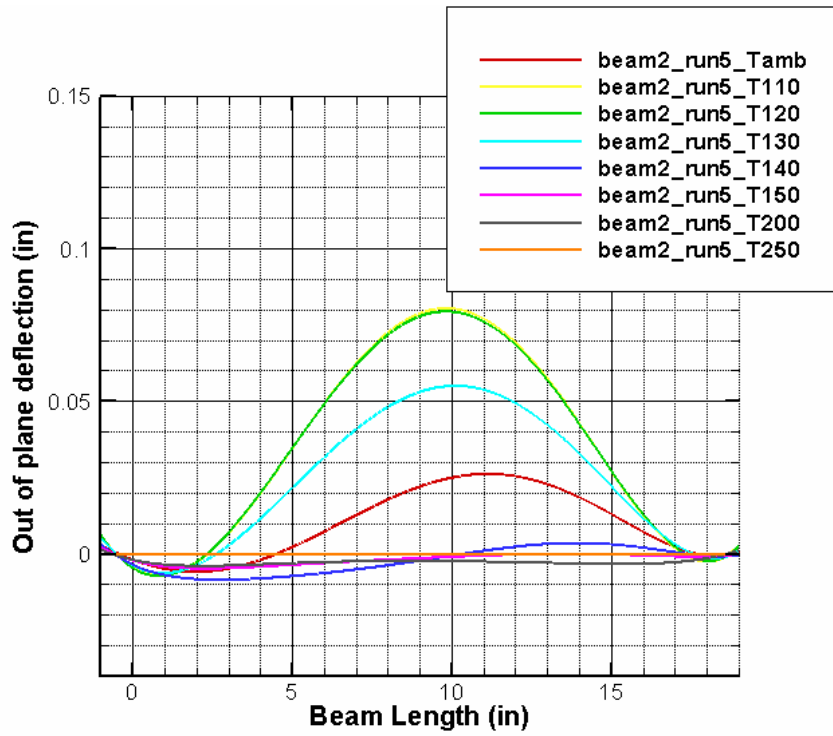


Figure 10.5- PMI full field imaging of the SMAHC Beam 2 Run 5.

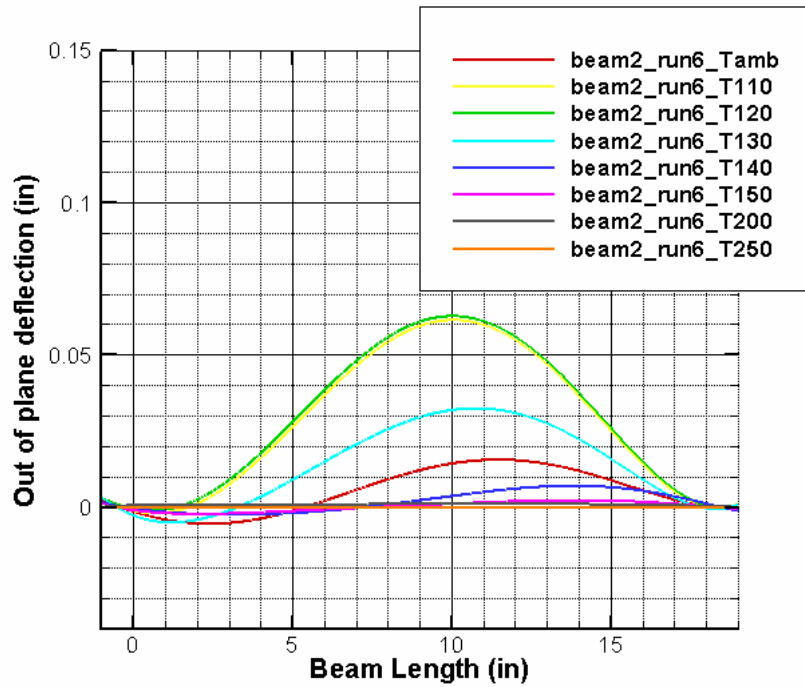


Figure 10.6- PMI full field imaging of the SMAHC Beam 2 Run 6.

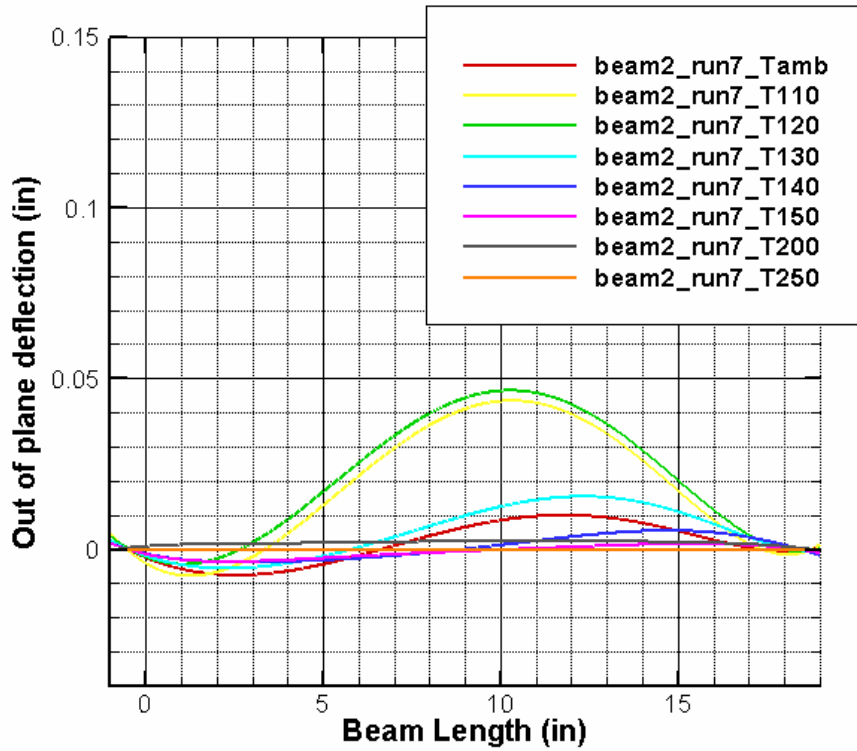


Figure 10.7- PMI full field imaging of the SMAHC Beam 2 Run 7.

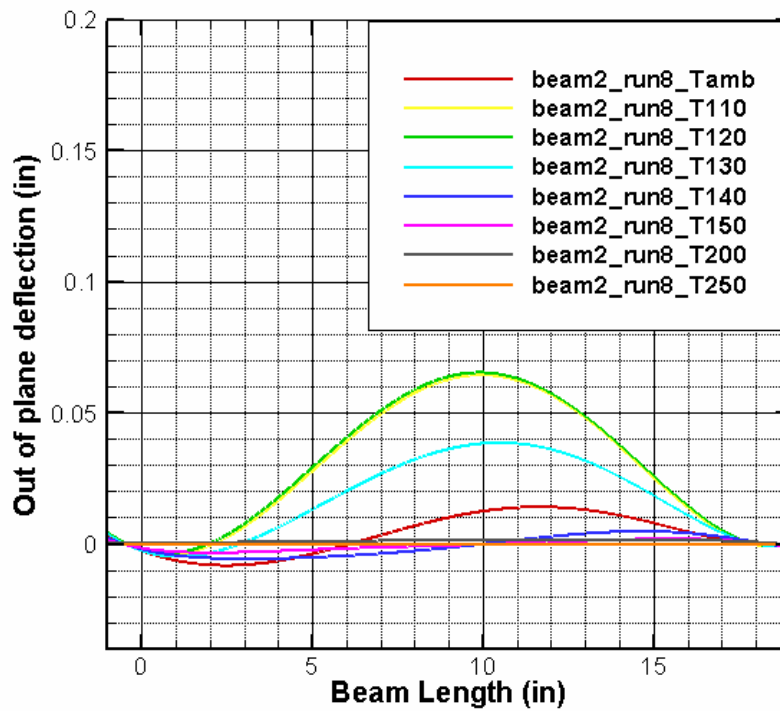


Figure 10.8- PMI full field imaging of the SMAHC Beam 2 Run 8.

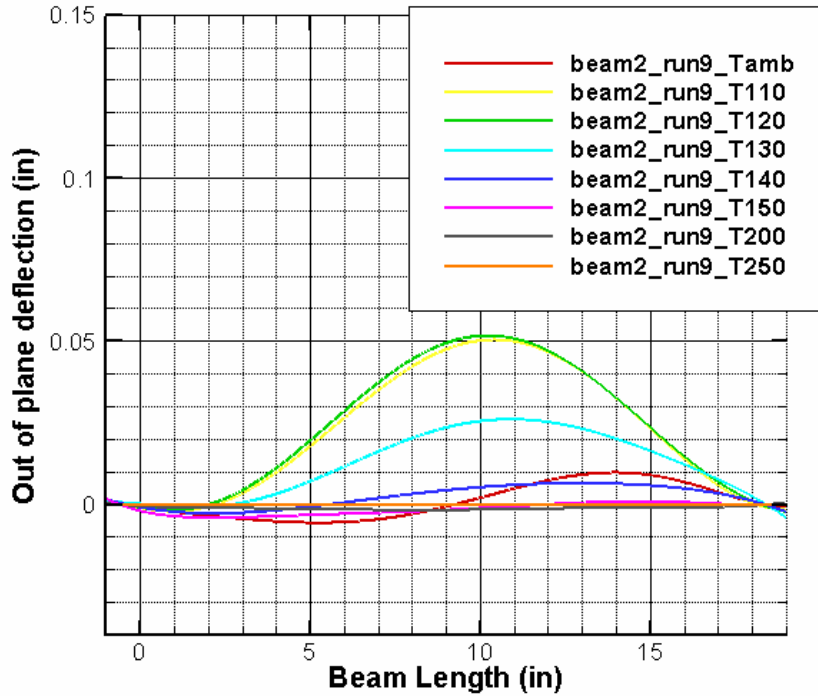


Figure 10.9- PMI full field imaging of the SMAHC Beam 2 Run 9.

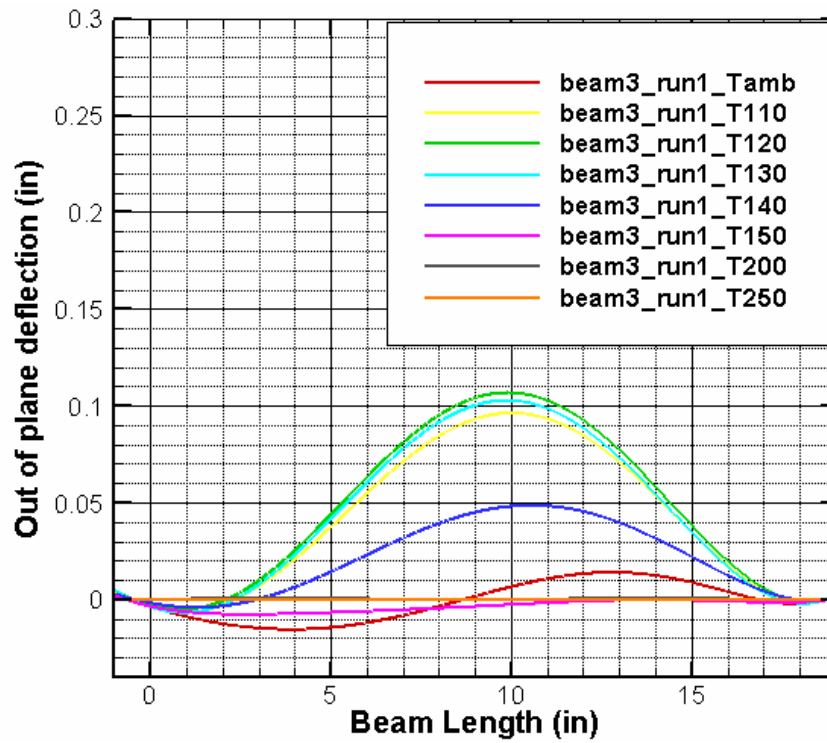


Figure 10.10- PMI full field imaging of the SMAHC Beam 3 Run 1.

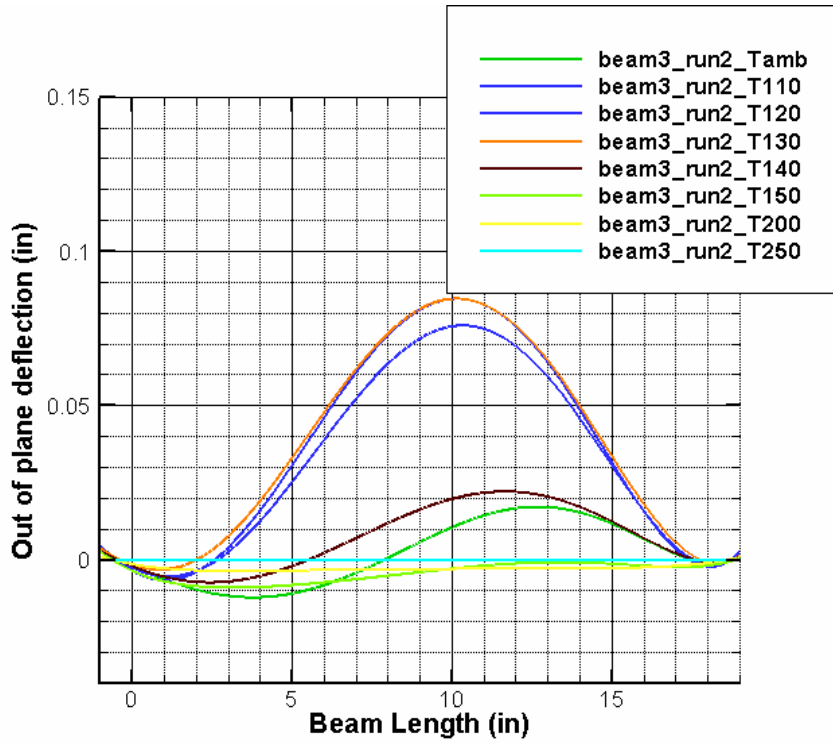


Figure 10.11- PMI full field imaging of the SMAHC Beam 3 Run 2.

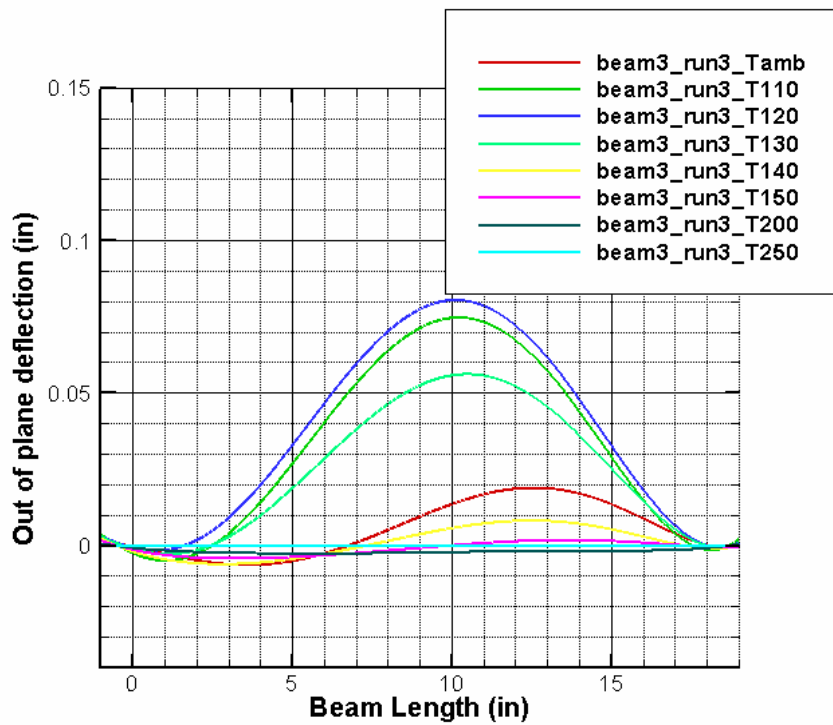


Figure 10.12- PMI full field imaging of the SMAHC Beam 3 Run 3.

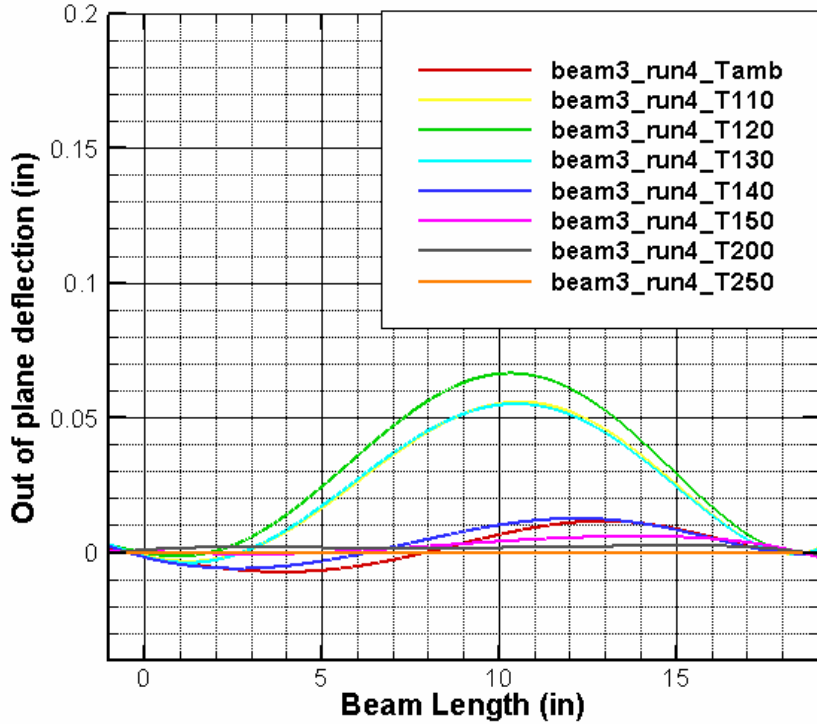


Figure 10.13- PMI full field imaging of the SMAHC Beam 3 Run 4.

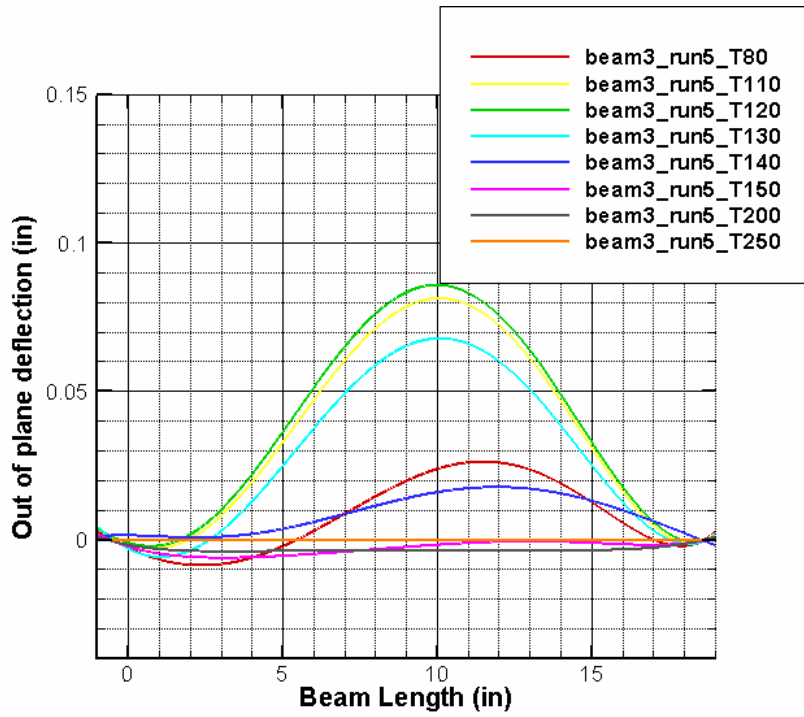


Figure 10.14- PMI full field imaging of the SMAHC Beam 3 Run 5.

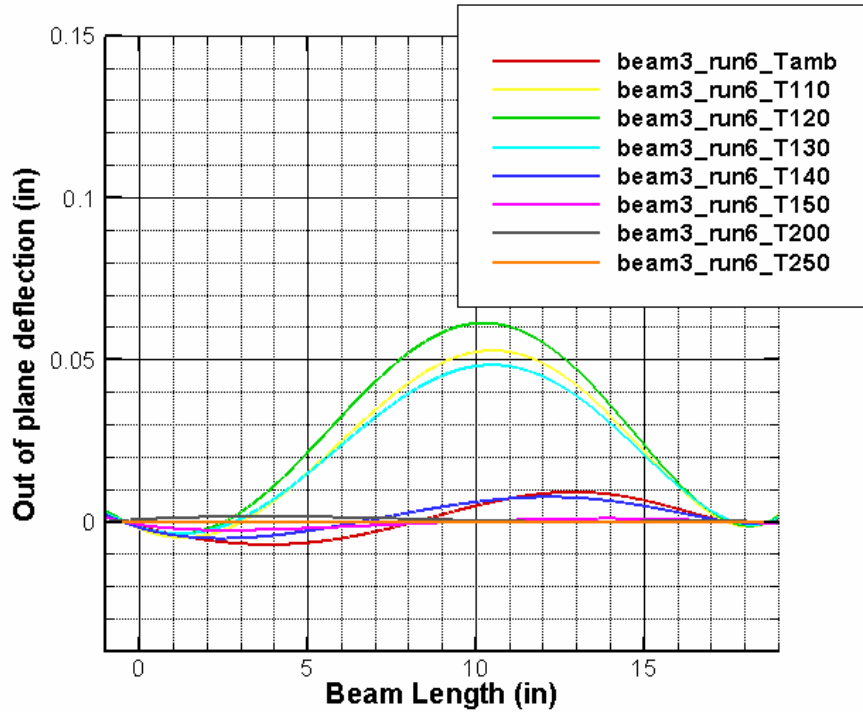


Figure 10.15- PMI full field imaging of the SMAHC Beam 3 Run 6.

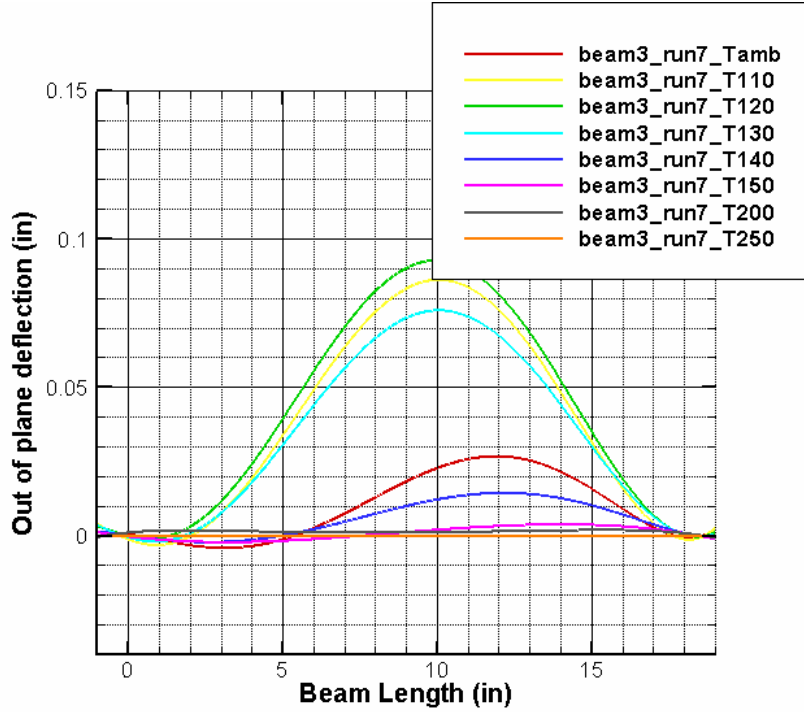


Figure 10.16- PMI full field imaging of the SMAHC Beam 3 Run 7.

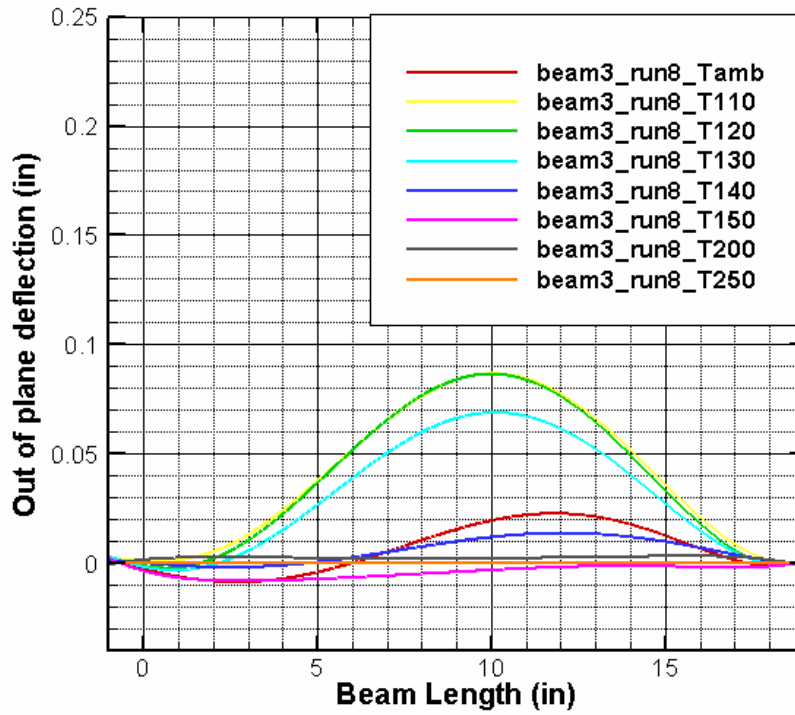


Figure 10.17- PMI full field imaging of the SMAHC Beam 3 Run 8.

APPENDIX B

Dynamic Acceleration Data Post Processing MATLAB code

```

%This code converts an acceleration time history data file into
%displacement time history data file by performing an FFT and then
%integrating to get displacement and transforming back to time history.
%Note that the code also deletes the low frequency noise present in our
%specific data file.

%Written by Brian Davis
%-----
clear;

%loads data file, generates acceleration and time vectors, and defines
%important constants

dataname=input('Enter the name of the data file: ','s');
data=[dataname, '.dat'];
fid=fopen(data, 'r');
%filename=fscanf(fid, '%s', 1);
%variables=fscanf(fid, '%s', 2);
[n, gh]=fscanf(fid, '%g %g', [2, inf]);
%fmin=input('0 to ? frequency value is the noise present in the data?');
fmin=10;
dt=n(1,2);
fnyq=1/(2*dt);
t=n(1,:)';
a=n(2,:)';
N=length(a);
ahat=fft(a);
%generates frequency vector
kmin=fix(fmin*N*dt);
knyq=fix(fnyq*N*dt);
k1=0:knyq;
k2=(knyq):-1:0;
k=[k1,k2]';
f=(1/(N*dt)).*k;

%generates displacement coefficients by integrating, and "zeros-out" the
%low frequency values.

dhat=(1./-(2*pi.*f).^2).*ahat;
for j=1:(kmin+1)
    dhat(j,:)=0;
end
for j=(N-(kmin+1)):N
    dhat(j,:)=0;
end

%inverse fft generates the displacement values

x=ifft(dhat);

%-----

%Compute PSD and RMS values from the generated displacement values
fs=1/dt;
df=1/(4096*dt);
[xspec, freq]=psd(x, 4096, fs, hanning(4096), 0);

```

```

xpsd=xspec/fnyq;
xrms=sqrt(sum(xpsd)*df);

%-----

%injects displacement and time vector into a matrix which is exported to a
%new data file. note that the 'w' writes to data file and the 't' keeps in
% text format so the carriage returns aren't deleted

data_file=[dataname '_disp.dat'];
data2=[t x]';
fid=fopen(data_file,'wt');
fprintf(fid,'variables = "t (sec)" "V (volts)" \n');
fprintf(fid,'%g %g\n',data2);
fclose(fid);

%Write the displacement fft coefficients to data file form

data_file=[dataname '_fft.dat'];
data2=[f dhat]';
fid=fopen(data_file,'wt');
fprintf(fid,'variables = "t (sec)" "V (volts)" \n');
fprintf(fid,'%g %g\n',data2);
fclose(fid);

%Write the displacement psd values to data file form

data_file=[dataname '_psd.dat'];
data2=[freq xpsd]';
fid=fopen(data_file,'wt');
fprintf(fid,'variables = "t (sec)" "V (volts)" \n');
fprintf(fid,'%g %g\n',data2);
fclose(fid);

%Write the displacement rms values to data file form

data_file=[dataname '_rms.dat'];
data2=[xrms]';
fid=fopen(data_file,'wt');
fprintf(fid,'variables = "t (sec)" "V (volts)" \n');
fprintf(fid,'%g %g\n',data2);
fclose(fid);
%-----

```

APPENDIX C

Initial Imperfection Data Linearly Interpolated to Node Set, MATLAB code.

```

%Brian Davis
%M-File that interprets experimental PMI data (deflection values in the z
%direction) to a defined node set.
%-----
-
%loads experimental data file
%-----
-
dataname=input('Enter the name of the datafile:', 's');
data=[dataname, '.dat'];
fid=fopen(data, 'r');
[n,gh]=fscanf(fid, '%g %g %g %g', [2, inf]);
x_data=n(1, :);
w_data=n(2, :);
%-----
%generate node set
%-----
nodes=(1:185)';
for i=1:185
    if i <= 37
        x(i)=(i-1)*.5;
        y(i)=0;
    elseif i > 37 & i <= 74
        x(i)=(i-38)*.5;
        y(i)=.275;
    elseif i > 74 & i <= 111
        x(i)=(i-75)*.5;
        y(i)=.5;
    elseif i > 111 & i <= 148
        x(i)=(i-112)*.5;
        y(i)=.725;
    else
        x(i)=(i-149)*.5;
        y(i)=1;
    end
end
mdl=[nodes, x, y];
%-----
% interprets the data file values to a matrix corresponding to the defined
% node sets initial deflection values (u,v,w).
%-----
w=interp1(x_data, w_data, mdl(:, 2));
uvw=[nodes, mdl(:, 2:3).*0, w];
%-----
% exports to a new data file representing the initial imperfection of the
% defined node set.
%-----
data_file=[dataname '_nodeset.dat'];
data2=[uvw]';
fid=fopen(data_file, 'wt');
fprintf(fid, 'variables = "node" "x coordinate" "y coordinate" "interp z
coordinate(imperfection)\n');
fprintf(fid, '%g, %f, %f, %f\n', data2);
fclose(fid);

```

APPENDIX D

ABAQUS Static and Dynamic Analysis Input File

*HEADING

Thermal post-buckling/random response of a SMAHC beam with initial imperfections

**

*NODE, NSET=ALL_NODES

1,	0.,	0.,	0.
2,	0.5,	0.,	0.
3,	1.,	0.,	0.
4,	1.5,	0.,	0.
5,	2.,	0.,	0.
6,	2.5,	0.,	0.
7,	3.,	0.,	0.
8,	3.5,	0.,	0.
9,	4.,	0.,	0.
10,	4.5,	0.,	0.
11,	5.,	0.,	0.
12,	5.5,	0.,	0.
13,	6.,	0.,	0.
14,	6.5,	0.,	0.
15,	7.,	0.,	0.
16,	7.5,	0.,	0.
17,	8.,	0.,	0.
18,	8.5,	0.,	0.
19,	9.,	0.,	0.
20,	9.5,	0.,	0.
21,	10.,	0.,	0.
22,	10.5,	0.,	0.
23,	11.,	0.,	0.
24,	11.5,	0.,	0.
25,	12.,	0.,	0.
26,	12.5,	0.,	0.
27,	13.,	0.,	0.
28,	13.5,	0.,	0.
29,	14.,	0.,	0.
30,	14.5,	0.,	0.
31,	15.,	0.,	0.
32,	15.5,	0.,	0.
33,	16.,	0.,	0.
34,	16.5,	0.,	0.
35,	17.,	0.,	0.
36,	17.5,	0.,	0.
37,	18.,	0.,	0.
38,	0.,	0.275,	0.
39,	0.5,	0.275,	0.
40,	1.,	0.275,	0.
41,	1.5,	0.275,	0.
42,	2.,	0.275,	0.
43,	2.5,	0.275,	0.
44,	3.,	0.275,	0.
45,	3.5,	0.275,	0.
46,	4.,	0.275,	0.
47,	4.5,	0.275,	0.
48,	5.,	0.275,	0.
49,	5.5,	0.275,	0.
50,	6.,	0.275,	0.
51,	6.5,	0.275,	0.
52,	7.,	0.275,	0.

53,	7.5,	0.275,	0.
54,	8.,	0.275,	0.
55,	8.5,	0.275,	0.
56,	9.,	0.275,	0.
57,	9.5,	0.275,	0.
58,	10.,	0.275,	0.
59,	10.5,	0.275,	0.
60,	11.,	0.275,	0.
61,	11.5,	0.275,	0.
62,	12.,	0.275,	0.
63,	12.5,	0.275,	0.
64,	13.,	0.275,	0.
65,	13.5,	0.275,	0.
66,	14.,	0.275,	0.
67,	14.5,	0.275,	0.
68,	15.,	0.275,	0.
69,	15.5,	0.275,	0.
70,	16.,	0.275,	0.
71,	16.5,	0.275,	0.
72,	17.,	0.275,	0.
73,	17.5,	0.275,	0.
74,	18.,	0.275,	0.
75,	0.,	0.5,	0.
76,	0.5,	0.5,	0.
77,	1.,	0.5,	0.
78,	1.5,	0.5,	0.
79,	2.,	0.5,	0.
80,	2.5,	0.5,	0.
81,	3.,	0.5,	0.
82,	3.5,	0.5,	0.
83,	4.,	0.5,	0.
84,	4.5,	0.5,	0.
85,	5.,	0.5,	0.
86,	5.5,	0.5,	0.
87,	6.,	0.5,	0.
88,	6.5,	0.5,	0.
89,	7.,	0.5,	0.
90,	7.5,	0.5,	0.
91,	8.,	0.5,	0.
92,	8.5,	0.5,	0.
93,	9.,	0.5,	0.
94,	9.5,	0.5,	0.
95,	10.,	0.5,	0.
96,	10.5,	0.5,	0.
97,	11.,	0.5,	0.
98,	11.5,	0.5,	0.
99,	12.,	0.5,	0.
100,	12.5,	0.5,	0.
101,	13.,	0.5,	0.
102,	13.5,	0.5,	0.
103,	14.,	0.5,	0.
104,	14.5,	0.5,	0.
105,	15.,	0.5,	0.
106,	15.5,	0.5,	0.
107,	16.,	0.5,	0.
108,	16.5,	0.5,	0.
109,	17.,	0.5,	0.

110,	17.5,	0.5,	0.
111,	18.,	0.5,	0.
112,	0.,	0.725,	0.
113,	0.5,	0.725,	0.
114,	1.,	0.725,	0.
115,	1.5,	0.725,	0.
116,	2.,	0.725,	0.
117,	2.5,	0.725,	0.
118,	3.,	0.725,	0.
119,	3.5,	0.725,	0.
120,	4.,	0.725,	0.
121,	4.5,	0.725,	0.
122,	5.,	0.725,	0.
123,	5.5,	0.725,	0.
124,	6.,	0.725,	0.
125,	6.5,	0.725,	0.
126,	7.,	0.725,	0.
127,	7.5,	0.725,	0.
128,	8.,	0.725,	0.
129,	8.5,	0.725,	0.
130,	9.,	0.725,	0.
131,	9.5,	0.725,	0.
132,	10.,	0.725,	0.
133,	10.5,	0.725,	0.
134,	11.,	0.725,	0.
135,	11.5,	0.725,	0.
136,	12.,	0.725,	0.
137,	12.5,	0.725,	0.
138,	13.,	0.725,	0.
139,	13.5,	0.725,	0.
140,	14.,	0.725,	0.
141,	14.5,	0.725,	0.
142,	15.,	0.725,	0.
143,	15.5,	0.725,	0.
144,	16.,	0.725,	0.
145,	16.5,	0.725,	0.
146,	17.,	0.725,	0.
147,	17.5,	0.725,	0.
148,	18.,	0.725,	0.
149,	0.,	1.,	0.
150,	0.5,	1.,	0.
151,	1.,	1.,	0.
152,	1.5,	1.,	0.
153,	2.,	1.,	0.
154,	2.5,	1.,	0.
155,	3.,	1.,	0.
156,	3.5,	1.,	0.
157,	4.,	1.,	0.
158,	4.5,	1.,	0.
159,	5.,	1.,	0.
160,	5.5,	1.,	0.
161,	6.,	1.,	0.
162,	6.5,	1.,	0.
163,	7.,	1.,	0.
164,	7.5,	1.,	0.
165,	8.,	1.,	0.
166,	8.5,	1.,	0.

```

167,      9.,      1.,      0.
168,     9.5,     1.,     0.
169,    10.,     1.,     0.
170,   10.5,     1.,     0.
171,   11.,     1.,     0.
172,   11.5,     1.,     0.
173,   12.,     1.,     0.
174,   12.5,     1.,     0.
175,   13.,     1.,     0.
176,   13.5,     1.,     0.
177,   14.,     1.,     0.
178,   14.5,     1.,     0.
179,   15.,     1.,     0.
180,   15.5,     1.,     0.
181,   16.,     1.,     0.
182,   16.5,     1.,     0.
183,   17.,     1.,     0.
184,   17.5,     1.,     0.
185,   18.,     1.,     0.
**
*NSET, NSET=CENTER
93,
*NSET, NSET=ACCELS
84, 93, 104
**
** Read geometric imperfection data from external file
**
*IMPERFECTION, INPUT=beam2_run7_pmi_imp_nodeset.dat
**
** -----
** --- Include temp. dependent material properties ---
** -----
**
** GLEP
** Date: 13-Nov-03           Time: 16:50:42
**
*MATERIAL, NAME=GLEP
*ELASTIC, TYPE=LAMINA
** E1,      E2,      nu12,      G12,      G13,      G23,      T
7.15e+6, 2.90e+6, 0.29, 1.40e+6, 1.40e+6, 1.40e+6, 60.
7.15e+6, 2.90e+6, 0.29, 1.40e+6, 1.40e+6, 1.40e+6, 70.
7.15e+6, 2.90e+6, 0.29, 1.40e+6, 1.40e+6, 1.40e+6, 80.
7.13e+6, 2.82e+6, 0.29, 1.34e+6, 1.34e+6, 1.34e+6, 100.
7.11e+6, 2.75e+6, 0.29, 1.29e+6, 1.29e+6, 1.29e+6, 120.
7.08e+6, 2.68e+6, 0.29, 1.24e+6, 1.24e+6, 1.24e+6, 140.
7.07e+6, 2.64e+6, 0.29, 1.22e+6, 1.22e+6, 1.22e+6, 150.
7.07e+6, 2.58e+6, 0.29, 1.20e+6, 1.20e+6, 1.20e+6, 160.
7.06e+6, 2.47e+6, 0.29, 1.15e+6, 1.15e+6, 1.15e+6, 180.
7.05e+6, 2.35e+6, 0.29, 1.10e+6, 1.10e+6, 1.10e+6, 200.
7.05e+6, 2.22e+6, 0.29, 0.98e+6, 0.98e+6, 0.98e+6, 220.
7.04e+6, 2.09e+6, 0.29, 0.87e+6, 0.87e+6, 0.87e+6, 240.
7.04e+6, 2.03e+6, 0.29, 0.81e+6, 0.81e+6, 0.81e+6, 250.
7.05e+6, 1.95e+6, 0.29, 0.75e+6, 0.75e+6, 0.75e+6, 260.
7.06e+6, 1.80e+6, 0.29, 0.62e+6, 0.62e+6, 0.62e+6, 280.
7.08e+6, 1.65e+6, 0.29, 0.50e+6, 0.50e+6, 0.50e+6, 300.
*DENSITY
0.00019,

```

```

*EXPANSION, TYPE=ORTHO, ZERO=71.
**  a1,      a2,      a3,  T
  0.2919E-05,  0.6095E-05,  ,  60.
  0.2968E-05,  0.6334E-05,  ,  70.
  0.3138E-05,  0.7169E-05,  ,  80.
  0.3455E-05,  0.9097E-05,  , 100.
  0.3664E-05,  0.1060E-04,  , 120.
  0.3750E-05,  0.1149E-04,  , 140.
  0.3762E-05,  0.1177E-04,  , 150.
  0.3758E-05,  0.1196E-04,  , 160.
  0.3728E-05,  0.1215E-04,  , 180.
  0.3691E-05,  0.1219E-04,  , 200.
  0.3666E-05,  0.1220E-04,  , 220.
  0.3665E-05,  0.1222E-04,  , 240.
  0.3673E-05,  0.1225E-04,  , 250.
  0.3687E-05,  0.1230E-04,  , 260.
  0.3723E-05,  0.1244E-04,  , 280.
  0.3763E-05,  0.1261E-04,  , 300.
**
** NITI
** Date: 13-Nov-03           Time: 16:50:42
**
*MATERIAL, NAME=NITI
*ELASTIC, TYPE=LAMINA
**  E1,      E2,      nu12,      G12,      G13,      G23,      T
  3.94000e+6,  3.94000e+6,  0.3,  1.51535e+6,  1.51535e+6,  1.51535e+6,  60.
  3.94000e+6,  3.94000e+6,  0.3,  1.51535e+6,  1.51535e+6,  1.51535e+6,  70.
  3.59667e+6,  3.59667e+6,  0.3,  1.38334e+6,  1.38334e+6,  1.38334e+6,  80.
  3.25333e+6,  3.25333e+6,  0.3,  1.25128e+6,  1.25128e+6,  1.25128e+6,  90.
  2.91000e+6,  2.91000e+6,  0.3,  1.11923e+6,  1.11923e+6,  1.11923e+6, 100.
  3.72800e+6,  3.72800e+6,  0.3,  1.43385e+6,  1.43385e+6,  1.43385e+6, 110.
  4.54600e+6,  4.54600e+6,  0.3,  1.74846e+6,  1.74846e+6,  1.74846e+6, 120.
  5.36400e+6,  5.36400e+6,  0.3,  2.06308e+6,  2.06308e+6,  2.06308e+6, 130.
  6.18200e+6,  6.18200e+6,  0.3,  2.37769e+6,  2.37769e+6,  2.37769e+6, 140.
  7.00000e+6,  7.00000e+6,  0.3,  2.69231e+6,  2.69231e+6,  2.69231e+6, 150.
  7.95600e+6,  7.95600e+6,  0.3,  3.06000e+6,  3.06000e+6,  3.06000e+6, 160.
  8.91200e+6,  8.91200e+6,  0.3,  3.42769e+6,  3.42769e+6,  3.42769e+6, 170.
  9.31200e+6,  9.31200e+6,  0.3,  3.58154e+6,  3.58154e+6,  3.58154e+6, 180.
  9.15600e+6,  9.15600e+6,  0.3,  3.52154e+6,  3.52154e+6,  3.52154e+6, 190.
  9.00000e+6,  9.00000e+6,  0.3,  3.46154e+6,  3.46154e+6,  3.46154e+6, 200.
  9.27000e+6,  9.27000e+6,  0.3,  3.56538e+6,  3.56538e+6,  3.56538e+6, 210.
  9.54000e+6,  9.54000e+6,  0.3,  3.66923e+6,  3.66923e+6,  3.66923e+6, 220.
  9.81000e+6,  9.81000e+6,  0.3,  3.77308e+6,  3.77308e+6,  3.77308e+6, 230.
  10.0800e+6,  10.0800e+6,  0.3,  3.87692e+6,  3.87692e+6,  3.87692e+6, 240.
  10.3500e+6,  10.3500e+6,  0.3,  3.98077e+6,  3.98077e+6,  3.98077e+6, 250.
  10.2740e+6,  10.2740e+6,  0.3,  3.95154e+6,  3.95154e+6,  3.95154e+6, 260.
  10.1980e+6,  10.1980e+6,  0.3,  3.92231e+6,  3.92231e+6,  3.92231e+6, 270.
  10.1220e+6,  10.1220e+6,  0.3,  3.89308e+6,  3.89308e+6,  3.89308e+6, 280.
  10.0460e+6,  10.0460e+6,  0.3,  3.86385e+6,  3.86385e+6,  3.86385e+6, 290.
  9.97000e+6,  9.97000e+6,  0.3,  3.83462e+6,  3.83462e+6,  3.83462e+6, 300.
  9.97000e+6,  9.97000e+6,  0.3,  3.83462e+6,  3.83462e+6,  3.83462e+6, 320.
*DENSITY
0.0005349,
*EXPANSION, TYPE=ORTHO, ZERO=71.
**  a1      a2      a3  T
  0.3670E-05,  0.3670E-05,  ,  60.
  0.3670E-05,  0.3670E-05,  ,  70.

```

```

-0.1430E-04, 0.3670E-05, , 80.
-0.2016E-04, 0.3670E-05, , 90.
-0.2692E-04, 0.3670E-05, , 100.
-0.3082E-04, 0.3670E-05, , 110.
-0.5461E-04, 0.3708E-05, , 120.
-0.7336E-04, 0.3794E-05, , 130.
-0.7746E-04, 0.3908E-05, , 140.
-0.7345E-04, 0.4037E-05, , 150.
-0.6568E-04, 0.4177E-05, , 160.
-0.5786E-04, 0.4324E-05, , 170.
-0.5466E-04, 0.4476E-05, , 180.
-0.5452E-04, 0.4617E-05, , 190.
-0.5356E-04, 0.4735E-05, , 200.
-0.5033E-04, 0.4836E-05, , 210.
-0.4667E-04, 0.4923E-05, , 220.
-0.4348E-04, 0.4999E-05, , 230.
-0.4051E-04, 0.5066E-05, , 240.
-0.3765E-04, 0.5126E-05, , 250.
-0.3634E-04, 0.5179E-05, , 260.
-0.3496E-04, 0.5226E-05, , 270.
-0.3375E-04, 0.5269E-05, , 280.
-0.3257E-04, 0.5308E-05, , 290.
-0.3159E-04, 0.5343E-05, , 300.
-0.3159E-04, 0.5343E-05, , 320.
**
** -----
** --- SHELL elements (with directional properties) ---
** -----
**
*SHELL SECTION, COMPOSITE, ELSET=SMACHELEM
** total thickness = 0.0825
0.004875, 3, GLEP, 45.
0.006, 3, NITI, 0.
0.004875, 3, GLEP, -45.
0.004875, 3, GLEP, 90.
0.004875, 3, GLEP, 45.
0.006, 3, NITI, 0.
0.004875, 3, GLEP, -45.
0.004875, 3, GLEP, 90.
0.004875, 3, GLEP, 90.
0.004875, 3, GLEP, -45.
0.006, 3, NITI, 0.
0.004875, 3, GLEP, 45.
0.004875, 3, GLEP, 90.
0.004875, 3, GLEP, -45.
0.006, 3, NITI, 0.
0.004875, 3, GLEP, 45.
**
*ELEMENT, TYPE=S4, ELSET=SMACHELEM
**
37, 38, 39, 76, 75
38, 39, 40, 77, 76
39, 40, 41, 78, 77
40, 41, 42, 79, 78
41, 42, 43, 80, 79
42, 43, 44, 81, 80
43, 44, 45, 82, 81

```

44, 45, 46, 83, 82
45, 46, 47, 84, 83
46, 47, 48, 85, 84
47, 48, 49, 86, 85
48, 49, 50, 87, 86
49, 50, 51, 88, 87
50, 51, 52, 89, 88
51, 52, 53, 90, 89
52, 53, 54, 91, 90
53, 54, 55, 92, 91
54, 55, 56, 93, 92
55, 56, 57, 94, 93
56, 57, 58, 95, 94
57, 58, 59, 96, 95
58, 59, 60, 97, 96
59, 60, 61, 98, 97
60, 61, 62, 99, 98
61, 62, 63, 100, 99
62, 63, 64, 101, 100
63, 64, 65, 102, 101
64, 65, 66, 103, 102
65, 66, 67, 104, 103
66, 67, 68, 105, 104
67, 68, 69, 106, 105
68, 69, 70, 107, 106
69, 70, 71, 108, 107
70, 71, 72, 109, 108
71, 72, 73, 110, 109
72, 73, 74, 111, 110
73, 75, 76, 113, 112
74, 76, 77, 114, 113
75, 77, 78, 115, 114
76, 78, 79, 116, 115
77, 79, 80, 117, 116
78, 80, 81, 118, 117
79, 81, 82, 119, 118
80, 82, 83, 120, 119
81, 83, 84, 121, 120
82, 84, 85, 122, 121
83, 85, 86, 123, 122
84, 86, 87, 124, 123
85, 87, 88, 125, 124
86, 88, 89, 126, 125
87, 89, 90, 127, 126
88, 90, 91, 128, 127
89, 91, 92, 129, 128
90, 92, 93, 130, 129
91, 93, 94, 131, 130
92, 94, 95, 132, 131
93, 95, 96, 133, 132
94, 96, 97, 134, 133
95, 97, 98, 135, 134
96, 98, 99, 136, 135
97, 99, 100, 137, 136
98, 100, 101, 138, 137
99, 101, 102, 139, 138
100, 102, 103, 140, 139

```

101, 103, 104, 141, 140
102, 104, 105, 142, 141
103, 105, 106, 143, 142
104, 106, 107, 144, 143
105, 107, 108, 145, 144
106, 108, 109, 146, 145
107, 109, 110, 147, 146
108, 110, 111, 148, 147
**
*SHELL SECTION, COMPOSITE, ELSET=GLEPELEM
** total thickness = 0.078
0.004875, 3, GLEP, 45.
0.004875, 3, GLEP, 0.
0.004875, 3, GLEP, -45.
0.004875, 3, GLEP, 90.
0.004875, 3, GLEP, 45.
0.004875, 3, GLEP, 0.
0.004875, 3, GLEP, -45.
0.004875, 3, GLEP, 90.
0.004875, 3, GLEP, 90.
0.004875, 3, GLEP, -45.
0.004875, 3, GLEP, 0.
0.004875, 3, GLEP, 45.
0.004875, 3, GLEP, 90.
0.004875, 3, GLEP, -45.
0.004875, 3, GLEP, 0.
0.004875, 3, GLEP, 45.
**
*ELEMENT, TYPE=S4, ELSET=GLEPELEM
**
1, 1, 2, 39, 38
2, 2, 3, 40, 39
3, 3, 4, 41, 40
4, 4, 5, 42, 41
5, 5, 6, 43, 42
6, 6, 7, 44, 43
7, 7, 8, 45, 44
8, 8, 9, 46, 45
9, 9, 10, 47, 46
10, 10, 11, 48, 47
11, 11, 12, 49, 48
12, 12, 13, 50, 49
13, 13, 14, 51, 50
14, 14, 15, 52, 51
15, 15, 16, 53, 52
16, 16, 17, 54, 53
17, 17, 18, 55, 54
18, 18, 19, 56, 55
19, 19, 20, 57, 56
20, 20, 21, 58, 57
21, 21, 22, 59, 58
22, 22, 23, 60, 59
23, 23, 24, 61, 60
24, 24, 25, 62, 61
25, 25, 26, 63, 62
26, 26, 27, 64, 63
27, 27, 28, 65, 64

```

```

28, 28, 29, 66, 65
29, 29, 30, 67, 66
30, 30, 31, 68, 67
31, 31, 32, 69, 68
32, 32, 33, 70, 69
33, 33, 34, 71, 70
34, 34, 35, 72, 71
35, 35, 36, 73, 72
36, 36, 37, 74, 73
109, 112, 113, 150, 149
110, 113, 114, 151, 150
111, 114, 115, 152, 151
112, 115, 116, 153, 152
113, 116, 117, 154, 153
114, 117, 118, 155, 154
115, 118, 119, 156, 155
116, 119, 120, 157, 156
117, 120, 121, 158, 157
118, 121, 122, 159, 158
119, 122, 123, 160, 159
120, 123, 124, 161, 160
121, 124, 125, 162, 161
122, 125, 126, 163, 162
123, 126, 127, 164, 163
124, 127, 128, 165, 164
125, 128, 129, 166, 165
126, 129, 130, 167, 166
127, 130, 131, 168, 167
128, 131, 132, 169, 168
129, 132, 133, 170, 169
130, 133, 134, 171, 170
131, 134, 135, 172, 171
132, 135, 136, 173, 172
133, 136, 137, 174, 173
134, 137, 138, 175, 174
135, 138, 139, 176, 175
136, 139, 140, 177, 176
137, 140, 141, 178, 177
138, 141, 142, 179, 178
139, 142, 143, 180, 179
140, 143, 144, 181, 180
141, 144, 145, 182, 181
142, 145, 146, 183, 182
143, 146, 147, 184, 183
144, 147, 148, 185, 184
**
*ELSET, ELSET=ALL_ELEMENTS
SMAHCELEM,
GLEPELEM,
**
*INITIAL CONDITIONS, TYPE=TEMPERATURE,
INPUT=beam2_run7_thermal_t71_nodeset.dat
**
**
*BOUNDARY
CFCF, 1,6,          0.
**

```

```

**
*NSET, NSET=CFCF
    1,    37,    38,    74,    75,    111,    112,    148,
    149,    185
**
*PSD-DEFINITION, NAME=S10TO400, G=1.0, INPUT=input_accel_psd.abq,
TYPE=BASE
**
** -----
** ----- STEP data for Eigensolution at 71 F
** -----
*STEP, PERTURBATION
Eigensolution for SMAHC beam at 71 F
**
*FREQUENCY, EIGENSOLVER=LANCZOS, NORMALIZATION=MASS
10, , 1500.
**
** Eigensolution output
**
***OUTPUT, FIELD
***NODE OUTPUT
**U,
*END STEP
**
** -----
** ----- STEP data for Linear Random Response at 71 F
** -----
*STEP, PERTURBATION
Linear random response of SMAHC beam at 71 F
**
** 0-400 Hz with 400 points between eigenfrequencies, 1.0 bias and linear
frequency
**
*RANDOM RESPONSE
0., 400., 400, 1.0, 1
**
** This is only needed in the event that a subset of the modes
** from the *FREQUENCY card are used
**
*SELECT EIGENMODES, GENERATE
1, 10
**
*MODAL DAMPING, MODAL=DIRECT
1,2, .0081
3,10, .0068
**
*CORRELATION, PSD=S10TO400, COMPLEX=NO, TYPE=CORRELATED
2, 1.
**
*DLOAD
**
*BASE MOTION, DOF=3, LOAD CASE=2, TYPE=ACCELERATION
**
** Random response PSD at three accel nodes
**
*OUTPUT, FIELD
*NODE OUTPUT, NSET=ACCELS

```

```

U,
**
*END STEP
** -----
** ----- STEP data for post-buckling 70-80 F
** -----
*STEP, NLGEOM, INC=33.3333
Post-buckling solution 70-80 degrees F
**
*STATIC, DIRECT
0.03,1.0
**
** input thermal load
**
*TEMPERATURE, INPUT=beam2_run7_thermal_T80_nodeset.dat
**
** Load deflection data at center node (propagates to subsequent static
steps)
**
*OUTPUT, HISTORY
*NODE OUTPUT, NSET=CENTER
U3,
**
*END STEP
** -----
** ----- STEP data for post-buckling 80-90 F
** -----
*STEP, NLGEOM, INC=33.3333
Post-buckling solution 80-90 degrees F
**
*STATIC, DIRECT
0.03,1.0
**
** Uniform thermal load
**
*TEMPERATURE, INPUT=beam2_run7_thermal_T90_nodeset.dat
**
** Load deflection data at center node (propagates to subsequent static
steps)
**
*OUTPUT, HISTORY
*NODE OUTPUT, NSET=CENTER
U3,
**
*END STEP
** -----
** ----- STEP data for post-buckling 90-100 F
** -----
*STEP, NLGEOM, INC=33.3333
Post-buckling solution 90-100 degrees F
**
*STATIC, DIRECT
0.03,1.0
**
** Uniform thermal load
**
*TEMPERATURE, INPUT=beam2_run7_thermal_T100_nodeset.dat

```

```

**
** Load deflection data at center node (propagates to subsequent static
steps)
**
**
*OUTPUT, HISTORY
*NODE OUTPUT, NSET=CENTER
U3,
**
*END STEP
** -----
** ----- STEP data for post-buckling 100-110 F
** -----
*STEP, NLGEOM, INC=33.3333
Post-buckling solution 100-110 degrees F
**
*STATIC, DIRECT
0.03,1.0
**
** Uniform thermal load
**
*TEMPERATURE, INPUT=beam2_run7_thermal_T110_nodeset.dat
**
** Load deflection data at center node (propagates to subsequent static
steps)
**
*OUTPUT, HISTORY
*NODE OUTPUT, NSET=CENTER
U3,
**
*END STEP
** -----
** ----- STEP data for post-buckling 110-120 F
** -----
*STEP, NLGEOM, INC=33.3333
Post-buckling solution 110-120 degrees F
**
*STATIC, DIRECT
0.03,1.0
**
** Uniform thermal load
**
*TEMPERATURE, INPUT=beam2_run7_thermal_T120_nodeset.dat
**
** Load deflection data at center node (propagates to subsequent static
steps)
**
*OUTPUT, HISTORY
*NODE OUTPUT, NSET=CENTER
U3,
**
*END STEP
** -----
** ----- STEP data for post-buckling 120-130 F
** -----
*STEP, NLGEOM, INC=33.3333
Post-buckling solution 120-130 degrees F
**

```

```

*STATIC, DIRECT
0.03,1.0
**
** Uniform thermal load
**
*TEMPERATURE, INPUT=beam2_run7_thermal_T130_nodeset.dat
**
** Load deflection data at center node (propagates to subsequent static
steps)
**
*OUTPUT, HISTORY
*NODE OUTPUT, NSET=CENTER
U3,
**
*END STEP
** -----
** ----- STEP data for post-buckling 130-140 F
** -----
*STEP, NLGEOM, INC=33.3333
Post-buckling solution 130-140 degrees F
**
*STATIC, DIRECT
0.03,1.0
**
** Uniform thermal load
**
*TEMPERATURE, INPUT=beam2_run7_thermal_T140_nodeset.dat
**
** Load deflection data at center node (propagates to subsequent static
steps)
**
*OUTPUT, HISTORY
*NODE OUTPUT, NSET=CENTER
U3,
**
*END STEP
** -----
** ----- STEP data for post-buckling 140-150 F
** -----
*STEP, NLGEOM, INC=33.3333
Post-buckling solution 140-150 degrees F
**
*STATIC, DIRECT
0.03,1.0
**
** Uniform thermal load
**
*TEMPERATURE, INPUT=beam2_run7_thermal_T150_nodeset.dat
**
** Load deflection data at center node (propagates to subsequent static
steps)
**
*OUTPUT, HISTORY
*NODE OUTPUT, NSET=CENTER
U3,
**
*END STEP

```

```

** -----
** ----- STEP data for post-buckling 150-160 F
** -----
*STEP, NLGEOM, INC=33.3333
Post-buckling solution 150-160 degrees F
**
*STATIC, DIRECT
0.03,1.0
**
** Uniform thermal load
**
*TEMPERATURE, INPUT=beam2_run7_thermal_T160_nodeset.dat
**
** Load deflection data at center node (propagates to subsequent static
steps)
**
*OUTPUT, HISTORY
*NODE OUTPUT, NSET=CENTER
U3,
**
*END STEP
** -----
** ----- STEP data for Eigensolution at 160 F
** -----
*STEP, PERTURBATION
Eigensolution for SMAHC beam at 160 F
**
*FREQUENCY, EIGENSOLVER=LANCZOS, NORMALIZATION=MASS
10, , 1500.
**
** Eigensolution output
**
***OUTPUT, FIELD
***NODE OUTPUT
**U,
*END STEP
**
** -----
** ----- STEP data for Linear Random Response at 160 F
** -----
*STEP, PERTURBATION
Linear random response of SMAHC beam at 160 F
**
** 0-400 Hz with 400 points between eigenfrequencies, 1.0 bias and linear
frequency
**
*RANDOM RESPONSE
0., 400., 400, 1.0, 1
**
** This is only needed in the event that a subset of the modes
** from the *FREQUENCY card are used
**
*SELECT EIGENMODES, GENERATE
1, 10
**
*MODAL DAMPING, MODAL=DIRECT
1,2, .0017

```

```

3,10, .0025
**
**CORRELATION, PSD=S10TO400, COMPLEX=NO, TYPE=CORRELATED
2, 1.
**
**DLOAD
**
**BASE MOTION, DOF=3, LOAD CASE=2, TYPE=ACCELERATION
**
** Random response PSD at three accel nodes
**
**OUTPUT, FIELD
**NODE OUTPUT, NSET=ACCELS
U,
**
**END STEP
** -----
** ----- STEP data for post-buckling 160-180 F
** -----
**STEP, NLGEOM
Post-buckling solution 160-180 degrees F
**
**STATIC, DIRECT
0.5,1.0
**
** Uniform thermal load
**
**TEMPERATURE, INPUT=beam2_run7_thermal_T180_nodeset.dat
**
** Load deflection data at center node (carries forward from above)
**
**END STEP
** -----
** ----- STEP data for post-buckling 180-200 F
** -----
**STEP, NLGEOM
Post-buckling solution 180-200 degrees F
**
**STATIC, DIRECT
0.5,1.0
**
** Uniform thermal load
**
**TEMPERATURE, INPUT=beam2_run7_thermal_T200_nodeset.dat
**
** Load deflection data at center node (carries forward from above)
**
**END STEP
** -----
** ----- STEP data for Eigensolution at 200 F
** -----
**STEP, PERTURBATION
Eigensolution for SMAHC beam at 200 F
**
**FREQUENCY, EIGENSOLVER=LANCZOS, NORMALIZATION=MASS
10, , 1500.
**

```

```

** Eigensolution output
**
***OUTPUT, FIELD
***NODE OUTPUT
**U,
*END STEP
**
** -----
** ----- STEP data for Linear Random Response at 200 F
** -----
*STEP, PERTURBATION
Linear random response of SMAHC beam at 200 F
**
** 0-400 Hz with 400 points between eigenfrequencies, 1.0 bias and linear
frequency
**
*RANDOM RESPONSE
0., 400., 400, 1.0, 1
**
** This is only needed in the event that a subset of the modes
** from the *FREQUENCY card are used
**
*SELECT EIGENMODES, GENERATE
1, 10
**
*MODAL DAMPING, MODAL=DIRECT
1,2, .0016
3,10, .0016
**
*CORRELATION, PSD=S10TO400, COMPLEX=NO, TYPE=CORRELATED
2, 1.
**
*DLOAD
**
*BASE MOTION, DOF=3, LOAD CASE=2, TYPE=ACCELERATION
**
** Random response PSD at 3 accel nodes
**
*OUTPUT, FIELD
*NODE OUTPUT, NSET=ACCELS
U,
**
*END STEP
** -----
** ----- STEP data for post-buckling 200-220 F
** -----
*STEP, NLGEOM
Post-buckling solution 200-220 degrees F
**
*STATIC, DIRECT
0.5,1.0
**
** Uniform thermal load
**
*TEMPERATURE, INPUT=beam2_run7_thermal_T220_nodeset.dat
**
** Load deflection data at center node (carries forward from above)

```

```

**
*END STEP
** -----
** ----- STEP data for post-buckling 220-250 F
** -----
*STEP, NLGEOM
Post-buckling solution 220-250 degrees F
**
*STATIC, DIRECT
0.5,1.0
**
** Uniform thermal load
**
*TEMPERATURE, INPUT=beam2_run7_thermal_T250_nodeset.dat
**
** Load deflection data at center node (carries forward from above)
**
*END STEP
** -----
** ----- STEP data for Eigensolution at 250 F
** -----
*STEP, PERTURBATION
Eigensolution for SMAHC beam at 250 F
**
*FREQUENCY, EIGENSOLVER=LANCZOS, NORMALIZATION=MASS
10, , 1500.
**
** Eigensolution output
**
***OUTPUT, FIELD
***NODE OUTPUT
**U3,
*END STEP
**
** -----
** ----- STEP data for Linear Random Response at 250 F
** -----
*STEP, PERTURBATION
Linear random response of SMAHC beam at 250 F
**
** 0-400 Hz with 400 points between eigenfrequencies, 1.0 bias and linear
frequency
**
*RANDOM RESPONSE
0., 400., 400, 1.0, 1
**
** This is only needed in the event that a subset of the modes
** from the *FREQUENCY card are used
**
*SELECT EIGENMODES, GENERATE
1, 10
**
*MODAL DAMPING, MODAL=DIRECT
1,2,.0021
3,10, .0022
**
*CORRELATION, PSD=S10TO400, COMPLEX=NO, TYPE=CORRELATED

```

```
2, 1.  
**  
*DLOAD  
**  
*BASE MOTION, DOF=3, LOAD CASE=2, TYPE=ACCELERATION  
**  
** Random response PSD at 3 accel nodes  
**  
*OUTPUT, FIELD  
*NODE OUTPUT, NSET=ACCELS  
U,  
**  
*END STEP
```

REPORT DOCUMENTATION PAGE

*Form Approved
OMB No. 0704-0188*

The public reporting burden for this collection of information is estimated to average 1 hour per response, including the time for reviewing instructions, searching existing data sources, gathering and maintaining the data needed, and completing and reviewing the collection of information. Send comments regarding this burden estimate or any other aspect of this collection of information, including suggestions for reducing this burden, to Department of Defense, Washington Headquarters Services, Directorate for Information Operations and Reports (0704-0188), 1215 Jefferson Davis Highway, Suite 1204, Arlington, VA 22202-4302. Respondents should be aware that notwithstanding any other provision of law, no person shall be subject to any penalty for failing to comply with a collection of information if it does not display a currently valid OMB control number.
PLEASE DO NOT RETURN YOUR FORM TO THE ABOVE ADDRESS.

1. REPORT DATE (DD-MM-YYYY) 01- 10 - 2005		2. REPORT TYPE Contractor Report		3. DATES COVERED (From - To) Aug 2003-Aug 2004	
4. TITLE AND SUBTITLE Investigation of the Thermomechanical Response of Shape Memory Alloy Hybrid Composite Beams				5a. CONTRACT NUMBER	
				5b. GRANT NUMBER NCC-1-02043	
				5c. PROGRAM ELEMENT NUMBER	
6. AUTHOR(S) Brian A. Davis				5d. PROJECT NUMBER	
				5e. TASK NUMBER	
				5f. WORK UNIT NUMBER 23-781-10-13	
7. PERFORMING ORGANIZATION NAME(S) AND ADDRESS(ES) NASA Langley Research Center Hampton, VA 23681-2199			8. PERFORMING ORGANIZATION REPORT NUMBER North Carolina State University Raleigh, NC 27695		
9. SPONSORING/MONITORING AGENCY NAME(S) AND ADDRESS(ES) National Aeronautics and Space Administration Washington, DC 20546-0001				10. SPONSOR/MONITOR'S ACRONYM(S) NASA	
				11. SPONSOR/MONITOR'S REPORT NUMBER(S) NASA/CR-2005-213929	
12. DISTRIBUTION/AVAILABILITY STATEMENT Unclassified - Unlimited Subject Category 39 Availability: NASA CASI (301) 621-0390					
13. SUPPLEMENTARY NOTES NASA Langley Technical Monitor: Travis L. Turner An electronic version can be found at http://ntrs.nasa.gov					
14. ABSTRACT Previous work at NASA Langley Research Center (LaRC) involved fabrication and testing of composite beams with embedded, pre-strained shape memory alloy (SMA) ribbons. That study also provided comparison of experimental results with numerical predictions from a research code making use of a new thermoelastic model for shape memory alloy hybrid composite (SMAHC) structures. The previous work showed qualitative validation of the numerical model. However, deficiencies in the experimental-numerical correlation were noted and hypotheses for the discrepancies were given for further investigation. The goal of this work is to refine the experimental measurement and numerical modeling approaches in order to better understand the discrepancies, improve the correlation between prediction and measurement, and provide rigorous quantitative validation of the numerical model. Thermal buckling, post-buckling, and random responses to thermal and inertial (base acceleration) loads are studied. Excellent agreement is achieved between the predicted and measured results, thereby quantitatively validating the numerical tool.					
15. SUBJECT TERMS Shape memory alloys, Nitinol, embedded actuators, hybrid composites, adaptive stiffening, thermal post-buckling control, vibration control, ABAQUS, finite element analysis, infrared thermography, projection moire interferometry, geometric imperfections					
16. SECURITY CLASSIFICATION OF:			17. LIMITATION OF ABSTRACT	18. NUMBER OF PAGES	19a. NAME OF RESPONSIBLE PERSON
a. REPORT	b. ABSTRACT	c. THIS PAGE			STI Help Desk (email: help@sti.nasa.gov)
U	U	U	UU	135	19b. TELEPHONE NUMBER (Include area code) (301) 621-0390